

# Modeling of magnetized expanding plasmas

***Citation for published version (APA):***

Peerenboom, K. S. C. (2012). *Modeling of magnetized expanding plasmas*. [Phd Thesis 1 (Research TU/e / Graduation TU/e), Applied Physics and Science Education]. Technische Universiteit Eindhoven.  
<https://doi.org/10.6100/IR733452>

***DOI:***

[10.6100/IR733452](https://doi.org/10.6100/IR733452)

***Document status and date:***

Published: 01/01/2012

***Document Version:***

Publisher's PDF, also known as Version of Record (includes final page, issue and volume numbers)

***Please check the document version of this publication:***

- A submitted manuscript is the version of the article upon submission and before peer-review. There can be important differences between the submitted version and the official published version of record. People interested in the research are advised to contact the author for the final version of the publication, or visit the DOI to the publisher's website.
- The final author version and the galley proof are versions of the publication after peer review.
- The final published version features the final layout of the paper including the volume, issue and page numbers.

[Link to publication](#)

***General rights***

Copyright and moral rights for the publications made accessible in the public portal are retained by the authors and/or other copyright owners and it is a condition of accessing publications that users recognise and abide by the legal requirements associated with these rights.

- Users may download and print one copy of any publication from the public portal for the purpose of private study or research.
- You may not further distribute the material or use it for any profit-making activity or commercial gain
- You may freely distribute the URL identifying the publication in the public portal.

If the publication is distributed under the terms of Article 25fa of the Dutch Copyright Act, indicated by the "Taverne" license above, please follow below link for the End User Agreement:

[www.tue.nl/taverne](http://www.tue.nl/taverne)

***Take down policy***

If you believe that this document breaches copyright please contact us at:

[openaccess@tue.nl](mailto:openaccess@tue.nl)

providing details and we will investigate your claim.

# Modeling of Magnetized Expanding Plasmas

PROEFSCHRIFT

ter verkrijging van de graad van doctor  
aan de Technische Universiteit Eindhoven,  
op gezag van de rector magnificus, prof.dr.ir. C.J. van Duijn,  
voor een commissie aangewezen door het College voor Promoties  
in het openbaar te verdedigen  
op donderdag 5 juli 2012 om 16.00 uur

door

Kim Stephanie Cathelijne Beks-Peerenboom

geboren te Eindhoven

Dit proefschrift is goedgekeurd door de promotoren:

prof.dr.ir. G.M.W. Kroesen  
en  
prof.dr. W.J. Goedheer

Copromotor:  
dr.ir. J. van Dijk

CIP-DATA TECHNISCHE UNIVERSITEIT EINDHOVEN

Beks-Peerenboom, Kim Stephanie Cathelijn

Modeling of Magnetized Expanding Plasmas / by Kim Beks-Peerenboom. -  
Eindhoven : Technische Universiteit Eindhoven, 2012. - Proefschrift.

A catalogue record is available from the Eindhoven University of  
Technology Library.

ISBN: 978-90-386-3177-6

NUR 928

Subject headings: plasma physics / plasma modeling / computational fluid  
dynamics / Stefan-Maxwell equations / fusion

Copyright © 2012 Kim Beks-Peerenboom

All rights reserved. No part of this book may be reproduced, stored in  
a database or retrieval system, or published, in any form or in any way,  
electronically, mechanically, by print, photo-print, microfilm or any  
other means without prior written permission of the author.

Printed by Ipskamp Drukkers B.V.

# Contents

<b>1</b>	<b>Introduction</b>	<b>1</b>
1.1	Fusion energy . . . . .	1
1.2	Modeling of Magnum-PSI . . . . .	2
1.3	Outline . . . . .	3
<b>2</b>	<b>Magneto-hydrodynamic equations</b>	<b>5</b>
2.1	Conservation equations . . . . .	5
2.1.1	Mass and charge conservation . . . . .	6
2.1.2	Momentum conservation . . . . .	7
2.1.3	Energy conservation . . . . .	8
2.2	Transport fluxes . . . . .	9
2.2.1	The isotropic case . . . . .	10
2.2.2	The anisotropic case . . . . .	11
2.3	Final form . . . . .	12
<b>3</b>	<b>Numerical strategies</b>	<b>13</b>
3.1	Numerical modeling . . . . .	13
3.2	Finite volume discretization . . . . .	13
3.2.1	Scalar convection-diffusion equations . . . . .	15
3.2.2	Systems of convection-diffusion equations . . . . .	18
3.3	Source term linearization . . . . .	21
3.3.1	The source dominated limit . . . . .	22
3.3.2	Linearization of the chemical sources . . . . .	23
3.3.3	Linearization of the energy sources . . . . .	25
3.4	Iteration and underrelaxation . . . . .	26
3.5	Matrix conditioning and solving . . . . .	27
3.6	Concluding remarks . . . . .	28
<b>4</b>	<b>Multicomponent diffusion in neutral mixtures</b>	<b>29</b>
4.1	Introduction . . . . .	30
4.2	Governing equations . . . . .	31
4.2.1	Continuity equations and constraints . . . . .	31
4.2.2	Stefan-Maxwell equations . . . . .	32

4.3	The flux diffusion matrix . . . . .	34
4.3.1	Calculation of $\tilde{\mathbf{M}}$ . . . . .	35
4.3.2	Calculation of $\tilde{\mathbf{D}}$ . . . . .	36
4.3.3	Calculation of $\mathbf{R}$ . . . . .	38
4.4	Analytical examples . . . . .	38
4.5	Discrete mass conservation . . . . .	40
4.6	Test case: Mixing of $\text{H}_2\text{O}$ , $\text{H}_2$ and $\text{N}_2$ . . . . .	42
4.7	Discussion . . . . .	43
<b>5</b>	<b>Ambipolar diffusion</b> . . . . .	<b>47</b>
5.1	Introduction . . . . .	47
5.2	Constraints and singularities . . . . .	47
5.3	The ambipolar diffusion matrix . . . . .	49
5.4	Analytical examples . . . . .	50
5.5	Regularization . . . . .	52
5.6	Discrete mass and charge conservation . . . . .	53
5.7	Test case: drift in a $\text{H}$ , $\text{H}^+$ , electron mixture . . . . .	55
5.8	Discussion . . . . .	56
<b>6</b>	<b>Diffusion in magnetized plasmas</b> . . . . .	<b>57</b>
6.1	Stefan-Maxwell equations in a magnetic field . . . . .	58
6.1.1	Along, across and around the field lines . . . . .	58
6.1.2	The quasi-neutrality constraint . . . . .	61
6.2	Analytical example . . . . .	62
<b>7</b>	<b>Supersonic expansion of argon in Magnum-PSI</b> . . . . .	<b>65</b>
7.1	Introduction . . . . .	66
7.2	Underexpanded jet . . . . .	67
7.3	The SIMPLE algorithm . . . . .	69
7.3.1	Incompressible flows . . . . .	69
7.3.2	Compressible flows . . . . .	73
7.4	Numerical model of the source and the expansion . . . . .	74
7.5	Numerical results . . . . .	76
7.5.1	The free expansion . . . . .	76
7.5.2	Shock position . . . . .	76
7.5.3	Influence of nozzle geometry . . . . .	79
7.6	Conclusions . . . . .	80
<b>8</b>	<b>Effects of magnetization on the expanding argon jet</b> . . . . .	<b>83</b>
8.1	Introduction . . . . .	83
8.2	Numerical model for the magnetized expansion . . . . .	83
8.2.1	Anisotropic transport coefficients . . . . .	84
8.2.2	Flow field . . . . .	84
8.2.3	Electromagnetic field . . . . .	85

8.3	Results . . . . .	87
8.3.1	Flow field . . . . .	87
8.3.2	Potential distribution . . . . .	89
8.3.3	Source output . . . . .	89
8.4	Conclusions . . . . .	92
<b>9</b>	<b>The expanding hydrogen plasma - comparison with experiments</b>	<b>93</b>
9.1	Introduction . . . . .	93
9.2	Setup and operating conditions . . . . .	94
9.3	Composition . . . . .	95
9.4	Results . . . . .	97
9.4.1	Comparison to pressure measurements . . . . .	97
9.4.2	Comparison to I-V measurements . . . . .	97
9.4.3	Comparison to Thomson measurements . . . . .	99
9.5	Conclusions . . . . .	100
<b>10</b>	<b>General conclusions</b>	<b>103</b>
<b>A</b>	<b>Linear algebra overview</b>	<b>105</b>
A.1	The generalized inverse . . . . .	105
A.2	Oblique projectors . . . . .	106
	<b>List of symbols</b>	<b>109</b>
	<b>Bibliography</b>	<b>III</b>
	<b>Abstract</b>	<b>II7</b>
	<b>Dankwoord</b>	<b>II9</b>
	<b>Curriculum Vitae</b>	<b>121</b>



## Chapter 1

# Introduction

### 1.1 Fusion energy

Climate change, shortage of fossil fuels and geopolitical considerations pose the need for alternative energy sources. Nuclear fusion energy could possibly provide this alternative for fossil fuels. One of the methods to generate fusion is based on the magnetic confinement of the fusion plasma. This method underlies the ITER [1] project, which aims to demonstrate the feasibility of fusion power. However, for fusion power to become a success, many difficulties still have to be overcome. One of the issues is the Plasma Surface Interaction (PSI) in the exhaust, the divertor, of the fusion reactor. A photograph of a divertor can be seen in Figure 1.1.

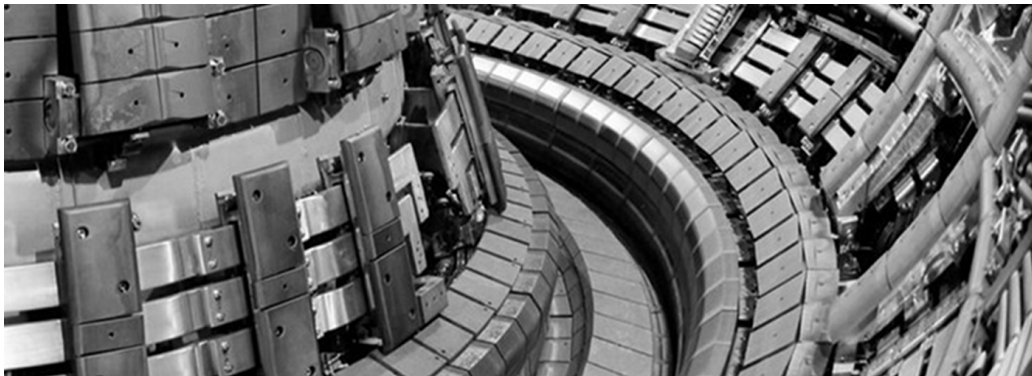


**Figure 1.1:** Divertor plates in the bottom of JET, currently the largest device producing fusion relevant plasmas. Photograph from EFDA (European Fusion Development Agreement).

The task of the divertor is to remove helium, the end product of the fusion reaction, and other impurities from the fusion plasma, since they cool down the plasma and dilute the deuterium-tritium fuel mixture. To this end, the magnetic field is configured to have closed field lines within the so-called ‘separatrix’ and open field lines outside the separatrix, see Figure 1.2. The plasma in the center of the reactor is thus confined, while the edge of the plasma is in contact with the divertor plates.



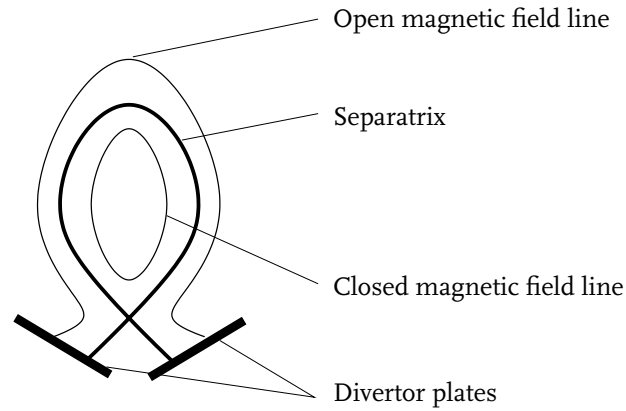


**Figure 1.2:** Separatrix. The magnetic field lines are closed within the separatrix and open outside the separatrix.

In the divertor, the wall of the fusion reactor is exposed to very high flux densities ( $10^{24}$  ions  $\text{m}^{-2}\text{s}^{-1}$ ) and energy fluxes ( $10 \text{ MW/m}^2$ ), despite the relatively low temperature ( $<10 \text{ eV}$ ) [2]. Due to the high heat flux, problems as melting and evaporation can occur. The particle fluxes can cause chemical and physical erosion and retention of fusion fuels by implantation or redeposition of eroded materials. These issues may limit the operational lifetime of the fusion reactor and can reduce fusion performance, since the eroded materials cool down the fusion plasma.

## 1.2 Modeling of Magnum-PSI

To obtain insight in the chemical and physical processes in the divertor, the linear plasma experiment Magnum-PSI (Magnetized Plasma Generator and Numerical Modeling for Plasma Surface Interaction studies) has been built at the FOM Institute for Plasma Physics in Rijnhuizen. In Figure 1.3, a side view of the Magnum-PSI experiment can be seen. The plasma in Magnum-PSI is created by a cascaded arc [3, 4] plasma source. After the source the plasma enters a vacuum chamber which is surrounded by a superconducting (3 Tesla) magnet to confine the plasma beam. In the target analysis chamber materials exposed to the plasma beam can be analyzed.

There have been a number of simulations with different codes on different aspects of Magnum-PSI. Simulations of the expansion into the source chamber have, for example, been carried out with gas dynamics and MagnetoHydroDynamic (MHD) approaches [5]. The interaction of the plasma with the target is modeled with Molecular Dynamics (MD) [6, 7, 8]. The plasma in the heating chamber and around the target have been modeled with the B2-EIRENE and B2.5-EUNOMIA codes [9, 10]. These codes use a fluid dynamic approach for the charged particles and a Monte Carlo solver for the neutrals. They can give a detailed description of the plasma in front of the target, but are less suited for simulation of the plasma source and expansion of the plasma into the source chamber.

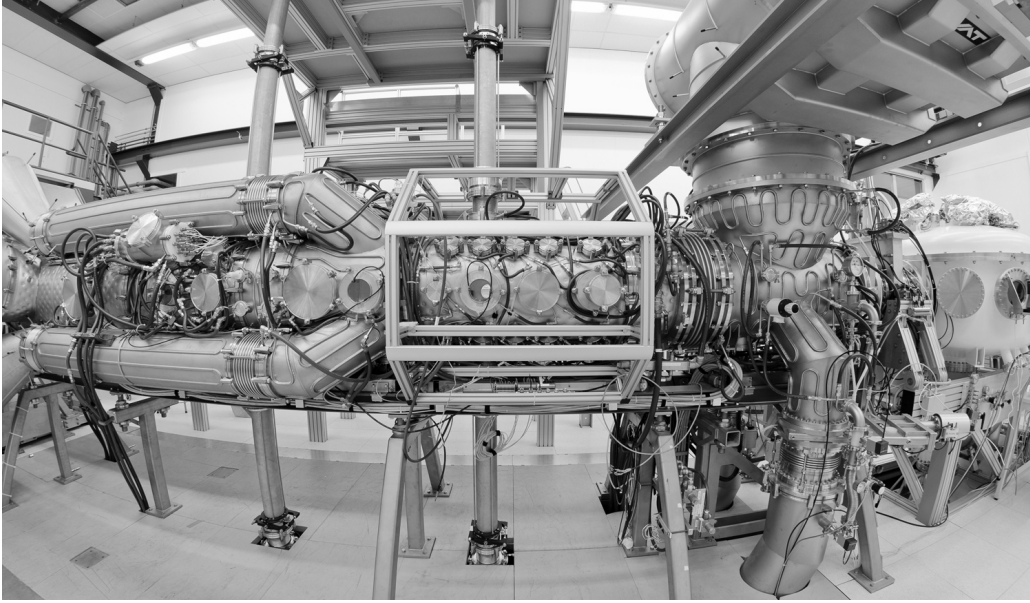


**Figure 1.3:** The Magnum-PSI experiment. The total length of the setup is about 15 meter. At the left the plasma is created by a cascaded arc. The magnet was not yet installed when this picture was made.

### 1.3 Outline

The focus of this thesis is the development of a numerical model for studying the plasma creation in the source and the consecutive magnetized expansion in Magnum-PSI. The numerical model is constructed using the modeling platform Plasimo [11]. In Chapter 2, the fluid equations describing the plasma are derived. The numerical strategies for solving these equations are introduced in Chapter 3. Special attention is paid to the system of continuity equations for the species in the plasma. To deal with the coupling between the species, a new finite volume discretization method is introduced to discretize this system of coupled continuity equations. Additionally, source term linearization of strong chemical sources, necessary for plasma near chemical equilibrium, is discussed.

To describe the behavior of the different species in the whole range of conditions in the magnetized expanding plasma – from gas to fully ionized, from non-magnetized to strongly magnetized – a multicomponent diffusion description is needed. Multi-component diffusion is discussed in Chapters 4, 5 and 6. We start by first considering a mixture with only neutral species in Chapter 4. For numerical stability, the mass constraint is not explicitly applied. Instead, all species mass fractions are treated as independent unknowns and the mass constraint is a result of the continuity equations, the boundary conditions, the diffusion algorithm and the new discretization scheme from Chapter 3. With this method, the mass constraint can be satisfied exactly, although it is not explicitly applied.

In Chapter 5, this method is extended to ambipolar plasmas with charged species. In addition to the mass constraint, there is now also a charge constraint. Furthermore, the diffusion algorithm is coupled to the electromagnetic calculation in case of ambipolar plasmas. Since mass and charge conservation constraints are not applied a priori, utmost care has to be taken in this coupling to obtain a consistent set of equations.

In magnetized plasmas, discussed in Chapter 6, multicomponent diffusion becomes even more involved since the flow directions across and around the magnetic field lines are coupled by the Lorentz force. Coupling is taken into account by using complex arithmetic in the diffusion algorithm.

With the numerical model, a number of case studies are carried out. Chapter 7 presents a study of an unmagnetized argon arc to validate the flow calculation. Additionally, the effect of the nozzle geometry on the plasma beam is studied. In Chapter 8 the argon model is extended with a magnetic field. The effect of this magnetic field on the flow pattern and plasma production is investigated. Chapter 9 presents a model of the expanding hydrogen plasma in a magnetic field. The results of this model are compared to experiments on Pilot-PSI, the forerunner of Magnum-PSI. Finally, the conclusions are summarized in Chapter 10.

## Chapter 2

# Magneto-hydrodynamic equations

The description of the magnetized plasma in this thesis is based on the multi-fluid approach. The conservation equations in this multi-fluid approach are derived from the Boltzmann transport equation which gives the density distribution of particles in phase space. By taking successive moments of the Boltzmann transport equation, conservation equations for mass, charge, momentum and energy are obtained.

The species distribution function  $f_i(\vec{r}, \vec{w}, t)$  is defined such that the number of particles of species type  $i$  within a volume element  $d\vec{r}$  around  $\vec{r}$  and within a velocity space element  $d\vec{w}$  around  $\vec{w}$  at time  $t$  is given by  $f_i(\vec{r}, \vec{w}, t)d\vec{r}d\vec{w}$ . The evolution of the distribution function in time can be described by the Boltzmann transport equation [12, 13]:

$$\frac{\partial f_i}{\partial t} + \vec{w} \cdot \nabla_{\vec{r}} f_i + \frac{\vec{F}_i}{m_i} \cdot \nabla_{\vec{w}} f_i = \left( \frac{\partial f_i}{\partial t} \right)_c, \quad (2.1)$$

where the first term on the left hand side represents the temporal evolution, the second term the change because of spatial gradients and the third term describes the change in the distribution function due to forces  $\vec{F}_i$  acting on the species of mass  $m_i$ . The gradient operator in position space is denoted by  $\nabla_{\vec{r}}$ , whereas  $\nabla_{\vec{w}}$  gives the gradient operator in velocity space. The right hand side gives the source term for the distribution function due to elastic and inelastic processes like excitation and de-excitation.

### 2.1 Conservation equations

We consider a multicomponent medium composed of different species  $i$  with number densities  $n_i$ , masses  $m_i$  and velocities  $\vec{u}_i$ . The species' mass densities are denoted as  $\rho_i = n_i m_i$ . The total mass density of the plasma is then defined by:

$$\rho = \sum_i \rho_i, \quad (2.2)$$

and the species mass fractions by:

$$y_i = \frac{\rho_i}{\rho}. \quad (2.3)$$

By their definition, the species mass fractions should obey the following *mass constraint*:

$$\sum_i y_i = 1. \quad (2.4)$$

The mass averaged velocity field  $\vec{v}$  is defined as:

$$\vec{v} = \sum_i y_i \vec{u}_i. \quad (2.5)$$

The diffusion velocity  $\vec{v}_i$  of species  $i$  is defined as the species velocity relative to the mass averaged velocity field, i.e.,

$$\vec{v}_i = \vec{u}_i - \vec{v}. \quad (2.6)$$

From the definition of the mass averaged velocity field it follows that

$$\sum_i y_i \vec{v}_i = \sum_i y_i \vec{u}_i - \sum_i y_i \vec{v} = \vec{0}. \quad (2.7)$$

We will refer to this constraint on the diffusion velocities as the *mass flux constraint*.

### 2.1.1 Mass and charge conservation

Mass conservation on the species level can be described by the species continuity equations. The species continuity equations are obtained by multiplication of (2.1) with  $m_i$  and integration over velocity space:

$$\frac{\partial \rho y_i}{\partial t} + \nabla \cdot (\rho y_i \vec{v}) + \nabla \cdot (\rho y_i \vec{v}_i) = m_i \omega_i, \quad (2.8)$$

where  $\omega_i$  is the density production rate of species  $i$  due to volume production processes. Summation of equation (2.8) over all species gives the global mass balance of the plasma:

$$\frac{\partial \rho}{\partial t} + \nabla \cdot (\rho \vec{v}) = 0, \quad (2.9)$$

where the right hand side is zero since no net mass is created in chemical reactions. Likewise, the global charge balance can be obtained by multiplication of (2.8) by  $q_i/m_i$  and summation over all species:

$$\frac{\partial \rho \sigma^c}{\partial t} + \nabla \cdot \vec{j} = 0, \quad (2.10)$$

with  $\sigma^c = \sum_i q_i y_i / m_i$  and  $\vec{j} = \sum_i n_i q_i \vec{u}_i$  the current density. Again, the right hand side is zero since no net charge is created in chemical reactions. It can be seen that charge density can only build up when the current is not divergence free. This charge density leads to an electric field, which can be calculated from Poisson's equation:

$$\nabla^2 \phi = -\rho \sigma^c / \epsilon, \quad (2.11)$$

with  $\phi$  the electrostatic potential and  $\epsilon$  the permittivity. The typical length scale over which charge separation is present is called the Debye length  $\lambda_D$  [14, chapter 3, section 2]. In plasmas where  $\lambda_D$  is small, resolving the charge density  $\sigma^c$  is not very efficient, since it requires excessively fine meshes. In these plasmas, it is more appropriate to consider the electric field in the limit of vanishing Debye length. In the limit of vanishing Debye length, the plasma becomes quasi-neutral:  $\sigma^c = 0$ . The electric field necessary to maintain this situation is called the ambipolar field  $\vec{E}_{\text{amb}}$ . The assumption of an ambipolar plasma puts extra constraints on the mass fractions and the diffusion velocities. Ambipolar diffusion will be the topic of Chapter 5.

### 2.1.2 Momentum conservation

The first moment of the Boltzmann Transport equation, the momentum balance, is obtained by multiplying (2.1) by  $m_i \vec{w}$  and integrating over velocity space:

$$\frac{\partial \rho_i \vec{u}_i}{\partial t} + \nabla \cdot (\rho_i \vec{u}_i \vec{u}_i) = -\nabla p_i^* - \nabla \cdot \bar{\bar{\pi}}_i^* + \vec{R}_i^F + \vec{F}_i, \quad (2.12)$$

where the term  $\vec{R}_i^F$  is the friction force which gives the momentum exchange between species  $i$  and all the other species due to collisions. The term  $\vec{F}_i$  represents the volume forces, for example, the electric field, magnetic field or gravitational field. The pressure and viscous stress tensor are given by  $p_i^*$  and  $\bar{\bar{\pi}}_i^*$ , respectively. The  $*$  means that the pressure and viscous stress tensor are defined in the system of species  $i$  and give the rate at which momentum is transferred across a surface moving with the mean velocity  $\vec{u}_i$  of the species. In contrast, the quantities  $p_i$  and  $\bar{\bar{\pi}}_i$  give the rate at which momentum is transferred across a surface moving with the mass averaged velocity  $\vec{v}$ . As a consequence, summation of  $p_i^*$  and  $\bar{\bar{\pi}}_i^*$  over all species  $i$  does, in general, not give the total pressure  $p$  and viscous stress tensor  $\bar{\bar{\pi}}$ . The pressure and viscous stress tensor can be transformed to the bulk system via [12, 13]:

$$(\bar{\bar{\pi}}_i)_{kl} - (\bar{\bar{\pi}}_i^*)_{kl} = n_i m_i \left( \langle (\vec{c}_i)_k \rangle \langle (\vec{c}_i)_l \rangle - \frac{1}{3} \langle c_i \rangle^2 \delta_{kl} \right), \quad (2.13)$$

$$p_i - p_i^* = \frac{1}{3} n_i m_i \langle c_i \rangle^2, \quad (2.14)$$

with  $\vec{c}_i$  the peculiar velocity of a particle of species  $i$  with respect to the bulk velocity and  $\langle \rangle$  denoting integration over velocity space. Summation of the transformed pressure and viscous stress tensor does yield the total pressure  $p$  and viscous stress tensor  $\bar{\bar{\pi}}$ :

$$\sum_i \bar{\bar{\pi}}_i = \bar{\bar{\pi}}, \quad (2.15)$$

$$\sum_i p_i = p. \quad (2.16)$$

Since in a collision dominated plasma the differences between the two velocity representations are small [12], the viscous stress tensor and pressure in the bulk velocity

frame can be substituted in (2.12). Summation of the momentum balances over all species gives the global momentum balance or Navier-Stokes equations:

$$\frac{\partial \rho \vec{v}}{\partial t} + \nabla \cdot (\rho \vec{v} \vec{v}) = -\nabla p - \nabla \cdot \vec{\pi} + \vec{j} \times \vec{B} + \rho \sigma^c \vec{E}, \quad (2.17)$$

with  $\vec{B}$  the magnetic field and  $\vec{E}$  the electric field. The global momentum balance is solved together with the mass balance (2.9) to calculate the velocity field and the pressure. The solution procedure of these flow equations is explained in Chapter 7. The species momentum balances (2.12), are often not solved in the multi-fluid approach. Instead, the diffusion velocities necessary for solving (2.8), are calculated from a simplified version of (2.12). In this thesis we will use the Stefan-Maxwell diffusion model, which will be further discussed in Section 2.2 and Chapters 4, 5 and 6.

### 2.1.3 Energy conservation

The second moment of the Boltzmann Transport equation, the energy balance, is obtained by multiplying (2.1) by  $\frac{1}{2} m_i w^2$  and integrating over velocity space. Written in terms of the species specific enthalpy  $h_i$  the energy balance for species  $i$  reads:

$$\frac{\partial}{\partial t} (\rho y_i h_i) + \nabla \cdot (\rho \vec{v} y_i h_i) + \nabla \cdot \vec{q}_i + \vec{\pi} : \nabla \vec{v} - \vec{v} \cdot \nabla p_i = Q_i, \quad (2.18)$$

with  $\vec{q}_i$  the heat flux and  $Q_i$  the exchange of heat between the different species. When it is assumed that the specific heat of a species is constant over temperature, the specific enthalpy  $h_i$  of species  $i$  can be written as:

$$h_i = h_i^0 + c_{pi} T_i, \quad (2.19)$$

with  $h_i^0$  the specific enthalpy of formation at reference temperature  $T_0$ ,  $c_{pi}$  the specific heat of the  $i$ th species and  $T_i$  the temperature of species  $i$ . The assumption that  $c_{pi}$  is constant is not a fundamental restriction. In cases where the assumption that  $c_{pi}$  is constant is not accurate enough, it is possible to use accurate polynomial fits from literature. Note that there are no source terms explicitly describing the energy gain or loss through inelastic processes in equation (2.18). These loss terms are hidden in the transport terms  $\nabla \cdot (\rho \vec{v} y_i h_i)$ ,  $\nabla \cdot \vec{q}_i$  and  $Q_i$ . The source terms will appear when we rewrite equation (2.18) in terms of the temperature.

In practice, the energy balances are not solved for all species separately. It is assumed that the electrons, due to their light mass, will pick up the energy of electromagnetic fields  $Q_{\text{Ohm}}$  and that viscous dissipation can be neglected for the electrons. By collisions, electrons transfer part of their energy to the heavy particles. However, due to the ineffective energy transfer between the electrons and the heavy particles, the electron and heavy particle temperature will differ. Therefore, separate balances

are solved for the electron and the heavy particle enthalpy:

$$\begin{aligned} \frac{\partial}{\partial t} \left( \sum_{i \neq e} \rho y_i h_i \right) + \nabla \cdot \left( \sum_{i \neq e} \rho \vec{v}_i y_i h_i \right) &= -\nabla \cdot \vec{q}_h - \bar{\bar{\pi}} : \nabla \vec{v} + \vec{v} \cdot \nabla p_h + Q_{eh}, \\ \frac{\partial}{\partial t} (\rho y_e h_e) + \nabla \cdot (\rho \vec{v} h_e) &= -\nabla \cdot \vec{q}_e + \vec{v} \cdot \nabla p_e + Q_{Ohm} - Q_{eh}, \end{aligned} \quad (2.20)$$

where  $\vec{q}_h$  is the heavy particle heat flux,  $\vec{q}_e$  the electron heat flux,  $p_h$  and  $p_e$  the heavy particle and electron partial pressure respectively and  $Q_{eh}$  the energy exchange between the electrons and the heavy particles.

To solve for the heavy particle and electron temperatures  $T_h$  and  $T_e$ , the balances (2.20) need to be rewritten in terms of the temperatures, rather than the enthalpies. However, to do so, the expressions for the heat fluxes  $\vec{q}_e$  and  $\vec{q}_h$  must be known. The expressions for the transport fluxes will be discussed in the next section.

## 2.2 Transport fluxes

To close the system of equations for mass, momentum and energy transport, the diffusion velocities  $\vec{v}_i$ , the viscous stress tensor  $\bar{\bar{\pi}}$  and the heat fluxes  $\vec{q}_e$  and  $\vec{q}_h$  must be specified. They are defined as:

$$\begin{aligned} \vec{v}_i &= \langle \vec{c}_i \rangle, \\ (\bar{\bar{\pi}}_i)_{kl} &= -n_i m_i \langle (\vec{c}_i)_k (\vec{c}_i)_l - \frac{1}{3} c_i^2 \delta_{kl} \rangle, \\ \vec{q}_i &= \frac{1}{2} n_i m_i \langle c_i^2 \vec{c}_i \rangle. \end{aligned}$$

Note that the influence of the internal degrees of freedom on the transport fluxes is not taken into account in a formal way. However, the internal degrees of freedom are taken into account in the calculation of the heat capacity in a more pragmatic way, as in [15]. Above expressions are not useful for simulation purposes. Instead, expressions for the transport fluxes in terms of  $y_i$ ,  $\vec{v}$ ,  $T_e$  and  $T_h$  are required. Since the distribution function  $f_i$  is normally not known, approximations to the distribution function have to be made to obtain manageable expressions for the fluxes. When the plasma is in equilibrium, there are no gradients in the composition, velocity and temperature of the plasma. In this case the distribution function is given by the Maxwellian distribution:

$$f_i = n_i (m_i / 2\pi kT)^{3/2} \exp(-m_i v_i^2 / 2kT). \quad (2.21)$$

When the plasma is not in equilibrium, the distribution function  $f_i$  satisfies the Boltzmann transport equation as given in (2.1).

If the conditions in the plasma are only slightly different from equilibrium, the distribution function is nearly Maxwellian and a perturbation method can be used to



solve the Boltzmann transport equation (2.1). The solution can then be used to obtain expressions for the fluxes and the transport coefficients. Only in near-equilibrium conditions the usual definitions for the transport coefficients are valid, which means that the fluxes are linear in the gradients of the composition, velocity and temperature.

### 2.2.1 The isotropic case

In an unmagnetized plasma, the first approximation in the Chapman-Enskog expansion gives the following expression for the diffusion velocity [16]:

$$\vec{v}_i = - \sum_j D_{ij} \vec{d}_j, \quad (2.22)$$

where  $D_{ij}$  is the multicomponent diffusion coefficient matrix and  $\vec{d}_i$  is the diffusion driving force for species  $i$ . The diffusion driving force is given by:

$$\vec{d}_i = \nabla x_i + (x_i - y_i) \frac{\nabla p}{p} + \frac{\rho}{p} \sum_j y_j y_j (\vec{b}_i - \vec{b}_j), \quad (2.23)$$

where  $x_i$  is the mole fraction of species  $i$  and  $\vec{b}_i$  the body force acting on species  $i$ . The viscosity tensor is given by the following expression:

$$\bar{\pi} = -\mu \left( \nabla \vec{v} + (\nabla \vec{v})^T - \frac{2}{3} \nabla \cdot \vec{v} \bar{I} \right), \quad (2.24)$$

where  $\mu$  is the dynamic viscosity. Finally, the heat flux can be expressed as:

$$\vec{q}_h = -\lambda_h \nabla T_h + \sum_{i \neq e} \rho y_i h_i \vec{v}_i \quad (2.25)$$

$$\vec{q}_e = -\lambda_e \nabla T_e + \rho y_e h_e \vec{v}_e, \quad (2.26)$$

with  $\lambda_h$  and  $\lambda_e$  the heat conductivity of the heavy particles and the electrons, respectively. With these expressions for the heat flux, we can now rewrite the enthalpy balances to equations for the heavy particle and electron temperature. By substituting (2.25) and (2.26) in the enthalpy balances (2.20) and using the species continuity equations (2.8), we obtain:

$$\begin{aligned} \frac{\partial}{\partial t} \left( \sum_{i \neq e} \rho y_i c_{pi} T_h \right) + \nabla \cdot \left( \sum_{i \neq e} \rho \vec{v}_i y_i c_{pi} T_h \right) - \nabla \cdot (\lambda_h \nabla T_h) = \\ -\bar{\pi} : \nabla \vec{v} + \vec{v} \cdot \nabla p_h + Q_{eh} + \sum_{i \neq e} m_i \omega_i h_i^0, \end{aligned} \quad (2.27)$$

$$\begin{aligned} \frac{\partial}{\partial t} (\rho y_e c_{pe} T_e) + \nabla \cdot (\rho \vec{v}_e y_e c_{pe} T_e) - \nabla \cdot (\lambda_e \nabla T_e) = \\ \vec{v} \cdot \nabla p_e + Q_{Ohm} - Q_{eh}. \end{aligned} \quad (2.28)$$

Note that the contributions  $\sum_{i \neq e} \rho \vec{v}_i y_i c_{pi} T_h$  and  $\rho \vec{v}_e h_e$  are neglected.

To obtain the coefficients  $D_{ij}$ ,  $\mu$ ,  $\lambda_h$  and  $\lambda_e$  in the transport fluxes above, transport linear systems have to be solved. For the diffusion system this is discussed in Chapters 4 and 5. For all other coefficients simpler approximations are used. Unless stated otherwise, Frost mixture rules [17] are used for the transport properties of the electrons and the mixture rules of Mitchner and Kruger [14] are used for the heavy particle properties.

### 2.2.2 The anisotropic case

The behavior of a plasma is strongly affected by the presence of a magnetic field. Magnetic fields make the transport phenomena of the plasma direction dependent: they introduce anisotropy. Normally, without a magnetic field, particles in a plasma move randomly with their thermal velocity. Due to collisions, mass, momentum and energy of these particles is redistributed. In a magnetic field, charged particles spiral around the magnetic field lines. This spiraling motion causes the anisotropy in transport along, across and around the magnetic field lines. The motion of the particles across and around the field lines is coupled by the Lorentz force.

Consider the motion of electrons and ions in a plasma. In a magnetic field, electrons and ions spiral around the field lines with the Larmor frequency  $\Omega_i$  due to the Lorentz force. The Larmor frequency is determined by the charge  $q_i$  of the particle, the magnetic field strength  $B$  and the mass  $m_i$  of the particle:

$$\Omega_e = q_e B / m_e, \quad \Omega_p = q_p B / m_p. \quad (2.29)$$

Electrons are indicated by the subscript  $e$ , while ions are indicated by a  $p$ . The spiraling motion of the electrons and ions with mean energy  $kT_i$  around the field lines has Larmor radius  $\ell_i$ , which is given by [18]:

$$\ell_e = \frac{\sqrt{2kT_e/m_e}}{\Omega_e}, \quad \ell_p = \frac{\sqrt{2kT_h/m_p}}{\Omega_p}, \quad (2.30)$$

where  $T_e$  and  $T_h$  are the electron and heavy particle temperature, respectively. If a particle can make more than one turn around the field line before having a collision, the particle is called magnetized. For a strongly magnetized electron this means:  $\Omega_e \gg \nu_e$ , with  $\nu_e$  the electron collision frequency.

In a plasma without a magnetic field, particles can move in a certain direction until they collide with another particle. Therefore, the typical step size in the random walk motion is the mean free path for collisions. When the plasma is magnetized this situation is different. In the direction along the magnetic field the mean free path still determines the typical step size. Across the magnetic field the charged particles are confined within the Larmor radius around the field lines. Therefore, the typical step size for transport across the field is the Larmor radius.

As a result of the anisotropy, the components of the multicomponent diffusion coefficient matrix are no longer scalars but tensors. The diffusion velocity is expressed

in terms of these tensor components along ( $\parallel$ ), across ( $\perp$ ) and around ( $\odot$ ) the magnetic field lines as:

$$\vec{v}_i = - \sum_j \left( D_{ij}^{\parallel} d_j^{\parallel} + D_{ij}^{\perp} (d_j^{\perp} + d_j^{\odot}) + D_{ij}^{\odot} (d_j^{\perp} - d_j^{\odot}) \right). \quad (2.31)$$

In the above expression, use has been made of the cylindrical symmetry of Magnum-PSI and the fixed (axial) magnetic field. In this situation, the fixed cylindrical basis ( $\vec{e}_r, \vec{e}_\phi, \vec{e}_z$ ) can be introduced and any vector  $\vec{x}$  can then be written as  $\vec{x} = x^{\perp} \vec{e}_r + x^{\odot} \vec{e}_\phi + x^{\parallel} \vec{e}_z$ , where  $x^{\perp}$ ,  $x^{\odot}$  and  $x^{\parallel}$  are scalars. Note this is not the usual notation that can be found in for example Ferziger and Kaper [19]. Usually,  $x^{\perp}$ ,  $x^{\odot}$  and  $x^{\parallel}$  are vectors since it is not possible to fix the magnetic field. In Chapter 6 calculation of the tensor components  $D_{ij}^{\parallel}$ ,  $D_{ij}^{\perp}$  and  $D_{ij}^{\odot}$  is discussed. Again, for the other coefficients we use a simpler approach. The isotropic heat conduction coefficients are adjusted to take into account the effect of magnetization in the following manner:

$$\lambda_i^{\perp} = \frac{1}{1 + (\Omega_i \nu_i)^2} \lambda_i^{\parallel}. \quad (2.32)$$

When there is no magnetic field, these expressions yield the normal (parallel) coefficients. Since the momentum is mainly carried by the heavy particles, the effect of the magnetic field on the viscosity is ignored. This is a reasonable assumption when the ion density is low compared to the neutral density or when the ions are not magnetized.

### 2.3 Final form

To conclude this chapter, we will give an overview of the equations to be solved. In this thesis, we restrict ourselves to steady, quasi-neutral plasmas. In this case the balances for mass, charge, momentum and energy conservation read:

$$\nabla \cdot (\rho y_i \vec{v}) + \nabla \cdot (\rho y_i \vec{v}_i) = m_i \omega_i, \quad (2.33)$$

$$\nabla \cdot (\rho \vec{v}) = 0, \quad (2.34)$$

$$\nabla \cdot \vec{j} = 0, \quad (2.35)$$

$$\nabla \cdot (\rho \vec{v} \vec{v}) = -\nabla p - \nabla \cdot \vec{\pi} + \vec{j} \times \vec{B}, \quad (2.36)$$

$$\sum_{i \neq e} \nabla \cdot (\rho \vec{v}_i y_i c_{pi} T_h) - \nabla \cdot (\lambda_h \nabla T_h) = -\vec{\pi} : \nabla \vec{v} + \vec{v} \cdot \nabla p_h + Q_{eh} + \sum_{i \neq e} m_i \omega_i h_i^0, \quad (2.37)$$

$$\nabla \cdot (\rho \vec{v}_e y_e c_{pe} T_e) - \nabla \cdot (\lambda_e \nabla T_e) = \vec{v} \cdot \nabla p_e + Q_{Ohm} - Q_{eh}. \quad (2.38)$$

The next chapter is devoted to the numerical strategies needed for solving this set of partial differential equations.

## Chapter 3

# Numerical strategies

The coupled discretization scheme presented in this chapter is based on:  
*Extension of the Complete Flux Scheme to Systems of Conservation Laws*,  
Ten Thijs Boonkkamp, J.H.M., Dijk, J. van, Liu, L., Peerenboom, K.S.C.,  
Accepted for publication in Journal of Scientific Computing

In this chapter the numerical strategies for solving the equations as presented in Chapter 2 are described. Special attention is paid to the discretization of the system of species continuity equations.

### 3.1 Numerical modeling

As discussed in Chapter 2, the plasma that we want to model can be treated with the fluid description. In this fluid description, finding a numerical solution involves solving the set of partial differential equations (PDE's) for mass, momentum and energy conservation, as derived in Chapter 2. The first step in numerically solving these PDE's is discretization. By discretization the continuous equations, describing the variables on all points in space and time, are transformed to discrete equations describing these quantities only on a finite number of grid points and time levels. The resulting algebraic systems for the variables on all grid points need to be solved. Iterations of the above steps are performed until a converged solution is obtained.

### 3.2 Finite volume discretization

In general the balance equations as presented in Chapter 2 cannot be solved analytically; the equations need to be discretized. In this section we will discuss discretization of scalar stationary continuity equations and systems of stationary continuity equations with cell-centered finite volumes on a one-dimensional grid.

For discretization in Plasimo, a grid with boundary fitted ortho-curvilinear (OCL) coordinates is used. This means that the boundaries of the regions of interest co-

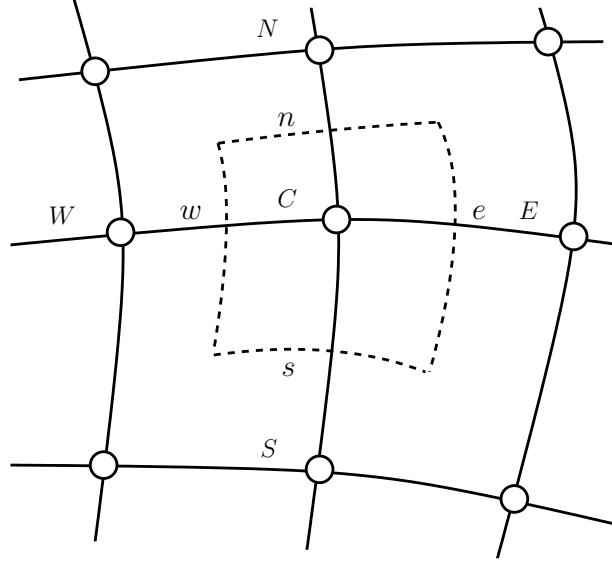


**Figure 3.1:** Control volume in ortho-curvilinear coordinates.

incide with coordinate lines of the coordinate system that is used. In this coordinate system an arbitrary geometry is mapped onto an equidistant computational grid. Plasimo uses an elliptic grid generation module [20], which constructs such meshes in two dimensions. In addition, it supports the usual standard coordinate systems (Cartesian, cylindrical, spherical) for one-, two- and three-dimensional simulations. In order to control the grid density on a per-coordinate basis, the code allows the user to specify stretch functions, as discussed in [21].

For clarity, only one (Cartesian) coordinate will be considered in the presentation of the discretization schemes in Section 3.2.1 and 3.2.2. The schemes are, however, not limited to 1D Cartesian grids, as will be briefly motivated here. The continuity equations that need to be discretized have the general form:

$$\nabla \cdot \vec{J} = s, \quad (3.1)$$

with  $\vec{J}$  the total flux and  $s$  the source. Integration of this continuity equation over a volume  $V$  and applying Gauss divergence theorem gives:

$$\oint_{\partial V} \vec{J} \cdot \vec{n} dA = \int_V s dV. \quad (3.2)$$

Consider the control volume in ortho-curvilinear coordinates as given in Figure 3.1. Since the control volume boundaries are perpendicular to the coordinates, equation (3.2) reduces to:

$$J_e A_e - J_w A_w + J_n A_n - J_s A_s = s_C \Delta V, \quad (3.3)$$

where the subscripts  $e$ ,  $w$ ,  $n$  and  $s$  refer to the east, west, north and south interface of the control volume, respectively. The volume of the control volume is denoted by

$\Delta V$ , while the areas of the east, west, north and south interfaces are given by  $A_e$ ,  $A_w$ ,  $A_n$  and  $A_s$ , respectively. In 1D and 3D the results are similar:

$$J_e A_e - J_w A_w = s_C \Delta V, \quad (3.4)$$

$$J_e A_e - J_w A_w + J_n A_n - J_s A_s + J_u A_u - J_d A_d = s_C \Delta V, \quad (3.5)$$

with  $u$  and  $d$  indicating the up and down interface of the control volumes. The difference between 1D, 2D and 3D in OCL coordinates is thus that the flux differences have to be considered and summed in 1, 2 or 3 directions<sup>1</sup>, respectively. Furthermore, the calculation of the lengths, areas and volumes is different. For example, in 1D Cartesian coordinates the areas  $A_e$  and  $A_w$  have value 1 m<sup>2</sup>, while in 3D Cartesian coordinates these areas are calculated as  $\Delta y \Delta z$ . Since, by the above considerations, the extension of the discretization schemes to higher dimensions and general ortho-curvilinear coordinates is relatively simple, only one (Cartesian) coordinate will be considered.

For time dependent problems, integration over the time step  $\Delta t$  has to be done in addition to integration over the control volumes. Both for the scalar and the coupled case this time integration can be done using the usual methods (implicit, explicit, Crank-Nicolson) [22, 23]. Therefore this extension is omitted as well. We will focus on the spatial discretization, which cannot be done with the usual methods [22, 23] for the case the fluxes are coupled.

### 3.2.1 Scalar convection-diffusion equations

In the one-dimensional case, the scalar continuity equation can be written as:

$$\frac{dJ}{dx} = s, \quad J = \rho u \phi - \Gamma \frac{d\phi}{dx}, \quad (3.6)$$

where  $J$  and  $u$  are the flux and the velocity in the  $x$  direction,  $s$  is the source,  $\rho$  the mass density and  $\Gamma$  is a scalar transport coefficient. Figure 3.2 gives the stencil used for discretization;  $C$ ,  $W$  and  $E$  denote the central, west and east nodal grid points, respectively. The west and east cell interfaces are denoted by  $w$  and  $e$ . Integration of equation (3.6) over the control volume shown in Figure 3.2 gives:

$$J_e - J_w = s_C \Delta x, \quad (3.7)$$

where  $s_C$  is the source term at the central point  $C$ . When the flux  $J_e$  is expressed linearly in  $\phi_C$  and  $\phi_E$ , and the flux  $J_w$  is expressed linearly in  $\phi_C$  and  $\phi_W$ , the following discrete equation is obtained:

$$a_C \phi_C = a_E \phi_E + a_W \phi_W + s_C \Delta x. \quad (3.8)$$

<sup>1</sup>When cross-fluxes are taken into account the different directions cannot be considered independently.

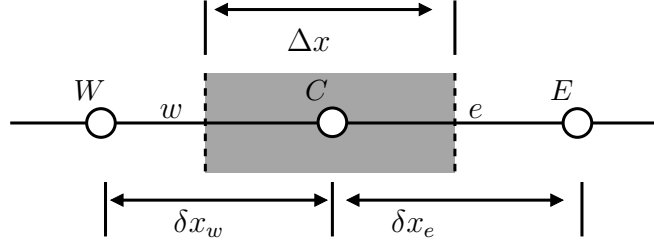


**Figure 3.2:** Stencil used for discretization.  $C$ ,  $W$  and  $E$  denote the central, west and east nodal grid points, respectively. The west and east cell interfaces are denoted by  $w$  and  $e$ .

The discretization coefficients  $a_C$ ,  $a_E$  and  $a_W$  depend on the expressions for the flux. The most straightforward choice for expressing the fluxes  $J_e$  and  $J_w$  in  $\phi_E$ ,  $\phi_C$  and  $\phi_W$  is to assume a piecewise linear profile for  $\phi$ , which results in:

$$J_e = \frac{1}{2}(\rho u)_e (\phi_E + \phi_C) - \Gamma_e \frac{\phi_E - \phi_C}{\delta x_e}, \quad (3.9)$$

$$J_w = \frac{1}{2}(\rho u)_w (\phi_W + \phi_C) - \Gamma_w \frac{\phi_C - \phi_W}{\delta x_w}. \quad (3.10)$$

The discretization coefficients are then given by:

$$\begin{aligned} a_E &= \frac{\Gamma_e}{\delta x_e} \left( 1 - \frac{1}{2} P_e \right), \\ a_W &= \frac{\Gamma_w}{\delta x_w} \left( 1 + \frac{1}{2} P_w \right), \\ a_C &= a_E + a_W + (\rho u)_e - (\rho u)_w, \end{aligned} \quad (3.11)$$

with  $P_e = (\rho u)_e \delta x_e / \Gamma_e$  and  $P_w = (\rho u)_w \delta x_w / \Gamma_w$  the Péclet number at the east and west interface, respectively. This scheme is usually referred to as the *central difference scheme*. It can be seen that in the case of dominant advection when the Péclet number  $|P| > 2$ ,  $a_E$  or  $a_W$  can become negative. This is a violation of the basic rules for discretization [22] and will result in unphysical solutions. This can be explained as follows. If we assume that there are no sources, then we expect that  $\phi_C$  is a weighted average of  $\phi_E$  and  $\phi_W$ . However, since  $\phi_C$  is expressed by:

$$\phi_C = \frac{a_W}{a_E + a_W} \phi_W + \frac{a_E}{a_E + a_W} \phi_E \equiv f \phi_W + (1 - f) \phi_E, \quad (3.12)$$

this is only an interpolation when  $0 < f < 1$ . This requires that all discretization coefficients have the same sign. The convention is to choose all coefficients positive.

Since one of the features of Magnum PSI is the transonic flow field, the central difference scheme cannot be used for our application. Instead the *exponential scheme* [22, 24] will be used. In the exponential scheme, the flux expression is not based on a piecewise linear profile for  $\phi$ , but on a local exact solution of the homogeneous equation with constant coefficients. When  $\Gamma$  is constant the exact solution of the scalar

convection-diffusion equation is known. This knowledge can be used to construct a discretization scheme. To derive an expression for the flux  $J_e$ , the following boundary value problem for the unknown  $\phi$  is solved:

$$\begin{aligned} \frac{dJ}{dx} = \frac{d}{dx} \left( (\rho u)_e \phi - \Gamma_e \frac{d\phi}{dx} \right) &= 0, & x_C < x < x_E, \\ \phi(x_C) &= \phi_C, \\ \phi(x_E) &= \phi_E. \end{aligned} \quad (3.13)$$

The flux is then given by:

$$J_e = \frac{1}{\delta x_e} \Gamma_e \left( B(-P_e) \phi_C - B(P_e) \phi_E \right), \quad (3.14)$$

where the Péclet number  $P_e$  is defined as  $P_e = (\rho u)_e \delta x_e / \Gamma_e$  and the Bernoulli function is given by:

$$B(z) = \frac{z}{e^z - 1}, \quad B(0) = 1. \quad (3.15)$$

The Bernoulli function is plotted in Figure 3.3. A similar expression can be obtained

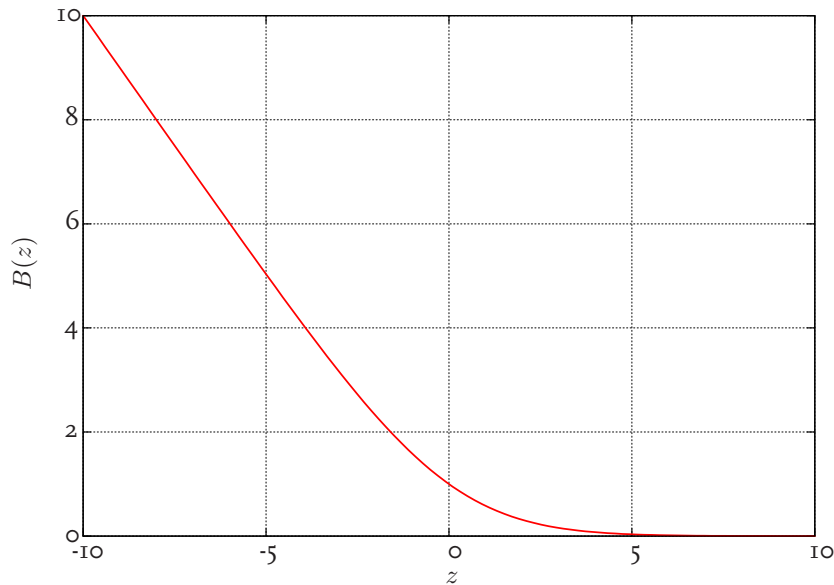


Figure 3.3: Bernoulli function.

for the flux at the west interface. Substitution of the expressions for the fluxes in equation (3.7) gives the discretization coefficients:

$$\begin{aligned} a_E &= \frac{1}{\delta x_e} \Gamma_e B(P_e), \\ a_W &= \frac{1}{\delta x_w} \Gamma_w B(-P_w), \\ a_C &= a_E + a_W + (\rho u)_e - (\rho u)_w. \end{aligned} \quad (3.16)$$



The exponential scheme does not produce unphysical solutions for dominant flow since all discretization coefficients are positive. The positiveness of the coefficients for all Péclet numbers can be directly deduced from the plot of the Bernoulli function in Figure 3.3. However, the suppression of unphysical oscillations is at the expense of the order of the scheme. For dominant flow, the exponential scheme reduces to the upwind scheme and is only first order accurate as opposed to the second order accuracy of the central difference scheme.

### 3.2.2 Systems of convection-diffusion equations

The species mass fractions cannot be described by a scalar continuity equation for each species separately. Instead, they are described by a system of coupled continuity equations. In the steady, one-dimensional case, this system of continuity equations (4.10) can be written as

$$\frac{d}{dx} \mathbf{J} = \mathbf{s}, \quad \mathbf{J} = \rho u \phi - \Gamma \frac{d}{dx} \phi, \quad (3.17)$$

where the different species in the vector  $\phi$  are coupled by the non-diagonal elements of  $\Gamma$ . The grid stencil used for discretization is again given by Figure 3.2. Integration of equation (3.17) over the control volume shown in Figure 3.2 gives:

$$\mathbf{J}_e - \mathbf{J}_w = \mathbf{s}_C \Delta x, \quad (3.18)$$

where  $s_C$  is the source term at the central point  $C$ . When the flux  $\mathbf{J}_e$  is expressed in  $\phi_C$  and  $\phi_E$ , and the flux  $\mathbf{J}_w$  is expressed in  $\phi_C$  and  $\phi_W$ , the following discrete equation is obtained:

$$\mathbf{A}_C \phi_C = \mathbf{A}_E \phi_E + \mathbf{A}_W \phi_W + \mathbf{s}_C \Delta x. \quad (3.19)$$

The discretization matrices  $\mathbf{A}_C$ ,  $\mathbf{A}_E$  and  $\mathbf{A}_W$  depend on the expressions for the numerical flux.

Section 3.2.2 will describe the discretization of the fluxes with the traditional (scalar) exponential scheme as discussed in the previous section. With this scalar exponential scheme, unphysical oscillations cannot be excluded. To overcome this problem, a more general, coupled form of the exponential scheme is introduced.

#### The scalar exponential scheme

Since traditional discretization schemes are designed for scalar convection-diffusion equations, they cannot directly be applied to the fluxes  $\mathbf{J}_e$  and  $\mathbf{J}_w$ , but they *can* be applied to the individual components  $J_{i,e}$  and  $J_{i,w}$  of the flux. The flux at the east interface  $J_{i,e}$  of species  $i$  can be approximated by applying the exponential scheme [22, 23] to the different contributions of the flux:

$$J_{i,e} = \frac{1}{\delta x_e} \sum_j \Gamma_{ij} (B(-P_{ij,e}) \phi_{j,C} - B(P_{ij,e}) \phi_{j,E}), \quad (3.20)$$

where the Péclet number  $P_{ij,e}$  is defined as  $P_{ij,e} = \rho u \delta x_e / \Gamma_{ij}$ . A similar expression can be obtained for the flux at the west interface. Substitution of the expressions for the fluxes in equation (3.18) gives the discretization coefficients:

$$\begin{aligned} A_{E,ij} &= \frac{1}{\delta x_e} \Gamma_{ij} B(P_{ij,e}), \\ A_{W,ij} &= \frac{1}{\delta x_w} \Gamma_{ij} B(-P_{ij,w}), \\ A_{C,ij} &= A_{E,ij} + A_{W,ij}. \end{aligned} \quad (3.21)$$

Note that in the expression for  $A_{C,ij}$ , it is assumed that the mass flux density  $\rho \vec{v}$  is divergence free. Although the exponential scheme does not produce unphysical oscillations for scalar convection-diffusion equations, unphysical oscillations can occur for systems of equations in the case of dominant advection. We found that oscillations appear when the discretization matrices contain negative eigenvalues. This restriction on the eigenvalues can be seen as the generalization of the positive coefficients restriction [22] to systems of convection-diffusion equations.

The reason that negative eigenvalues can occur is that the exponential scheme is based on the exact solution of a local boundary value problem of a *scalar* convection-diffusion equation without sources and constant coefficients. To avoid oscillations in the system case, the scheme must be based on the exact solution of a local boundary value problem of a *system* of convection-diffusion equations without sources and constant coefficients. Such a scheme will be presented in the next section.

### The coupled exponential scheme

In this section, a generalization of the exponential scheme will be introduced. The scheme is a special case of the scheme presented in [25]. In [25] the representation of the flux is based on the solution of a local boundary value problem for the entire system of equations, including the source terms. In the present work, the flux representation is based on the homogeneous solution of the local boundary value problem; i.e. without sources. The difference between the discretization scheme in this work and [25] can be compared with the difference between the exponential scheme and the complete-flux scheme for scalar advection diffusion reaction equations ([22] vs [26]).

To derive an expression for the flux  $\mathbf{J}_e$ , the following system boundary value problem for the vector  $\phi$  of unknowns is used:

$$\begin{aligned} \frac{d}{dx} \mathbf{J} &= \frac{d}{dx} \left( (\rho u)_e \phi - \Gamma_e \frac{d}{dx} \phi \right) = \mathbf{0}, & x_C < x < x_E, \\ \phi(x_C) &= \phi_C, \\ \phi(x_E) &= \phi_E, \end{aligned} \quad (3.22)$$

where  $(\rho u)_e$  and  $\Gamma_e$  are assumed to be constant on  $(x_C, x_E)$ . Note that (3.22) is equal to (3.17) in case  $s = 0$ . It is important to mention here that neglecting the source in

the derivation of the flux, does not limit the application of the discretization scheme to problems without sources. The only consequence is that uniform second order convergence is not guaranteed by the discretization scheme. Integration of (3.22) from  $x_e$  to  $x$  gives:

$$\mathbf{J}(x) - \mathbf{J}_e = \mathbf{0}. \quad (3.23)$$

If we define  $\mathbf{K}_e = (\rho u)_e \Gamma_e^{-1}$ , the flux can be written as<sup>2</sup>:

$$\mathbf{J}(x) = -\Gamma_e e^{x\mathbf{K}_e} \frac{d}{dx} (e^{-x\mathbf{K}_e} \phi). \quad (3.24)$$

Substitution of this expression for the flux in (3.23) yields:

$$-\Gamma_e e^{x\mathbf{K}_e} \frac{d}{dx} (e^{-x\mathbf{K}_e} \phi) - \mathbf{J}_e = \mathbf{0}. \quad (3.25)$$

After multiplication with  $e^{-x\mathbf{K}_e} \Gamma_e^{-1}$  we obtain:

$$\frac{d}{dx} (e^{-x\mathbf{K}_e} \phi) + e^{-x\mathbf{K}_e} \Gamma_e^{-1} \mathbf{J}_e = \mathbf{0}. \quad (3.26)$$

Integration from  $x_C$  to  $x_E$  gives:

$$e^{-x_E \mathbf{K}_e} \phi_E - e^{-x_C \mathbf{K}_e} \phi_C + \left( \int_{x_C}^{x_E} e^{-x\mathbf{K}_e} dx \right) \Gamma_e^{-1} \mathbf{J}_e = \mathbf{0}. \quad (3.27)$$

After left multiplication<sup>3</sup> with  $\mathbf{K}_e$  and calculation of the integral we find:

$$(e^{-x_C \mathbf{K}_e} - e^{-x_E \mathbf{K}_e}) \Gamma_e^{-1} \mathbf{J}_e = \mathbf{K}_e (e^{-x_C \mathbf{K}_e} \phi_C - e^{-x_E \mathbf{K}_e} \phi_E). \quad (3.28)$$

Introducing the Péclet matrix  $\mathbf{P}_e = \delta x_e \mathbf{K}_e$ , the following expression for the flux is obtained:

$$(e^{\mathbf{P}_e} - \mathbf{I}) \Gamma_e^{-1} \mathbf{J}_e = \mathbf{K}_e (e^{\mathbf{P}_e} \phi_C - \phi_E), \quad (3.29)$$

which can be rewritten as:

$$\mathbf{J}_e = \frac{1}{\delta x_e} \Gamma_e \left( B(-\mathbf{P}_e) \phi_C - B(\mathbf{P}_e) \phi_E \right). \quad (3.30)$$

The Bernoulli function of the Péclet matrix is calculated by diagonalization of the Péclet matrix:

$$\mathbf{P} = \mathbf{V} \mathbf{\Lambda} \mathbf{V}^{-1} = \mathbf{V} \begin{pmatrix} \lambda_1 & & \\ & \ddots & \\ & & \lambda_N \end{pmatrix} \mathbf{V}^{-1}, \quad (3.31)$$

$$B(\mathbf{P}) = \mathbf{V} B(\mathbf{\Lambda}) \mathbf{V}^{-1} = \mathbf{V} \begin{pmatrix} B(\lambda_1) & & \\ & \ddots & \\ & & B(\lambda_N) \end{pmatrix} \mathbf{V}^{-1}, \quad (3.32)$$

<sup>2</sup>The following properties are used: 1)  $\Gamma$  is regular, 2)  $\mathbf{K}$  and  $e^{-x\mathbf{K}}$  commute, 3)  $(e^{x\mathbf{K}})^{-1} = e^{-x\mathbf{K}}$ .

<sup>3</sup>Note that multiplication with  $\mathbf{K}$  can only be performed when  $\mathbf{K}$  is non-singular. A more rigorous derivation (allowing for singular  $\mathbf{K}$ ) is done in [25] and shows that the final result presented here is valid for singular  $\mathbf{K}$  as well.

with  $\mathbf{V}$  the matrix containing the eigenvectors of  $\mathbf{P}$  as its columns and  $\mathbf{\Lambda}$  a diagonal matrix with the eigenvalues  $\lambda_i$  of the Péclet matrix. Likewise,  $B(-\mathbf{P})$  can be computed. Note that for the diagonalization, it is required that  $\mathbf{P}$  has a complete set of linearly independent eigenvectors. In Cullinan [27] it is proven that for Péclet matrices resulting from multi-component diffusion problems this is indeed the case.

For the flux at the west interface, an expression similar to the east interface can be obtained. Substitution of the expression for the fluxes in equation (3.18), gives the following expressions for the discretization matrices:

$$\mathbf{A}_E = \frac{1}{\delta x_e} \mathbf{\Gamma}_e B(\mathbf{P}_e), \quad \mathbf{A}_W = \frac{1}{\delta x_w} \mathbf{\Gamma}_w B(-\mathbf{P}_w), \quad \mathbf{A}_C = \mathbf{A}_E + \mathbf{A}_W. \quad (3.33)$$

Similar to the scalar discretization, we have used the fact that the flow field  $\rho \vec{v}$  is divergence free in the expression for  $\mathbf{A}_C$ . From (3.32) it can be seen that the coupled exponential scheme guarantees that the eigenvalues of the discretization matrices are positive, since the eigenvalues of  $B(\mathbf{P})$  are given by  $B(\lambda_i)$ , which are always positive.

As can be seen in Table 3.1, the coupled exponential scheme and the traditional scalar exponential scheme have quite some similarities. In fact, the coupled exponential scheme decouples the system by changing to the basis of eigenvectors ( $\mathbf{P} = \mathbf{V} \mathbf{\Lambda} \mathbf{V}^{-1}$ ). In the decoupled system, the scalar exponential scheme is applied,  $B(\mathbf{P}) = \mathbf{V} B(\mathbf{\Lambda}) \mathbf{V}^{-1}$ . Application of other scalar discretization schemes (power law, hybrid [22, 23]) to the decoupled (diagonalized) system is possible as well.

Coupled	Scalar
$\mathbf{J}_e = \frac{1}{\delta x_e} \mathbf{\Gamma}_e (B(-\mathbf{P}_e) \phi_C - B(\mathbf{P}_e) \phi_E)$	$J_e = \frac{1}{\delta x_e} \Gamma_e (B(-P_e) \phi_C - B(P_e) \phi_E)$
$\mathbf{J}_w = \frac{1}{\delta x_w} \mathbf{\Gamma}_w (B(-\mathbf{P}_w) \phi_W - B(\mathbf{P}_w) \phi_C)$	$J_w = \frac{1}{\delta x_w} \Gamma_w (B(-P_w) \phi_W - B(P_w) \phi_C)$
$\mathbf{A}_E = \frac{1}{\delta x_e} \mathbf{\Gamma}_e B(\mathbf{P}_e)$	$a_E = \frac{1}{\delta x_e} \Gamma_e B(P_e)$
$\mathbf{A}_W = \frac{1}{\delta x_w} \mathbf{\Gamma}_w B(-\mathbf{P}_w)$	$a_W = \frac{1}{\delta x_w} \Gamma_w B(-P_w)$
$\mathbf{A}_C = \mathbf{A}_E + \mathbf{A}_W$	$a_C = a_E + a_W$

**Table 3.1:** Comparison of the traditional exponential scheme and its generalization to systems of convection-diffusion equations.

### 3.3 Source term linearization

In the previous section on discretization, the source term  $s_C$  was treated as a constant. However, in many cases the source term depends on the variable  $\phi$  itself. The production rate of electrons is, for example, dependent on the electron density. To take into account this dependency, the source term is linearized as follows:

$$s_C = C + P \phi_C, \quad (3.34)$$

where  $C$  is the *constant* part of  $s_C$  and  $P$  is the part of the source *proportional* to  $\phi_C$ . For numerical stability, the coefficient  $P$  must always be less than or equal to zero.

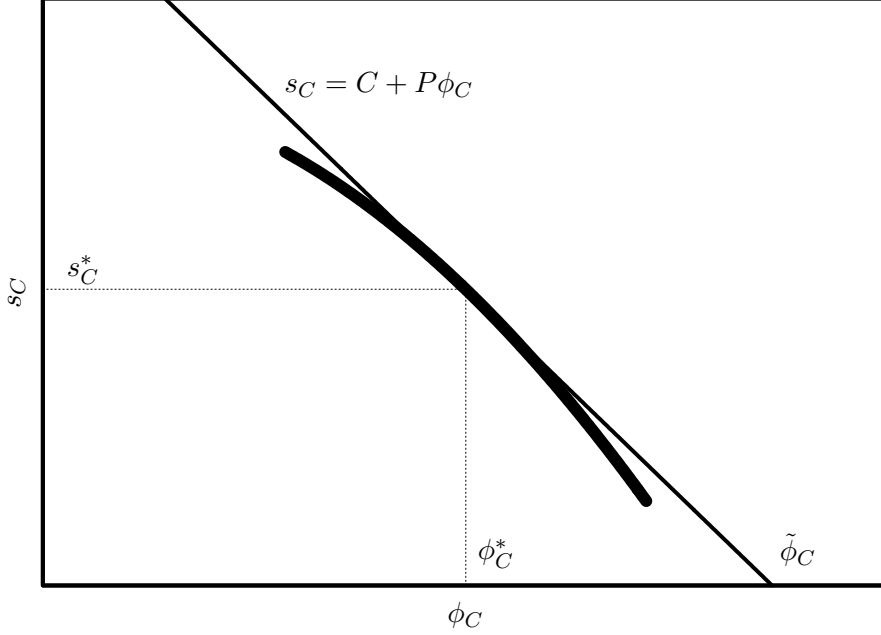


**Figure 3.4:** The solution in the source dominated limit.

Since convergence problems often arise when the source terms are very large, it is useful to consider source term linearization in the source dominated limit.

### 3.3.1 The source dominated limit

In the source dominated limit, transport can be neglected and the discrete equation (3.8) reduces to:

$$s_C = C + P\phi_C \approx 0. \quad (3.35)$$

The source dominated limit leads to the solution:

$$\phi_C = -\frac{C}{P}. \quad (3.36)$$

The source dominated limit can be used to design the linearization such that  $\phi_C$  stays within reasonable limits [22]. If we want the next iteration value of  $\phi_C$  to be close to a given value  $\tilde{\phi}_C$ , this can be arranged through the linearization:

$$C = \frac{s_C^* \tilde{\phi}_C}{\tilde{\phi}_C - \phi_C^*}, \quad P = -\frac{s_C^*}{\tilde{\phi}_C - \phi_C^*}. \quad (3.37)$$

Here  $s_C^*$  and  $\phi_C^*$  denote the current value of the (non-linearized) source term and  $\phi_C$  respectively. In Figure 3.4 the linearization is schematically depicted. The desired value  $\tilde{\phi}_C$  can be determined from physical considerations, for example that the mass

fractions of all the species must lie between 0 and 1. Because the linearization is based on the source dominated limit, the next iteration will not be exactly  $\tilde{\phi}_C$ , since also the transport terms in the discrete equation will influence it. Furthermore, by considering the source for the converged solution  $\phi_C = \phi_C^*$ , it can be seen that the linearization does not influence the final solution:

$$C + P\phi_C = \frac{s_C^* \tilde{\phi}_C}{\tilde{\phi}_C - \phi_C^*} - \frac{s_C^*}{\tilde{\phi}_C - \phi_C^*} \phi_C^* = s_C^*. \quad (3.38)$$

The linearization only changes the convergence path. It avoids rapid changes during the iteration process and physically unrealistic values. We will now use the source dominated limit to construct the linearization for the chemical source terms.

### 3.3.2 Linearization of the chemical sources

The chemical source terms in the continuity equations are non-linear functions of the species densities and can therefore vary strongly from iteration step to iteration step, causing poor convergence behavior. The strong variations can even lead to negative densities, thereby ruining the calculation. To prevent this, the source term linearization introduced in this section is constructed such that physically unrealistic results during iteration are avoided. The method is a generalization of [22], which is based on the source dominated limit of the discretized equations.

Physically realistic results need to fulfill the following two conditions:

1.  $\sum_i y_i = 1$ ,
2.  $0 \leq y_i \leq 1$ .

In Chapter 4 it will be proven that when  $\sum_i m_i \omega_i = 0$  and transport is dealt with correctly, condition 1 is fulfilled. However, this is true for constant sources  $m_i \omega_i$  and we have to be aware that this condition is not automatically guaranteed when the sources are linearized. Furthermore, there is no guarantee that condition 2 is fulfilled when chemical sources are present. The composition calculation can perfectly satisfy  $\sum_i y_i = 1$ , while not satisfying  $0 \leq y_i \leq 1$ . A mixture of two species with mass fractions of 1.5 and -0.5 respectively, is not physical. The linearization method should therefore linearize the sources in such a way that both condition 1 and 2 are fulfilled every iteration step.

In Figure 3.5 the solution domain that satisfies both condition 1 and 2 is graphically depicted by the dark gray triangle for a three species mixture. A correct solution lies on the part of the constraint plane  $\sum_i y_i = 1$  that is bounded by the planes  $y_i = 0$ . The current values of the source and mass fraction vector are denoted by  $s_C^*$  and  $y^*$ , respectively. Both  $s_C^*$  and  $y^*$  are in the plane  $\sum_i y_i = 1$ . From the direction of the source vector  $s_C^*$  and the current value of the mass fraction  $y^*$  we can determine which of the planes  $y_i = 0$  is encountered first. The intersection of  $s_C^*$  with this plane becomes the target  $\tilde{y}$  for linearization.

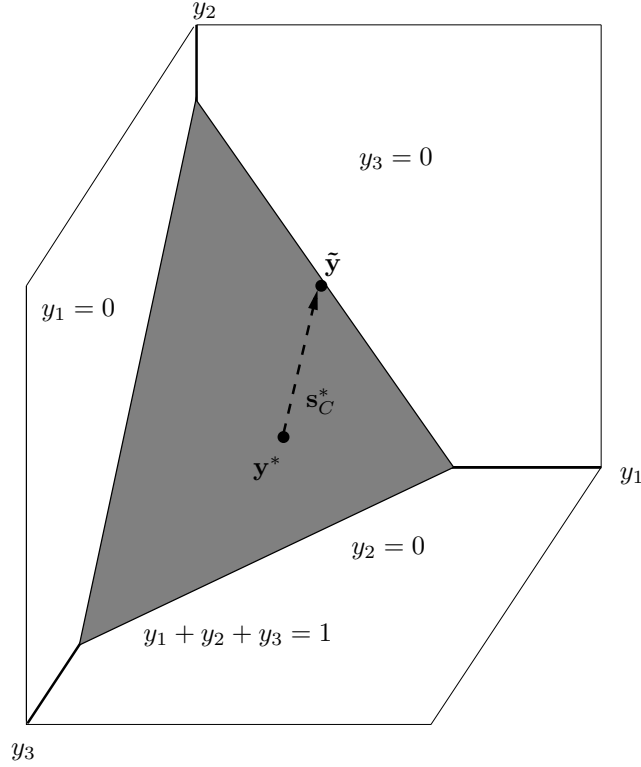


**Figure 3.5:** Constraint planes in a mixture with three species.

For  $N$  species, the constraint plane  $\sum_{i=1}^N y_i = 1$  is bounded by the  $N$  hyperplanes  $y_i = 0$ . The linearization target  $\tilde{\mathbf{y}}$  can be determined by calculating the intersection of the source line with all the bounding hyperplanes. The points  $\mathbf{y}$  on the source line can be parametrized as follows:

$$\mathbf{y} = \mathbf{y}^* + \zeta \mathbf{s}_C^*, \quad (3.39)$$

where  $\mathbf{s}_C^*$  is the source vector determining the direction of the line and  $\mathbf{y}^*$  is a point on the line. Because the origin is a point on all the bounding hyperplanes  $y_i = 0$ , the points  $\mathbf{y}$  on these planes can be described by:

$$\mathbf{n}_i \cdot \mathbf{y} = 0, \quad (3.40)$$

with  $\mathbf{n}_i$  the normal of the  $i$ th bounding hyperplane. The intersections of the source line with these planes are given by:

$$\zeta_i = -\frac{\mathbf{n}_i \cdot \mathbf{y}^*}{\mathbf{n}_i \cdot \mathbf{s}_C^*}. \quad (3.41)$$

For all  $N$  planes  $\zeta_i$  can be determined. The smallest positive  $\zeta_i$  gives the plane that should be aimed at in the linearization procedure. The target is then  $\tilde{\mathbf{y}} = \mathbf{y}^* +$

$\zeta_{\min} \mathbf{s}_C^*$ . Since differences in  $\zeta_{\min}$  from grid cell to grid cell can lead to a spiky mass fraction field when the sources are large,  $\zeta_{\min}$  is the minimum from all the bounding hyperplanes as well as from all the grid cells. Note that  $\zeta_{\min}$  also has a physical interpretation. When we consider the time dependent species continuity equations in the absence of transport,  $\frac{\partial \rho \mathbf{y}}{\partial t} = \mathbf{s}_C^*$ , the maximum time step that can be taken in an explicit time stepping method before the species mass fractions get negative is given by  $\tau = \rho \zeta_{\min}$ .

To avoid strong variations within one iteration step, we can use an underrelaxation factor  $\alpha$  and calculate  $\tilde{\mathbf{y}}$  according to:

$$\tilde{\mathbf{y}} = \alpha (\mathbf{y}^* + \zeta_{\min} \mathbf{s}_C^*) + (1 - \alpha) \mathbf{y}^* = \mathbf{y}^* + \alpha \zeta_{\min} \mathbf{s}_C^*. \quad (3.42)$$

For example, for  $\alpha = 0.5$  the linearization target  $\tilde{\mathbf{y}}$  lies halfway between the current value  $\mathbf{y}^*$  and the physical limit. The target value  $\tilde{\mathbf{y}}$  can now be used in the linearization coefficients for the different species:

$$C_i = \frac{s_{C,i}^* \tilde{y}_i}{\tilde{y}_i - y_i^*} = \frac{\tilde{y}_i}{\alpha \zeta_{\min}}, \quad P_i = -\frac{s_{C,i}^*}{\tilde{y}_i - y_i^*} = \frac{1}{\alpha \zeta_{\min}}, \quad (3.43)$$

where the subscript  $i$  refers to the  $i$ th species.

### 3.3.3 Linearization of the energy sources

Chemical reactions not only influence the chemical composition, but also contribute to the source terms for the energy equations. For the purpose of the discussion, it is assumed that only chemical reactions contribute to the energy sources for the moment. Similar to the chemical sources, the energy sources can give unrealistic solutions during iteration. For example, the energy gained by an association reaction can never be more than the number of atoms present times the association energy. Therefore, when the species mass fractions get negative, also the resulting energy source term will be unphysical. In the previous section, it was observed that the maximum time step that can be taken in an explicit time stepping method before the species mass fractions get negative is given by  $\tau = \rho \zeta_{\min}$ . Unphysical situations for the energy sources can therefore be prevented by taking the same time step.

Consider the electron temperature. In the source dominated limit, the temperature change as a result of the time step  $\tau$  will be:

$$\tilde{T}_e - T_e^* = \tau \frac{s_C^*}{c_e}, \quad (3.44)$$

where  $c_e$  is the electron heat capacity and  $s_C^*$  now contains the energy source term for the electrons due to chemical reactions. The value  $\tilde{T}_e$  gives the physical limit for the electron temperature. Using  $\tilde{T}_e$  as the target for linearization and making use of the same underrelaxation factor  $\alpha$  as in the previous section gives the following linearization coefficients:

$$C = s_C^* + \frac{c_e T_e^*}{\alpha \tau}, \quad P = -\frac{c_e}{\alpha \tau}. \quad (3.45)$$



The coefficients for the heavy particle temperature can be obtained similarly. The linearization presented prevents unphysical solutions where more chemical energy is added than is available in the plasma. Furthermore, by basing the linearization of the chemical and energy sources on the same time step, consistency between these sources is established.

### 3.4 Iteration and underrelaxation

The partial differential equations as presented in Chapter 2 are strongly non-linear. Furthermore, the different PDE's are coupled via the transport coefficients and source terms. Therefore, the equations are solved iteratively. The equations are linearized and the coefficients and source terms are calculated from the previous iteration. The model is said to be converged when the residual is below a preset tolerance, where the residual  $\xi$  is defined as:

$$\xi = \max_{i,j,N} \left| \frac{\Delta \Phi_{i,j}^N}{\Phi_{i,j}^N} \right|, \quad (3.46)$$

with  $\Phi_{i,j}^N$  the solution of equation  $N$  at gridpoint  $(i, j)$ . In this thesis the tolerance used is typically  $10^{-6}$ . To prevent divergence in the iterative solution it is often necessary to slow down the changes from iteration to iteration. This can be done with underrelaxation. In Plasimo, a relaxation factor, as described in Patankar [22] for scalar continuity equations, is used. This underrelaxation method is extended to systems of continuity equations.

Underrelaxation is taken into account by modification of the discretization coefficients and matrices. Starting from the discretized equation, for both the scalar and the system case:

$$\begin{aligned} a_C \phi_C &= a_E \phi_E + a_W \phi_W + b, \\ \mathbf{A}_C \phi_C &= \mathbf{A}_E \phi_E + \mathbf{A}_W \phi_W + \mathbf{b}, \end{aligned} \quad (3.47)$$

where  $b$  and  $\mathbf{b}$  contain the constant part of the linearized sources. The above equations can be reorganized as follows:

$$\begin{aligned} \phi_C &= \frac{a_E \phi_E + a_W \phi_W + b}{a_C}, \\ \phi_C &= \mathbf{A}_C^{-1} (\mathbf{A}_E \phi_E + \mathbf{A}_W \phi_W + \mathbf{b}). \end{aligned} \quad (3.48)$$

Let  $\phi_C^*$  and  $\phi_C^*$  be the values from the previous iteration. By adding and subtracting this value from equation (3.48) we get:

$$\begin{aligned} \phi_C &= \phi_C^* + \left( \frac{a_E \phi_E + a_W \phi_W + b}{a_C} - \phi_C^* \right), \\ \phi_C &= \phi_C^* + \left( \mathbf{A}_C^{-1} (\mathbf{A}_E \phi_E + \mathbf{A}_W \phi_W + \mathbf{b}) - \phi_C^* \right). \end{aligned} \quad (3.49)$$

The expression between the parentheses gives the change in the current iteration. To slow down this change, an underrelaxation parameter  $\alpha$  ( $0 < \alpha \leq 1$ ) can be introduced:

$$\begin{aligned}\phi_C &= \phi_C^* + \alpha \left( \frac{a_E \phi_E + a_W \phi_W + b}{a_C} - \phi_C^* \right), \\ \phi_C &= \phi_C^* + \alpha \left( \mathbf{A}_C^{-1} (\mathbf{A}_E \phi_E + \mathbf{A}_W \phi_W + \mathbf{b}) - \phi_C^* \right).\end{aligned}\quad (3.50)$$

It can be seen that for  $\alpha = 0$  the solution does not change, while for  $\alpha = 1$  the whole modification is taken into account. The case  $0 < \alpha < 1$  gives the intermediate situation where only part of the modification is taken into account. Rearranging equation (3.50) gives the modified discretization coefficients and matrices:

$$\begin{aligned}\frac{a_C}{\alpha} \phi_C &= a_E \phi_E + a_W \phi_W + b + (1 - \alpha) \frac{a_C}{\alpha} \phi_C^*, \\ \frac{\mathbf{A}_C}{\alpha} \phi_C &= \mathbf{A}_E \phi_E + \mathbf{A}_W \phi_W + \mathbf{b} + (1 - \alpha) \frac{\mathbf{A}_C}{\alpha} \phi_C^*.\end{aligned}\quad (3.51)$$

Note that when the iterations converge and  $\phi_C$  becomes equal to  $\phi_C^*$ , the original equation is satisfied. This should of course be a property of underrelaxation.

### 3.5 Matrix conditioning and solving

The discrete equations per control volume as presented in Section 3.2 can be assembled into a system matrix  $\mathbf{A}$ , from which the quantity  $\mathbf{x}$  on all the grid points can be computed:

$$\mathbf{A}\mathbf{x} = \mathbf{b}.\quad (3.52)$$

The vector  $\mathbf{b}$  contains the sources and the boundary conditions. In Plasimo, a number of solvers are available for solving the system (3.52). There are a number of iterative solvers such as BiConjugate Gradient (BiCG) and Quasi-Minimal Residual (QMR), that can use a preconditioner. Apart from the iterative solvers, two direct solvers are available: BandMatrixLU and SuperLU. When solving the pressure correction equation (see Chapter 7) and the system of mass balances of all species (Chapters 4, 5 and 6) it is crucial that mass conservation is fulfilled exactly. Therefore we use SuperLU for these equations, instead of (faster) iterative solvers.

To solve (3.52) for the mass fractions, an additional conditioning step is needed. Since the charge constraint is not applied explicitly, as will be discussed in Chapter 5, also the electron mass fraction is part of the solution vector  $\mathbf{x}$ . Due to the large mass ratio between the electrons and the heavy particles, the system matrix will be ill-conditioned. As a result, the mass and charge neutrality constraint, which are not explicitly applied, are not fulfilled satisfactory when electrons are present. To improve the conditioning of the system matrix, scaling of rows and columns is performed to obtain the modified system:

$$\tilde{\mathbf{A}}\tilde{\mathbf{x}} = \tilde{\mathbf{b}},\quad (3.53)$$

where  $\tilde{\mathbf{A}} = \mathbf{R}(\mathbf{A}\mathbf{C})$ ,  $\tilde{\mathbf{x}} = \mathbf{C}^{-1}\mathbf{x}$  and  $\tilde{\mathbf{b}} = \mathbf{R}\mathbf{b}$ . The matrix  $\mathbf{C}$  scales the columns of the matrix with the mass of the corresponding species:

$$\mathbf{C} = \text{diag}(m_i/m_p), \quad (3.54)$$

where  $m_p$  is the proton mass. The matrix  $\mathbf{R}$  scales the rows such that every diagonal element of the modified matrix  $\tilde{\mathbf{A}}$  will be unity:

$$\mathbf{R} = \text{diag}(1/(AC)_{ii}). \quad (3.55)$$

After the solution of the modified system has been obtained, the modified solution  $\tilde{\mathbf{x}}$  is transformed back to the original solution vector  $\mathbf{x}$ . In simulations of mixtures with electrons, the preconditioning step typically reduces the condition number from  $10^{21}$  to  $10^6$ .

### 3.6 Concluding remarks

In this chapter we explained how the equations as presented in Chapter 2 are discretized and solved. However, nothing was said about the implementation of the presented numerical strategies. We will not go into much detail, but to conclude this chapter we will give a small example on the implementation of discretization in Plasimo.

A key infrastructural component of Plasimo is the LinSys class template library. LinSys provides support in C++ for tensor values, tensor fields and systems of equations involving such fields. In addition, LinSys facilitates the discretization of (coupled) field equations. Discretization of the coupled system of equations for the mass fractions, for example, is done with the following C++ code:

```
//loop over all species
for (unsigned i=0; i!=num_part; ++i)
{
    (
        //the surface integral of the flux
        surf_int(cd_flux(y,conv,diff,i))
        -
        //the volume integral of the sources
        (nonlin(C(i)) + lin(y_i) * P(i)) * volume()
    ).apply_foreach_internal(y_i); //for all control volumes
}
```

As can be seen, this code closely resembles equation (3.18). In general, discretization can be achieved with LinSys by composing expressions that consist of a number of discretizer primitives such as `surf_int`, which provides the surface integral of a flux. In addition to the usual arithmetic and vectorial operators (divergence, gradient and curl), LinSys provides discretizers for convection-diffusion fluxes. Various schemes are offered, in the above example `cd_flux` gives the expression for the flux in the coupled exponential scheme.

## Chapter 4

# Multicomponent diffusion in neutral mixtures

This chapter is based on:

*Mass conservative finite volume discretization of the continuity equations in multi-component mixtures*, Peerenboom, K.S.C., Dijk, J. van, Ten Thije Boonkkamp, J.H.M., Liu, L., Goedheer, W.J., Mullen, J.J.A.M. van der, *Journal of Computational Physics*, 230(9), 3525-3537, 2011

**Abstract.** The Stefan-Maxwell equations for multi-component diffusion result in a system of coupled continuity equations for all species in the mixture. We use a generalization of the exponential scheme to discretize this system of continuity equations with the finite volume method. The system of continuity equations in this work is obtained from a non-singular formulation of the Stefan-Maxwell equations, where the mass constraint is not applied explicitly. Instead, all mass fractions are treated as independent unknowns and the constraint is a result of the continuity equations, the boundary conditions, the diffusion algorithm and the *discretization scheme*. We prove that with the generalized exponential scheme from Chapter 3, the mass constraint can be satisfied exactly, although it is not explicitly applied. A test model from literature is used to verify the correct behavior of the scheme.

## 4.1 Introduction

In numerical simulations of multi-component mixtures, the diffusion model is one of the key aspects of the calculation. In plasmas in local thermodynamic equilibrium (LTE), where both the internal and reactive processes are at equilibrium, the diffusion model is used to account for the effects of elemental demixing or to calculate the reactive contribution to the thermal conductivity [28, 29, 30]. In combustion simulations and simulations of plasmas that are not in local thermodynamic equilibrium (NLTE), the diffusive flux is needed in the species continuity equations.

Because of its simplicity, the Fick diffusion model [31, 32] is often used. However, the validity of this diffusion model is restricted to cases of binary and dilute mixtures. In the more general case, when the Stefan-Maxwell relations [33, 19] are used, the diffusive flux of a species depends not only on its own concentration gradient but also on the concentration gradients of other species.

Consequently, in contrast to the Fick diffusion model, the Stefan-Maxwell model results in a *coupled* set of continuity equations for all species, in which the diffusive fluxes are described by matrices rather than scalar coefficients. Recent work on the discretization of these equations has focused on the finite difference [34] and the finite element methods [35]. So far, little attention has been paid to the finite-volume discretization. This is most likely because the usual (scalar) finite volume discretization schemes [22, 23] are not directly applicable when the diffusive fluxes are coupled. Pope and Gogos [36] addressed the discretization issue by artificially decoupling the governing equations. Only the self-diffusion operator was treated implicitly, while the diffusion in the other species was treated explicitly as a convection term. As a consequence, this method fits nicely in the traditional (scalar) finite volume schemes as presented in [22, 23]. However, as shown in [37], ‘segregated solution of the governing equations, wherein only the self-diffusion operator is treated implicitly, while the diffusion due to the other species is treated explicitly, results in an iterative algorithm whose convergence depends on the strategy used to conserve overall mass’. Furthermore, according to [37], ‘for multi-dimensional problems, convergence is not guaranteed even with severe under-relaxation, and is dependent on the mesh size’. In [37], Mazumder proposes a fully implicit approach, which is, however, only suitable for simulations without convection.

Another issue in the implementation of the Stefan-Maxwell equations is the application of the mass constraint  $\sum_i y_i = 1$  for the mass fractions  $y_i$ . A straightforward approach is to single out one species and calculate the mass fraction of this species from the mass constraint instead of from the continuity equation. However, this approach can give cancellation problems when the selected species is not present in excess everywhere in the plasma and can even lead to negative mass fractions. For these reasons, an approach where all species are treated as independent unknowns and the constraint is not explicitly applied is preferred. Such an approach is, e.g., described by Giovangigli [38] and Magin and Degrez [15]. Although the mathematical background is extensively studied in those papers, no attention is paid to the effect

of the discretization scheme on mass conservation. This issue is addressed in [34] for diagonally implicit integration with the finite difference method, and it is shown there that this method does not guarantee that the mass constraint will be satisfied.

In this chapter, we apply the generalization of the exponential discretization scheme as introduced in Chapter 3 to the fluxes obtained from the Stefan-Maxwell equations. The coupling between the fluxes is taken into account, while staying as close as possible to the formulation of the traditional finite volume schemes. To our knowledge, this is the first time a coupled finite volume scheme is applied to the Stefan-Maxwell diffusive fluxes.

Regarding the mass constraint we will follow the formulation of the Stefan-Maxwell equations as described in [38, 15], but extend the idea to the discrete level and make the connection with the discretization scheme. We will prove that with the proposed coupled exponential scheme, the mass constraint can be satisfied exactly<sup>1</sup>.

The structure of this chapter is as follows. Section 4.2 shortly summarizes the equations involved. In Section 4.3, we explain how the flux diffusion matrix can be obtained from the Stefan-Maxwell equations. Then, in Section 4.4 it is shown that for a dominant background gas the complex formalism of multicomponent diffusion reduces to the simple Fick law. Section 4.5 discusses the discrete mass conservation, while test results are given in Section 4.6. This chapter ends with a short discussion in Section 4.7.

## 4.2 Governing equations

### 4.2.1 Continuity equations and constraints

The composition of a multi-component mixture can be described by the continuity equations for the different species. Expressed in terms of the species mass fraction  $y_i$ , the continuity equation for species  $i$  reads:

$$\frac{\partial}{\partial t} (\rho y_i) + \nabla \cdot (\rho \vec{v} y_i) + \nabla \cdot (\rho \vec{v}_i y_i) = m_i \omega_i, \quad (4.1)$$

where  $\rho$  is the mass density,  $\vec{v}$  the mass averaged velocity of the plasma,  $\vec{v}_i$  the diffusion velocity and  $m_i \omega_i$  the mass production rate per unit of volume. The diffusion velocities can be obtained from the Stefan-Maxwell equations, which will be presented in Section 4.2.2. As discussed in Section 2.1, the diffusion velocity  $\vec{v}_i$  is defined as the velocity of species  $i$  with respect to the mass averaged velocity  $\vec{v}$ . As a result of this definition, no net mass is transported by the sum of the diffusive fluxes:

$$\sum_i y_i \vec{v}_i = \vec{0}. \quad (4.2)$$

---

<sup>1</sup>Throughout this thesis, the term ‘exact’ means ‘up to the order of the machine accuracy’.

Since the mass fractions are defined as the ratio between the species mass density  $\rho_i$  and the total mass density,  $y_i = \rho_i/\rho$ , the mass fractions are constrained as well:

$$\sum_i y_i = 1. \quad (4.3)$$

Since no net mass is produced in reactions, the sum of the mass production rates satisfies the relation:

$$\sum_i m_i \omega_i = 0. \quad (4.4)$$

It is important to note that, analytically, constraint (4.4) is automatically satisfied since no net mass is created or destroyed in reactions, while constraints (4.2) and (4.3) need to be imposed. Section 4.3.2 discusses how these constraints can be imposed in a symmetric way, such that all species are treated as independent unknowns.

#### 4.2.2 Stefan-Maxwell equations

The diffusion velocities  $\vec{v}_i$  are described by the Stefan-Maxwell equations, which can be deduced from the kinetic theory of gases [33, 19]. Alternatively, the Stefan-Maxwell equations can be obtained from momentum conservation considerations [39]. The derivation in [39] corresponds to the first order Sonine polynomial expansion [40] of the exact kinetic theory of gases. In this case the Stefan-Maxwell equations are given by:

$$\sum_j F_{ij} \vec{v}_j = -\vec{d}_i \quad \Leftrightarrow \quad \mathbf{F} \mathbf{v} = -\mathbf{d}, \quad (4.5)$$

where  $\mathbf{F} = (F_{ij})$  is the friction matrix,  $\mathbf{v} = (\vec{v}_i)$  is the vector of diffusion velocities and  $\mathbf{d} = (\vec{d}_i)$  is the driving force for species  $i$ . Alternatively, the formulation from the kinetic theory of gases can be used. This results in the equations:

$$\vec{v}_i = -\sum_j D_{ij} \vec{d}_j \quad \Leftrightarrow \quad \mathbf{v} = -\mathbf{D} \mathbf{d}, \quad (4.6)$$

with  $\mathbf{D} = (D_{ij})$ , the multicomponent diffusion coefficient matrix. To keep the following discussion as simple as possible, we will take into account only ordinary concentration diffusion as a driving force, in which case:

$$\vec{d}_i = \nabla x_i, \quad (4.7)$$

with  $x_i$  the mole fraction of species  $i$ .

An important difference between the two formulations (4.5) and (4.6) is that the elements of the (first order) friction matrix are explicitly known, while the elements of the multicomponent diffusion coefficient matrix are not. The elements of the friction matrix are given by:

$$F_{ij} = \begin{cases} \sum_k f_{ik} & \text{if } i = j, \\ -f_{ij} & \text{if } i \neq j, \end{cases} \quad (4.8)$$

with  $f_{ij}$  the mutual friction coefficient between species  $i$  and  $j$ , which can be expressed as:

$$f_{ij} = \frac{x_i x_j}{\mathcal{D}_{ij}}, \quad f_{ii} \equiv 0, \quad (4.9)$$

with  $x_i$  the mole fraction of species  $i$  and  $\mathcal{D}_{ij}$  the usual binary diffusion coefficient [33, 19]. The friction coefficients are symmetric:  $f_{ij} = f_{ji}$ , and positive for  $i \neq j$ :  $f_{ij} > 0$ . Note that these friction coefficients are only valid for first order diffusion velocities. In more accurate Stefan-Maxwell equations, the friction coefficients are not explicitly known. In this case the Stefan-Maxwell equations result from block elimination of larger systems and then the coefficients  $\mathcal{D}_{ij}$  are no longer the binary diffusion coefficients [16].

If we take a closer look at the mathematical properties of the two diffusion formulations, we can see that  $\mathbf{F}$  is singular, the nullspace<sup>2</sup> of  $\mathbf{F}$  is spanned by the vector  $\mathbf{u} = (1, \dots, 1)^T$ . The range of  $\mathbf{F}$  is given by the orthoplement  $\mathbf{u}^\perp$ . Any solution  $\mathbf{v}$  of the Stefan-Maxwell equations can be split in two components:  $\mathbf{v} = \mathbf{v}_{\mathbf{u}^\perp} + \mathbf{v}_{\mathbf{u}}$ , with  $\mathbf{v}_{\mathbf{u}^\perp} \in \mathbf{u}^\perp$  and  $\mathbf{v}_{\mathbf{u}} \in \mathbf{u}$ . The solutions given by the Stefan-Maxwell system are not unique since  $\mathbf{v}$  is a solution if  $\mathbf{F}\mathbf{v}_{\mathbf{u}^\perp} = -\mathbf{d}$  regardless of  $\mathbf{v}_{\mathbf{u}}$ . Physically, this is because one may add a constant velocity to all diffusion velocities, since these are relative. Likewise, the nullspace of  $\mathbf{D}$  is  $\mathbf{y} = (y_1, \dots, y_N)^T$  and the range  $\mathbf{y}^\perp$ . Or, in other words, one may add any multiple of the mass fractions to the driving forces and still have a valid solution. The properties of  $\mathbf{F}$  and  $\mathbf{D}$  are summarized in Table 4.1.

	Stefan-Maxwell	Kinetic theory
system	$\mathbf{F}\mathbf{v} = -\mathbf{d}$	$\mathbf{D}\mathbf{d} = -\mathbf{v}$
nullspace	$N(\mathbf{F}) = \mathbf{u}$	$N(\mathbf{D}) = \mathbf{y}$
range	$R(\mathbf{F}) = \mathbf{u}^\perp$	$R(\mathbf{D}) = \mathbf{y}^\perp$
constraint	$\langle \mathbf{y}, \mathbf{v} \rangle = 0$	$\langle \mathbf{u}, \mathbf{d} \rangle = 0$
regularization	$\tilde{\mathbf{F}} = \mathbf{F} + \alpha \mathbf{y} \otimes \mathbf{y}$	$\tilde{\mathbf{D}} = \mathbf{D} + \beta \mathbf{u} \otimes \mathbf{u}$
regularized system	$\tilde{\mathbf{F}}\mathbf{v} = -\mathbf{d}$	$\tilde{\mathbf{D}}\mathbf{d} = -\mathbf{v}$

**Table 4.1:** Properties of the two diffusion formulations. The matrices  $\mathbf{F}$  and  $\mathbf{D}$  are each others generalized inverses with prescribed range and nullspace.

The two diffusion formulations seem each others inverse. The matrices  $\mathbf{F}$  and  $\mathbf{D}$ , however, are both singular and do not have an inverse. Instead, they are each others generalized inverses<sup>3</sup> with prescribed range and nullspace [41]. The following properties hold:

$$\mathbf{F}\mathbf{D}\mathbf{F} = \mathbf{F}, \quad \mathbf{D}\mathbf{F}\mathbf{D} = \mathbf{D},$$

<sup>2</sup>The nullspace of a matrix  $\mathbf{A}$  is the set of all vectors  $\mathbf{x}$  for which  $\mathbf{A}\mathbf{x} = \mathbf{0}$ .

<sup>3</sup>See appendix A for a more thorough discussion on generalized inverses in relation to constrained systems.



$$\mathbf{F}\mathbf{D} = \mathbf{I} - \frac{\mathbf{y} \otimes \mathbf{u}}{\langle \mathbf{u}, \mathbf{y} \rangle}, \quad \mathbf{D}\mathbf{F} = \mathbf{I} - \frac{\mathbf{u} \otimes \mathbf{y}}{\langle \mathbf{u}, \mathbf{y} \rangle},$$

with  $\otimes$  denoting the dyadic product:  $\mathbf{a} \otimes \mathbf{b} = (a_i b_j)$ . To obtain suitable expressions for the diffusion velocities the matrices  $\mathbf{D}$  and  $\mathbf{F}$  need to be regularized. The next section will discuss how this is done.

### 4.3 The flux diffusion matrix

To solve for the species mass fractions, an expression for the diffusive mass fluxes in terms of the gradients of the mass fractions is needed. However, we have an expression for the species diffusion velocities in terms of the gradients of the mole fractions, given by (4.6). The diffusion velocities, therefore, need to be converted to mass fluxes. An additional conversion is needed to obtain the gradients of the mass fractions from the gradients of the mole fractions. Furthermore, the matrix  $\mathbf{D}$  needs to be regularized.

We seek an expression of the form:

$$\frac{\partial}{\partial t}(\rho y_i) + \nabla \cdot (\rho \vec{v} y_i) - \nabla \cdot \left( \sum_j \Gamma_{ij} \nabla y_j \right) = m_i \omega_i, \quad (4.10)$$

where the coefficients  $\Gamma_{ij}$  denote the elements of the *flux diffusion matrix*  $\mathbf{\Gamma}$ , which expresses the diffusive mass fluxes in terms of the gradients of the mass fractions. The matrix  $\mathbf{\Gamma}$  is in fact the product of three matrices:

$$\mathbf{\Gamma} = \mathbf{R}\tilde{\mathbf{D}}\tilde{\mathbf{M}}. \quad (4.11)$$

The matrices are:

1. A matrix  $\tilde{\mathbf{M}}$ , relating the gradients of the mole fractions to the gradients of the mass fractions. The driving forces  $\vec{d}_i$  are given in terms of the gradients of the mole fractions  $\nabla x_i$ . Since equation (4.10) is solved for the mass fractions, the gradients of the mole fractions  $\nabla x_i$  need to be converted to the gradients of the mass fractions  $\nabla y_i$ . This conversion is discussed in Section 4.3.1.
2. A matrix  $\tilde{\mathbf{D}}$ , relating the diffusion velocities to the gradients of the mole fractions. The coefficients of  $\mathbf{F}$  are explicitly known, while the elements of  $\mathbf{D}$  are not. However, to substitute (4.6) in (4.1) we need the formulation where the diffusion velocities are given in terms of the driving forces. Therefore, we have to calculate the multicomponent diffusion matrix  $\mathbf{D}$  from the friction matrix  $\mathbf{F}$ . Also, matrix  $\mathbf{D}$  has to be regularized to obtain  $\tilde{\mathbf{D}}$ . Since calculation and regularization of  $\mathbf{D}$  are intertwined, both are discussed in Section 4.3.2.
3. A matrix  $\mathbf{R}$ , relating the diffusive mass fluxes to the diffusion velocities. The calculation of  $\mathbf{R}$  is discussed in Section 4.3.3.

To be able to find a numerical solution of the system of mass balances (4.10), it is crucial that the flux diffusion matrix is non-singular. Therefore, the matrices  $\tilde{\mathbf{M}}$ ,  $\tilde{\mathbf{D}}$  and  $\mathbf{R}$  must also be non-singular. Due to the mass and mass flux constraint, calculation of these matrices is not trivial, since care has to be taken to avoid that mass constraints are imposed a priori.

The continuity equations (4.1) are constrained by (4.3), while the Stefan-Maxwell equations (4.5) are subject to constraint (4.2). As a result, there are  $N - 1$  independent continuity equations and  $N - 1$  independent Stefan-Maxwell equations in a system with  $N$  different species. Therefore, it is possible to single out one species and calculate the mass fraction of this species from (4.3). However, this approach is asymmetric, since one species is treated differently from the other species. Furthermore, this approach can give cancellation problems when the selected species is not present in excess everywhere in the plasma.

For the above mentioned reasons, we follow the strategy of [38], where all mass fractions are considered as independent unknowns and the constraints are not imposed explicitly. Then, since all  $N$  species mass fractions are treated as independent unknowns, the constraints must be a *result* of the continuity equations, the boundary conditions, the initial conditions and the diffusion algorithm. We will show that the formulation of [38] leads to an elliptic equation for  $\sigma^m = \sum_i y_i$ . The idea then is that when  $\sigma^m = 1$  is satisfied at the boundary,  $\sigma^m = 1$  will be satisfied in the entire domain, because of the elliptic nature of the equation. In addition, for time-dependent problems,  $\sigma^m = 1$  will be satisfied for all  $t > 0$ , when  $\sigma^m = 1$  holds for the initial condition. In this strategy, special attention has to be paid to the application of the constraints, since any *a priori* application of (4.3) or (4.2) gives rise to a singular flux diffusion matrix  $\mathbf{\Gamma}$ , as will be shown in the following sections.

#### 4.3.1 Calculation of $\tilde{\mathbf{M}}$

Since the continuity equations are solved for the mass fractions  $y_i$  of the species, the driving forces of the Stefan-Maxwell equations need to be expressed in terms of the mass fractions as well. The relation between the mole and mass fractions is given by:

$$x_i = \frac{m}{m_i} y_i, \quad (4.12)$$

where  $m_i$  is the mass of species  $i$  and the mixture averaged mass  $m$  is defined as:

$$1/m = \sum_j y_j / m_j. \quad (4.13)$$

Note that  $m = \rho/n$ , with  $n$  the total number density of the mixture. By taking the gradient of expression (4.12) the gradients of the mole and mass fractions can be related as:

$$\partial_x \mathbf{x} = \mathbf{M} \partial_x \mathbf{y}, \quad (4.14)$$

where

$$\mathbf{M} = \text{diag}(\mathbf{x}) (\mathbf{I} - \mathbf{u} \otimes \mathbf{x}) \text{diag}^{-1}(\mathbf{y}), \quad (4.15)$$

with  $\mathbf{x}$  the vector of mole fractions of all the species. The left nullspace of  $\mathbf{M}$  is given by  $\mathbf{u}$ . As a result, the matrix  $\mathbf{M}$  and the flux diffusion matrix  $\mathbf{\Gamma}$  are singular, as shown in [38].

To eliminate the singularity of  $\mathbf{M}$ , we adopt the relation between the mass and mole fractions as proposed in [38]:

$$x_i = \sigma^m \frac{m}{m_i} y_i, \quad (4.16)$$

where  $\sigma^m = \sum_i y_i$ . Note that  $\sum_i x_i = \sum_i y_i$  follows from (4.16). The gradient of (4.16) is now given by:

$$\partial_x \mathbf{x} = \tilde{\mathbf{M}} \partial_x \mathbf{y}, \quad (4.17)$$

with

$$\tilde{\mathbf{M}} = \left( \text{diag}(\mathbf{x}) + \frac{\mathbf{x} \otimes (\mathbf{y} - \mathbf{x})}{\langle \mathbf{x}, \mathbf{u} \rangle} \right) \text{diag}^{-1}(\mathbf{y}). \quad (4.18)$$

For later reference, note that

$$\mathbf{u}^T \tilde{\mathbf{M}} = \mathbf{u}^T, \quad (4.19)$$

which will be used in Section 4.5. The modified matrix  $\tilde{\mathbf{M}}$  is non-singular and summation of (4.17) yields  $\sum_i \nabla x_i = \sum_i \nabla y_i$ . The Stefan-Maxwell equations can now be expressed in terms of the gradients of the mass fractions.

#### 4.3.2 Calculation of $\tilde{\mathbf{D}}$

With the result from the last section, we can rewrite the gradients of the mole fractions to the gradients of the mass fractions to express the diffusion velocities as:

$$\vec{v}_i = - \sum_j D_{ij} \sum_k \tilde{M}_{jk} \nabla y_k. \quad (4.20)$$

It would now seem straightforward to substitute this result in (4.1) and solve for the mass fractions. However, the elements of  $\mathbf{D}$  are not explicitly known and therefore need to be calculated by inversion of  $\mathbf{F}$ . Since  $\mathbf{F}$  has nullspace  $\mathbf{u}$ , and is therefore non-invertible,  $\mathbf{F}$  has to be regularized.

Another problem is that  $\mathbf{y}$  is in the nullspace of  $\mathbf{D}$  and therefore  $\sum_i y_i \vec{v}_i = \vec{0}$  is satisfied independent of the diffusion driving forces. That this is a problem can be made comprehensible by considering the sum of all  $N$  species continuity equations in steady state [38]:

$$\sum_i \left( \nabla \cdot (\rho \vec{v}_i y_i) + \nabla \cdot (\rho \vec{v}_i y_i) \right) = \sum_i m_i \omega_i. \quad (4.21)$$

Since only  $y_i$  and  $\vec{v}_i$  are dependent on  $i$  and chemical reactions do not lead to net mass production, this sum reduces to:

$$\nabla \cdot (\rho \vec{v} \sigma^m) = 0. \quad (4.22)$$

This equation can be seen as the continuity equation for the ‘species’  $\sigma^m = \sum_i y_i$ . It can be seen that (4.22) degenerates for  $\vec{v} = \vec{0}$ , due to missing diffusion terms for  $\sigma^m$ . As is shown in [38], singularities will appear for flux boundary conditions as well. The degeneracy of (4.22) is a problem because (4.3) is not applied explicitly and  $\sigma^m = 1$  should result from the formulation of the continuity equations.

To solve the above mentioned problems associated with the singularities in  $\mathbf{F}$  and  $\mathbf{D}$  we have to calculate regularized matrices  $\tilde{\mathbf{F}}$  and  $\tilde{\mathbf{D}}$ . As for the matrix  $\mathbf{M}$  from the previous section, the singularities in  $\mathbf{F}$  and  $\mathbf{D}$  are due to the fact that mass constraints are imposed a priori [38]. The regularization of  $\mathbf{F}$  should preserve the symmetry and should not change the solution of the problem. This can be established by introducing:

$$\tilde{\mathbf{F}} = \mathbf{F} + \alpha \mathbf{y} \otimes \mathbf{y}, \quad (4.23)$$

where  $\alpha$  is a free, positive parameter. The matrix  $\alpha \mathbf{y} \otimes \mathbf{y}$  projects the diffusion velocities on the mass flux constraint <sup>4</sup>. Likewise,  $\mathbf{D}$  can be regularized by:

$$\tilde{\mathbf{D}} = \mathbf{D} + \beta \mathbf{u} \otimes \mathbf{u}, \quad (4.24)$$

where  $\beta$  is a free, positive parameter. When  $\alpha$  and  $\beta$  satisfy  $\alpha\beta(\sigma^m)^2 = 1$ , it can be verified that  $\tilde{\mathbf{F}}\tilde{\mathbf{D}} = \mathbf{I}$ . Now  $\tilde{\mathbf{D}}$  and  $\tilde{\mathbf{F}}$  are true inverses of each other,  $\tilde{\mathbf{D}}$  can be calculated as  $\tilde{\mathbf{F}}^{-1}$  and the velocities can be expressed as:

$$\vec{v}_i = - \sum_j \tilde{D}_{ij} \sum_k \tilde{M}_{jk} \nabla y_k. \quad (4.25)$$

It can be seen that with this new expression (4.2) is no longer satisfied independent of the driving forces. Substitution of the new expression (4.25) in (4.1) and summation over all species now gives:

$$\nabla \cdot (\rho \vec{v} \sigma^m) - \nabla \cdot (\mathcal{D}^m \nabla \sigma^m) = 0, \quad (4.26)$$

with  $\mathcal{D}^m = \rho\beta\sigma^m = \frac{\rho}{\alpha\sigma^m}$ . The equation obtained is an elliptic convection-diffusion equation for  $\sigma^m$ . Under appropriate boundary conditions, the physical solution  $\sigma^m = 1$  will be obtained in the entire domain [42, 43].

In order to invert  $\tilde{\mathbf{F}}$ ,  $\alpha$  has to be chosen appropriately. An appropriate choice for the free parameter  $\alpha$  is  $\alpha = 1/\max(\mathcal{D}_{ij})$  [15], since it guarantees that the elements of the matrices  $\mathbf{F}$  and  $\alpha \mathbf{y} \otimes \mathbf{y}$  have the same order of magnitude. Note that instead of direct inversion of the Stefan-Maxwell system, it is possible to use iterative methods as discussed for example in [44] to obtain  $\tilde{\mathbf{D}}$ . These iterative methods are computationally cheaper than direct inversion. We will not discuss this method here, since in our case the largest computational expense lies in solving the discretized species mass balances, and not in the inversion of the Stefan-Maxwell system at each grid point.

<sup>4</sup>See appendix A.2 for a discussion on projectors.

### 4.3.3 Calculation of $\mathbf{R}$

The final step in obtaining the flux diffusion matrix  $\mathbf{\Gamma}$  is to convert the diffusion velocities to the mass fluxes  $\vec{J}_i$ :

$$\vec{J}_i = \rho y_i \vec{v}_i = -\rho y_i \sum_j \tilde{D}_{ij} \sum_k \tilde{M}_{jk} \nabla y_k. \quad (4.27)$$

Recalling the definition of the flux diffusion matrix in equation (4.11) it is clear that

$$\mathbf{R} = \text{diag}(\rho y_i). \quad (4.28)$$

The diffusive mass fluxes can thus be expressed as:

$$\vec{J}_i = - \sum_j \Gamma_{ij} \nabla y_j. \quad (4.29)$$

For positive mass fractions,  $\mathbf{R}$ ,  $\tilde{\mathbf{D}}$  and  $\tilde{\mathbf{M}}$  are non-singular and  $\mathbf{R}$  and  $\tilde{\mathbf{D}}$  are even symmetric positive definite. It can be proven [27] that  $\mathbf{\Gamma}$  is positive definite and has a complete set of eigenvectors, which is a property we need for the discretization scheme. We have now found the appropriate expression for the flux diffusion matrix.

## 4.4 Analytical examples

In binary and dilute mixtures the complicated multicomponent diffusion formalism should reduce to Fick's law, where diffusion can be described by a coefficient instead of a matrix. These two limiting cases will be considered here.

**Binary mixture** To investigate the limit of a binary mixture, consider a gas with two neutral species: ( $x_1 = x$ ,  $x_2 = 1 - x$ ) In this case there is only one relevant friction coefficient  $f = f_{12} = f_{21} = x_1 x_2 / D_{12}$ , and (4.8) reduces to:

$$\mathbf{F} = \begin{pmatrix} f & -f \\ -f & f \end{pmatrix}.$$

The inverse of the friction matrix is given by:

$$\begin{aligned} (\mathbf{F} + \alpha \mathbf{y} \otimes \mathbf{y})^{-1} &= \begin{pmatrix} f + \alpha y_1 y_1 & -f + \alpha y_1 y_2 \\ -f + \alpha y_2 y_1 & f + \alpha y_2 y_2 \end{pmatrix}^{-1}, \\ &= \frac{1}{\alpha f} \begin{pmatrix} f + \alpha y_2 y_2 & f - \alpha y_1 y_2 \\ f - \alpha y_2 y_1 & f + \alpha y_1 y_1 \end{pmatrix}, \\ &= \frac{1}{f} \begin{pmatrix} y_2 y_2 & -y_1 y_2 \\ -y_2 y_1 & y_1 y_1 \end{pmatrix} + \frac{1}{\alpha} \begin{pmatrix} 1 & 1 \\ 1 & 1 \end{pmatrix}. \end{aligned}$$

The diffusion coefficient matrix is given by:

$$\begin{aligned}\mathbf{D} &= (\mathbf{F} + \alpha \mathbf{y} \otimes \mathbf{y})^{-1} - \frac{1}{\alpha} \mathbf{u} \otimes \mathbf{u}, \\ &= \frac{1}{f} \begin{pmatrix} y_2 y_2 & -y_1 y_2 \\ -y_2 y_1 & y_1 y_1 \end{pmatrix}.\end{aligned}$$

The result is independent of the regularization parameter  $\alpha$ , as should it should: the regularization procedure should not influence the final result. Calculation of the mass fluxes gives:

$$\begin{aligned}\mathbf{J} &= -\mathbf{R}\mathbf{D}\partial\mathbf{x}, \\ &= -\frac{\rho y_1 y_2}{f} \partial\mathbf{x},\end{aligned}$$

where  $\partial\mathbf{x} = (\nabla x, -\nabla x)^T$ . From this result we can see that diffusion does not lead to net mass transport:  $\vec{J}_1 + \vec{J}_2 = 0$ . Furthermore, the diffusion coefficient matrix reduces to a single diffusion coefficient.

**Dilute mixture** To investigate a dilute mixture with a dominant background gas, a mixture with three species is considered. The first species is the dominant species, while species two and three are the traces:  $y_1 \approx 1$ ,  $y_2 \approx 0$ ,  $y_3 \approx 0$ . We can then neglect the friction between species two and three ( $f_{23} = 0$ ), and the friction matrix is given by:

$$\tilde{\mathbf{F}} = \begin{pmatrix} (f_{12} + f_{13}) + \alpha y_1 y_1 & -f_{12} + \alpha y_1 y_2 & -f_{13} + \alpha y_1 y_3 \\ -f_{12} + \alpha y_1 y_2 & f_{12} + \alpha y_2 y_2 & +\alpha y_2 y_3 \\ -f_{13} + \alpha y_1 y_3 & +\alpha y_2 y_3 & f_{13} + \alpha y_3 y_3 \end{pmatrix}.$$

Inversion gives:

$$\begin{aligned}\mathbf{D} &= \tilde{\mathbf{F}}^{-1} - \frac{1}{\alpha} \mathbf{u} \otimes \mathbf{u} \\ &= \begin{pmatrix} \frac{y_2^2}{f_{12}} + \frac{y_3^2}{f_{13}} & -\frac{y_2(y_1+y_3)}{f_{12}} + \frac{y_3^2}{f_{13}} & -\frac{y_3(y_1+y_2)}{f_{13}} + \frac{y_2^2}{f_{12}} \\ -\frac{y_2(y_1+y_3)}{f_{12}} + \frac{y_3^2}{f_{13}} & \frac{(y_1+y_3)^2}{f_{12}} + \frac{y_3^2}{f_{13}} & -\frac{y_3(y_1+y_2)}{f_{13}} - \frac{y_2(y_1+y_3)}{f_{12}} \\ -\frac{y_3(y_1+y_2)}{f_{13}} + \frac{y_2^2}{f_{12}} & -\frac{y_3(y_1+y_2)}{f_{13}} - \frac{y_2(y_1+y_3)}{f_{12}} & \frac{(y_1+y_2)^2}{f_{13}} + \frac{y_2^2}{f_{12}} \end{pmatrix}.\end{aligned}$$

Calculation of the mass fluxes and neglect of quadratic terms in  $y_2$  and  $y_3$  gives:

$$\begin{aligned}\mathbf{J} &= -\mathbf{R}\mathbf{D}\partial\mathbf{x}, \\ &= -\rho \begin{pmatrix} 0 & -\frac{y_2 y_1^2}{f_{12}} & -\frac{y_3 y_1^2}{f_{13}} \\ 0 & \frac{y_1^2 y_2}{f_{12}} & 0 \\ 0 & 0 & \frac{y_1^2 y_3}{f_{13}} \end{pmatrix} \partial\mathbf{x}.\end{aligned}$$

Again, we can see that the mass flux constraint is satisfied:  $\vec{J}_1 + \vec{J}_2 + \vec{J}_3 = 0$ . Furthermore, the diffusion in the trace species is described by a single coefficient, as should be the case in the limit of Fickian diffusion.

#### 4.5 Discrete mass conservation

In Section 4.3.2 we have shown that *analytically*,  $\sigma^m = 1$  will be satisfied in the entire domain due to the elliptic nature of (4.26). In this section we will show that when the coupled exponential scheme from Chapter 3 is used for discretization, this is true *numerically* as well. As will be derived, in this case the discrete equation for  $\sigma^m$  reads:

$$a_C \sigma_C^m = a_E \sigma_E^m + a_W \sigma_W^m, \quad (4.30)$$

with  $\sigma_C^m$ ,  $\sigma_E^m$  and  $\sigma_W^m$  the values of  $\sigma^m$  on the central, east and west nodal point, respectively. The coefficients  $a_C$ ,  $a_E$  and  $a_W$  are the corresponding discretization coefficients and satisfy  $a_E > 0$ ,  $a_W > 0$  and  $a_C = a_E + a_W$ . The discrete equation for  $\sigma^m$  reveals a very pleasant property of the coupled exponential scheme that we introduced in Chapter 3. Since  $\sigma_C^m$  is a weighted average of  $\sigma_E^m$  and  $\sigma_W^m$ , we can deduce from the discrete maximum principle that  $\sigma^m = 1$  will be satisfied in the entire domain. Suppose that  $\sigma_C^m$  is a local maximum:  $\sigma_C^m \geq \sigma_E^m$ ,  $\sigma_C^m \geq \sigma_W^m$ . However, since  $\sigma_C^m$  is a weighted average the following needs to be true:  $\sigma_C^m = \sigma_E^m = \sigma_W^m$ . We can now take  $\sigma_E^m$  or  $\sigma_W^m$  and continue the procedure until we hit the boundary, where  $\sigma^m = 1$ . Although the mass fractions of the individual species may be affected by discretization errors, we are guaranteed to have a mass conserving solution for  $\sigma^m$  where all the points in the domain satisfy  $\sigma^m = 1$ , *without discretization error*.

To derive this discrete equation for  $\sigma^m$ , we start with the discretized equation for the mass fraction vector  $\mathbf{y}$ . When we apply the coupled exponential scheme from Chapter 3 to equation (4.10), the following expression is obtained:

$$\mathbf{A}_C \mathbf{y}_C = \mathbf{A}_E \mathbf{y}_E + \mathbf{A}_W \mathbf{y}_W + \mathbf{s}_C \Delta x. \quad (4.31)$$

Left multiplication with  $\mathbf{u}^T = (1, \dots, 1)$  gives:

$$\mathbf{u}^T \mathbf{A}_C \mathbf{y}_C = \mathbf{u}^T \mathbf{A}_E \mathbf{y}_E + \mathbf{u}^T \mathbf{A}_W \mathbf{y}_W, \quad (4.32)$$

since  $\mathbf{u}^T \mathbf{s}_C = 0$  by virtue of equation (4.4). If  $\mathbf{u}^T$  is a left eigenvector of the discretization matrices this can be written as:

$$a_C^m \mathbf{u}^T \mathbf{y}_C = a_E^m \mathbf{u}^T \mathbf{y}_E + a_W^m \mathbf{u}^T \mathbf{y}_W, \quad (4.33)$$

which is equivalent to:

$$a_C^m \sigma_C^m = a_E^m \sigma_E^m + a_W^m \sigma_W^m. \quad (4.34)$$

In the following subsections, we will prove that  $\mathbf{u}^T$  is indeed a left eigenvector of all the discretization matrices. The proof consists of three parts:

1.  $\mathbf{u}^T$  is a left eigenvector of the flux diffusion matrix,
2.  $\mathbf{u}^T$  is a left eigenvector of the Péclet matrices ,
3.  $\mathbf{u}^T$  is a left eigenvector of the discretization matrices.

**Eigenvector of the flux diffusion matrix**

The matrix vector product of  $\mathbf{u}^T$  and  $\mathbf{\Gamma}$  can be written as:

$$\mathbf{u}^T \mathbf{\Gamma} = \mathbf{u}^T \mathbf{R} \tilde{\mathbf{D}} \tilde{\mathbf{M}}. \quad (4.35)$$

Since  $\mathbf{u}^T \mathbf{R} = \rho \mathbf{y}^T$  by the definition in equation (4.28), this can be written as:

$$\mathbf{u}^T \mathbf{\Gamma} = \rho \mathbf{y}^T \tilde{\mathbf{D}} \tilde{\mathbf{M}}. \quad (4.36)$$

Using the definition of  $\tilde{\mathbf{D}}$  in equation (4.24) we arrive at

$$\mathbf{u}^T \mathbf{\Gamma} = \mathcal{D}^m \mathbf{u}^T \tilde{\mathbf{M}}. \quad (4.37)$$

Since  $\mathbf{u}^T \tilde{\mathbf{M}} = \mathbf{u}^T$  because of equation (4.19) we can see that  $\mathbf{u}^T$  is a left eigenvector of  $\mathbf{\Gamma}$ :

$$\mathbf{u}^T \mathbf{\Gamma} = \mathcal{D}^m \mathbf{u}^T. \quad (4.38)$$

**Eigenvector of the Péclet matrices**

Since  $\mathbf{u}^T$  is a left eigenvector of  $\mathbf{\Gamma}$  it is a left eigenvector of  $\mathbf{\Gamma}^{-1}$  as well:

$$\mathbf{u}^T \mathbf{\Gamma}^{-1} = \frac{1}{\mathcal{D}^m} \mathbf{u}^T. \quad (4.39)$$

As a result,  $\mathbf{u}^T$  is also a left eigenvector of the Péclet matrix  $\mathbf{P}$ :

$$\mathbf{u}^T \mathbf{P} = \rho u \delta x \mathbf{u}^T \mathbf{\Gamma}^{-1} = \rho u \delta x \frac{1}{\mathcal{D}^m} \mathbf{u}^T \equiv P^m \mathbf{u}^T, \quad (4.40)$$

where we defined the ‘constraint’ Péclet number as:  $P^m = \rho u \delta x / \mathcal{D}^m$ . Note that this form of the ‘constraint’ Péclet number can be understood from equation (4.26).

**Eigenvector of the discretization matrices**

To proceed with the proof, we diagonalize the Péclet matrix using the left eigenvectors:

$$\mathbf{P} = \mathbf{W}^{-1} \mathbf{\Lambda} \mathbf{W} = \mathbf{W}^{-1} \begin{pmatrix} \lambda_1 & & \\ & \ddots & \\ & & \lambda_N \end{pmatrix} \mathbf{W}, \quad (4.41)$$

$$B(\mathbf{P}) = \mathbf{W}^{-1} B(\mathbf{\Lambda}) \mathbf{W} = \mathbf{W}^{-1} \begin{pmatrix} B(\lambda_1) & & \\ & \ddots & \\ & & B(\lambda_N) \end{pmatrix} \mathbf{W}, \quad (4.42)$$

where  $\mathbf{W}$  contains the left eigenvectors of  $\mathbf{P}$  as its rows. Multiplying with  $\mathbf{W}$  gives:

$$\mathbf{W} B(\mathbf{P}) = B(\mathbf{\Lambda}) \mathbf{W} = \begin{pmatrix} B(\lambda_1) & & \\ & \ddots & \\ & & B(\lambda_N) \end{pmatrix} \mathbf{W}. \quad (4.43)$$



Since  $\mathbf{u}^T$  is one of the rows of  $\mathbf{W}$ , we can conclude that applying the Bernoulli function to the Péclet matrix does not change the left eigenvectors, but only the corresponding eigenvalues:

$$\mathbf{u}^T B(\mathbf{P}) = B(P^m) \mathbf{u}^T. \quad (4.44)$$

Since  $\mathbf{A}_E$ ,  $\mathbf{A}_W$  and  $\mathbf{A}_C$  are given by (3.33),  $\mathbf{u}^T$  is also a left eigenvector of the discretization matrices:

$$\mathbf{u}^T \mathbf{A}_E = \frac{1}{\delta x_e} \mathcal{D}_e^m B(P_e^m) \mathbf{u}^T, \quad \mathbf{u}^T \mathbf{A}_W = \frac{1}{\delta x_w} \mathcal{D}_w^m B(-P_w^m) \mathbf{u}^T. \quad (4.45)$$

The discretization coefficients of the discrete equation (4.30) for  $\sigma^m$  are thus given by:

$$a_E = \frac{1}{\delta x_e} \mathcal{D}_e^m B(P_e^m), \quad a_W = \frac{1}{\delta x_w} \mathcal{D}_w^m B(-P_w^m), \quad a_C = a_E + a_W. \quad (4.46)$$

It can be seen that this result is the scalar exponential scheme applied to equation (4.26).

As explained in the beginning of this section, this form of the discrete equation for  $\sigma^m$  guarantees mass conservation without discretization error. Note that the solution  $\sigma^m = 1$  can only be obtained up to machine accuracy when the discretization scheme does not change the eigenvector  $\mathbf{u}^T$  of the discretization matrices. This is guaranteed by the coupled discretization method, but not by the scalar exponential scheme from Chapter 3. Without flow, both methods are equivalent, in all other cases mass conservation is not guaranteed by the scalar exponential scheme from Chapter 3 and the coupled discretization method should be used.

#### 4.6 Test case: Mixing of $\text{H}_2\text{O}$ , $\text{H}_2$ and $\text{N}_2$

As a test for the mass constraint and the discretization scheme the two dimensional test model as described in [37] was used. The geometry of the domain and the boundary conditions at the inlets can be seen in Figure 4.1. At the other boundaries, homogeneous Neumann boundary conditions are applied.

First, the model was run without flow, as in [37]. Subsequently, the model was run with a constant mass flux  $\rho u$  in the  $x$ -direction of  $0.002 \text{ kg m}^{-2} \text{ s}^{-1}$ . Calculations were performed with the scalar and the coupled exponential scheme on a grid of 80 by 80 gridpoints.

The results of both runs as calculated with the coupled exponential scheme are shown in Figure 4.2. Comparing the simulations with and without flow, it can be seen that in the case with flow the mass fractions are more strongly determined by their upwind values, as expected. In the case without flow, both the scalar and coupled exponential scheme converged in 19 iterations. The calculation time was 11.19 s for the scalar scheme, and 10.89 s for the coupled scheme on a regular desktop PC. As expected, the mass constraint was exactly satisfied without discretization error in both discretization schemes. In Figure 4.3 the result for the coupled scheme is

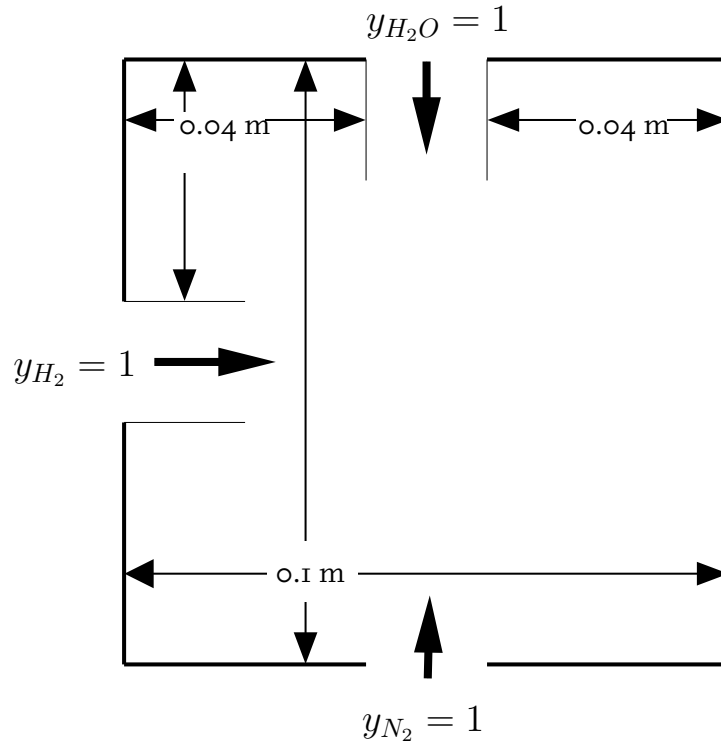
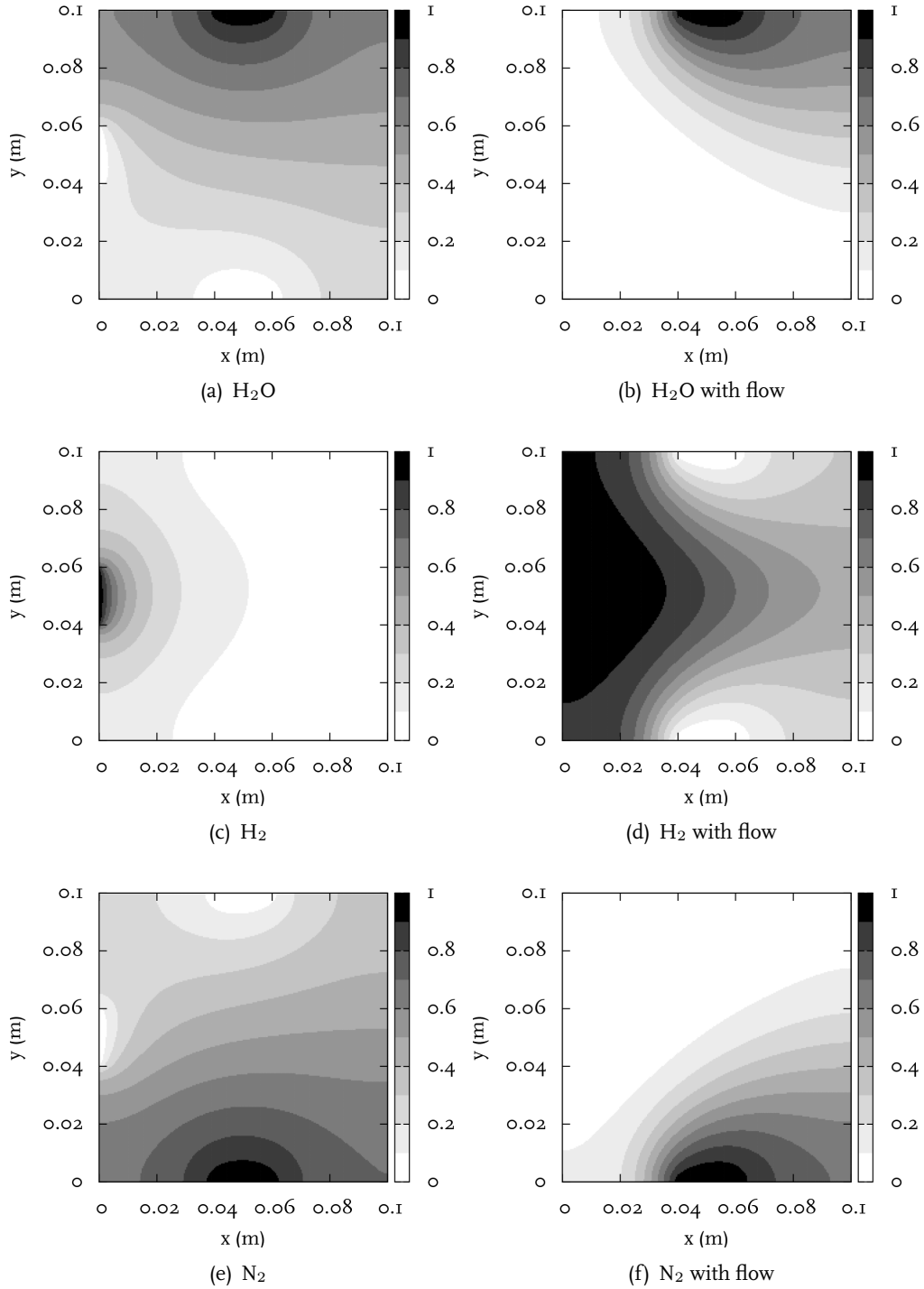


Figure 4.1: Geometry of the 2-D test problem.

shown. However, with flow, the mass constraint was not exactly satisfied for the scalar exponential scheme and no convergence was obtained, showing the incapability of the scalar scheme for simulations with flow. The coupled exponential scheme converged in 20 iteration steps in 16.3 s and mass conservation was satisfied. We can conclude that the computational cost of the scalar and the coupled exponential scheme are comparable, but the coupled scheme is more robust.

## 4.7 Discussion

In this chapter, a generalization of the exponential discretization scheme was used to discretize the fluxes resulting from the Stefan-Maxwell equations. For the Stefan-Maxwell equations the non-singular formulation of [38, 15] was used. In this formulation, the mass constraint is not applied explicitly, but is a result of the continuity equations, the boundary conditions and the diffusion algorithm. Since there is no need to select a species to account for the constraint, this formulation is especially useful for mixtures without dominant species. It was shown that with the generalized, coupled exponential discretization scheme the numerical solution can satisfy the mass conservation constraint exactly.



**Figure 4.2:** Species mass fractions with and without flow as calculated with the coupled exponential scheme. In the case with flow, the scalar exponential scheme did not converge.

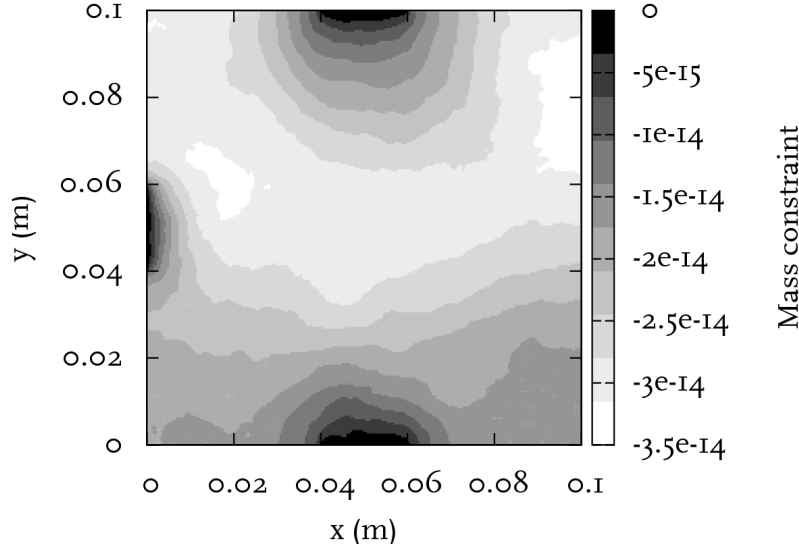


**Figure 4.3:** The mass constraint  $1 - \sum_i y_i$ . As can be seen mass conservation is fulfilled up to machine accuracy.

The test results confirmed that the mass constraint is indeed satisfied exactly with the coupled exponential discretization scheme, independent of the Péclet numbers. Furthermore, the coupled exponential scheme gives physical solutions for all Péclet numbers. Scalar discretization of the different flux contributions does neither guarantee mass conservation, nor physical solutions for simulations with convection. In some cases, the simulations with scalar discretization did not even converge.

The discretization scheme presented in Chapter 3 makes it possible to actually use the method as presented in [38, 15] in simulations of mixtures, where the diffusive fluxes of the different constituents are coupled. Examples of such mixtures can be found in combustion problems, NLTE plasma models and simulations of elemental demixing in LTE plasmas. Note that the method presented here is limited to mixtures with neutral species. In the next chapters, we will extend the non-singular formulation of the Stefan-Maxwell equations to plasmas. This extension is not straightforward; complications include the mass disparity between electrons and heavy particles [45], singularities due to the ambipolar constraint [45] and anisotropy of diffusive fluxes in magnetized plasmas [46].



## Chapter 5

# Ambipolar diffusion

This chapter is based on:

*On the ambipolar constraint in multi-component diffusion problems*, Peerenboom, K.S.C., Dijk, J. van, Goedheer, W.J., Mullen, J.J.A.M. van der, Journal of Computational Physics, 230(10), 3651-3655, 2011

### 5.1 Introduction

The diffusion velocities in multi-component systems such as plasmas are governed by the Stefan-Maxwell equations. As discussed in [38], the mass flux constraint on these diffusion velocities gives rise to a singularity in the resulting set of continuity equations. In ambipolar plasmas, the current prescription puts an extra constraint on the diffusion velocities. Similar to the mass flux constraint, this constraint introduces an extra singularity in the set of continuity equations.

In his extensive paper on ambipolar diffusion [45], Giovangigli identifies this singularity and hints at a possible solution. Here, we will work out the details and obtain a regularized (non-singular) form of the ambipolar diffusion matrix. In addition, we will show that with this regularized ambipolar diffusion matrix and the correct discretization scheme, quasi-neutrality will follow from the numerical method; it does not need to be imposed explicitly.

### 5.2 Constraints and singularities

The mass fraction  $y_i = \rho_i / \rho$  of a species  $i$  follows from the continuity equation:

$$\frac{\partial}{\partial t} (\rho y_i) + \nabla \cdot (\rho \vec{v} y_i) + \nabla \cdot (\rho \vec{v}_i y_i) = m_i \omega_i, \quad (5.1)$$

with  $\rho_i = n_i m_i$  the mass density of species  $i$  with number density  $n_i$  and mass  $m_i$ ,  $\rho = \sum_i \rho_i$  the total mass density,  $\vec{v}$  the mass averaged bulk velocity,  $\vec{v}_i$  the diffusion velocity and  $m_i \omega_i$  the mass production source term. The diffusion velocity is defined as the velocity with respect to the mass averaged velocity:

$$\vec{v}_i = \vec{u}_i - \vec{v}, \quad (5.2)$$

where  $\vec{u}_i$  is the total velocity of species  $i$ . By their definition, the mass fractions are subject to the constraint

$$\sum_i y_i = 1, \quad (5.3)$$

and the diffusion velocities to the constraint

$$\sum_i y_i \vec{v}_i = 0. \quad (5.4)$$

As shown in [38], straightforward application of this constraint for the velocities gives rise to a degenerate set of continuity equations.

In plasmas, the drift of charged particles in electric fields causes charge separations over a typical length scale of the Debye length  $\lambda_D$ . This charge separation leads to an electric field, which can be calculated with Poisson's equation. In plasmas where  $\lambda_D$  is small, this approach is not very efficient, since it requires excessively fine meshes. In these plasmas, it is more appropriate to consider the electric field in the limit of vanishing Debye length.

In the limit of vanishing Debye length, the plasma becomes quasi-neutral and, as explained in Chapter 2, the current should be divergence free to maintain this quasi-neutrality. The electric field necessary to maintain this situation is called the ambipolar field  $\vec{E}_{\text{amb}}$ . The assumption of an ambipolar plasma puts extra constraints on the mass fractions and the diffusion velocities. The *quasi-neutrality constraint* can be expressed as:

$$\sum_i \frac{q_i y_i}{m_i} = 0, \quad (5.5)$$

which is the counterpart of (5.3), but now for charge instead of mass. The constraint for the diffusion velocities is less straightforward. It is often assumed in the ambipolar case that the current is zero, but this is not a necessary condition. Instead, it is sufficient that the current is divergence free. Therefore we apply the following *current constraint*:

$$\vec{j} = \sum_i n_i q_i \vec{v}_i = \vec{j}_{\text{ext}}, \quad \nabla \cdot \vec{j}_{\text{ext}} = 0, \quad (5.6)$$

with  $\vec{j}_{\text{ext}}$  the external current density. When we assume Ohm's law, the external current density is related to the external electric field  $\vec{E}_{\text{ext}}$  via:

$$\vec{j}_{\text{ext}} = \sigma \vec{E}_{\text{ext}}, \quad (5.7)$$

where  $\sigma$  is the electrical conductivity. Similar to (5.4), the current constraint causes singular behavior. This can be demonstrated by considering a steady-state situation. Multiplying all continuity equations with  $q_i/m_i$  and summing over all species gives:

$$\sum_i \left( \nabla \cdot \left( \rho \vec{v}_i \frac{q_i y_i}{m_i} \right) + \nabla \cdot \left( \rho \vec{v}_i \frac{q_i y_i}{m_i} \right) \right) = \sum_i q_i \omega_i. \quad (5.8)$$

Since no net charge is produced or destroyed in reactions, the sum on the right hand side of this equation is zero. Introducing the ‘charge-neutrality species’  $\sigma^c = \sum_i q_i y_i / m_i$  and applying constraint (5.6) gives:

$$\nabla \cdot (\rho \vec{v} \sigma^c) = 0. \quad (5.9)$$

This equation becomes degenerate for stagnation points, where  $\vec{v} = \vec{0}$ . As in the mass constraint, this degeneracy is due to the lack of dissipative terms, but now for the ‘charge-neutrality species’  $\sigma^c$ . A solution for this singularity is presented in Section 5.5. The next section will explain how the ambipolar diffusion matrix is obtained.

### 5.3 The ambipolar diffusion matrix

The solution for the singularity induced by the current constraint is found in adding dissipative (diffusive) terms to the expressions for the diffusion velocities without changing the solution. First, consider the original expressions for the diffusion velocities. As in Chapter 4, the Stefan-Maxwell equations can be written as [38, 47]:

$$\mathbf{F}\mathbf{v} = -\mathbf{d}, \quad (5.10)$$

or in the dual formulation:

$$\mathbf{v} = -\mathbf{D}\mathbf{d}, \quad (5.11)$$

with  $\mathbf{v} = (v_1, \dots, v_N)^T$  the vector of diffusion velocities and  $\mathbf{d} = (d_1, \dots, d_N)^T$  the vector of driving forces. In the following analysis, we will use the formulation of equation (5.11). Besides normal concentration diffusion, we will now also take into account drift in the external and ambipolar electric field in the driving forces:

$$\mathbf{d} = \partial\mathbf{x} - \mathbf{z}\vec{E}_{ext}/p - \mathbf{z}\vec{E}_{amb}/p, \quad (5.12)$$

where  $p$  is the pressure and  $\mathbf{z} = (n_1 q_1, \dots, n_N q_N)^T$ . Substitution of the driving forces in (5.11) gives:

$$\mathbf{v} = -\mathbf{D} \left( \partial\mathbf{x} - \mathbf{z}\vec{E}_{ext}/p - \mathbf{z}\vec{E}_{amb}/p \right). \quad (5.13)$$

The ambipolar field is still present in this expression for the diffusion velocities, but can be eliminated by applying constraint (5.6). When we define the inner product in species space as  $\langle \mathbf{a}, \mathbf{b} \rangle = \sum_i a_i b_i$ , the current constraint (5.6) can alternatively be written as:

$$\langle \mathbf{z}, \mathbf{v} \rangle = \sigma \vec{E}_{ext}. \quad (5.14)$$

By taking the inner product of  $\mathbf{z}$  with (5.13) and using the definition of the conductivity  $\sigma = \langle \mathbf{z}, \mathbf{D}\mathbf{z} \rangle / p$ , the following expression for the ambipolar field is obtained:

$$\vec{E}_{amb}/p = \frac{\langle \mathbf{z}, \mathbf{D}\partial\mathbf{x} \rangle}{\langle \mathbf{z}, \mathbf{D}\mathbf{z} \rangle}. \quad (5.15)$$



Backsubstitution in expression (5.13) for the diffusion velocities gives:

$$\begin{aligned}\mathbf{v} &= -\left(\mathbf{D} - \frac{\mathbf{D}\mathbf{z} \otimes \mathbf{D}\mathbf{z}}{\langle \mathbf{z}, \mathbf{D}\mathbf{z} \rangle}\right) \partial \mathbf{x} + \mathbf{D}\mathbf{z} \vec{E}_{ext}/p, \\ &= -\hat{\mathbf{D}} \partial \mathbf{x} + \mathbf{D}\mathbf{z} \vec{E}_{ext}/p\end{aligned}\quad (5.16)$$

where  $\otimes$  denotes the dyadic product in species space:  $\mathbf{a} \otimes \mathbf{b} = (a_i b_j)$ . In the next section, we will now demonstrate that the general expression for the ambipolar diffusion matrix  $\hat{\mathbf{D}}$  reduces to well-known results for two limiting cases.

To solve equation (5.1) for the species mass fractions, an expression for the diffusive mass fluxes in terms of (the gradients of) the mass fractions is needed. As in Chapter 4, the mass fluxes can be obtained by multiplication with the matrix  $\mathbf{R} = \text{diag}(\rho y_i)$ :

$$\mathbf{J} = -\mathbf{R}\hat{\mathbf{D}}\partial \mathbf{x} + \mathbf{R}\mathbf{D}\mathbf{z} \vec{E}_{ext}/p. \quad (5.17)$$

The gradients of the mole fractions can be converted to the gradients of the mass fractions by using the matrix  $\tilde{\mathbf{M}}$  from Chapter 4:

$$\mathbf{J} = -\mathbf{R}\hat{\mathbf{D}}\tilde{\mathbf{M}}\partial \mathbf{y} + \mathbf{R}\mathbf{D}\mathbf{z} \vec{E}_{ext}/p. \quad (5.18)$$

The drift term  $\mathbf{D}\mathbf{z} \vec{E}_{ext}/p$  is written in terms of the mass fractions as follows:

$$\mathbf{J} = -\mathbf{R}\hat{\mathbf{D}}\tilde{\mathbf{M}}\partial \mathbf{y} + \mathbf{R}\mathbf{D}\mathbf{z} \otimes \mathbf{u} \mathbf{y} \vec{E}_{ext}/p. \quad (5.19)$$

Note that this does not change the solution since  $\langle \mathbf{u}, \mathbf{y} \rangle = \sigma^m = 1$ .

## 5.4 Analytical examples

**Ambipolar diffusion in a fully ionized plasma** Consider the case that the plasma is fully ionized. In this case there are only two species, electrons and ions, and we know that the solution must be given by  $x_+ = x_- = 1/2$ . If the ion mass fraction and charge density are given by  $y_+ = y$  and  $z_+ = z$ , respectively, we know from the mass and charge constraint that the electron mass fraction and charge density are given by  $y_- = 1 - y$  and  $z_- = -z$ . The diffusion coefficient matrix  $\mathbf{D}$  is the same as for the binary mixture in Chapter 4:

$$\begin{aligned}\mathbf{D} &= \left(\mathbf{F} + \alpha \mathbf{y} \otimes \mathbf{y}\right)^{-1} - \frac{1}{\alpha} \mathbf{u} \otimes \mathbf{u}, \\ &= \begin{pmatrix} f + \alpha y^2 & -f + \alpha y(1-y) \\ -f + \alpha y(1-y) & f + \alpha(1-y)^2 \end{pmatrix}^{-1} - \frac{1}{\alpha} \begin{pmatrix} 1 & 1 \\ 1 & 1 \end{pmatrix}, \\ &= \frac{1}{f} \begin{pmatrix} (1-y)^2 & -y(1-y) \\ -y(1-y) & y^2 \end{pmatrix}.\end{aligned}$$

This result is independent of  $\alpha$ , as should be the case. Calculation of the ambipolar diffusion coefficient matrix gives:

$$\begin{aligned}\mathbf{D}\mathbf{z} &= \frac{1}{f} \begin{pmatrix} z(1-y) \\ -zy \end{pmatrix}, \\ \langle \mathbf{z}, \mathbf{D}\mathbf{z} \rangle &= \frac{1}{f} z^2, \\ \mathbf{D}\mathbf{z} \otimes \mathbf{D}\mathbf{z} &= \frac{1}{f^2} \begin{pmatrix} z^2(1-y)^2 & -z^2y(1-y) \\ -z^2y(1-y) & z^2y^2 \end{pmatrix}, \\ \mathbf{D} - \frac{\mathbf{D}\mathbf{z} \otimes \mathbf{D}\mathbf{z}}{\langle \mathbf{z}, \mathbf{D}\mathbf{z} \rangle} &= \begin{pmatrix} 0 & 0 \\ 0 & 0 \end{pmatrix}.\end{aligned}$$

The diffusion velocities are given by:

$$\begin{aligned}\mathbf{v} &= - \left( \mathbf{D} - \frac{\mathbf{D}\mathbf{z} \otimes \mathbf{D}\mathbf{z}}{\langle \mathbf{z}, \mathbf{D}\mathbf{z} \rangle} \right) \partial \mathbf{x} + \frac{\vec{E}_{ext}}{p} \mathbf{D}\mathbf{z}, \\ &= \frac{z\vec{E}_{ext}}{pf} \begin{pmatrix} 1-y \\ -y \end{pmatrix}.\end{aligned}$$

It can be seen that in the fully ionized case diffusion proportional to concentration gradients is completely absent and only forced diffusion in an external electric field is present. The electrons and ions drift in opposite directions and the electrons are much faster since  $y \gg 1-y$ . The absence of diffusion is expected since in the fully ionized case the plasma reduces to one fluid with fixed composition  $x_+ = x_- = 1/2$ .

**Classical ambipolar diffusion** Consider a plasma with three species: neutrals, ions and electrons. The neutral species form the dominant background gas, the electrons and ions are only present in traces:  $y_0 \approx 1, y_+ \approx 0, y_- \approx 0$ . The plasma is quasi-neutral:  $z_+ = -z_- = z, x_+ = x_- = x$ . In this case it is expected that the multicomponent diffusion expressions reduce to Fickian diffusion, where both the electrons and the ions diffuse with twice the original ion diffusion coefficient if  $T_e = T_h$ . Neglecting the external electric field, the mass fluxes are given by:

$$\mathbf{J} = -\mathbf{R}\mathbf{D} \left( \mathbf{I} - \frac{\mathbf{z} \otimes \mathbf{D}\mathbf{z}}{\langle \mathbf{z}, \mathbf{D}\mathbf{z} \rangle} \right) \partial \mathbf{x}.$$

Using the results from Section 4.4 for the dilute mixture, we obtain:

$$\begin{aligned}\mathbf{I} - \frac{\mathbf{z} \otimes \mathbf{D}\mathbf{z}}{\langle \mathbf{z}, \mathbf{D}\mathbf{z} \rangle} &= \begin{pmatrix} 1 & 0 & 0 \\ 0 & \frac{f_{+0}}{f_{+0}+f_{-0}} & \frac{f_{+0}}{f_{+0}+f_{-0}} \\ 0 & \frac{f_{-0}}{f_{+0}+f_{-0}} & \frac{f_{-0}}{f_{+0}+f_{-0}} \end{pmatrix}, \\ \mathbf{J} &= -\rho \begin{pmatrix} 0 & -\frac{y_+y_0^2}{f_{+0}} & -\frac{y_-y_0^2}{f_{-0}} \\ 0 & \frac{y_0^2y_+}{f_{+0}} & 0 \\ 0 & 0 & \frac{y_0^2y_-}{f_{-0}} \end{pmatrix} \begin{pmatrix} 1 & 0 & 0 \\ 0 & \frac{f_{+0}}{f_{+0}+f_{-0}} & \frac{f_{+0}}{f_{+0}+f_{-0}} \\ 0 & \frac{f_{-0}}{f_{+0}+f_{-0}} & \frac{f_{-0}}{f_{+0}+f_{-0}} \end{pmatrix} \partial \mathbf{x},\end{aligned}$$

Using the fact that  $f_{+0} \gg f_{-0}$ , we obtain:

$$\mathbf{J} \approx -\frac{\rho y_0^2}{f_{+0}} \begin{pmatrix} 0 & -(y_+ + y_-) & -(y_+ + y_-) \\ 0 & y_+ & y_+ \\ 0 & y_- & y_- \end{pmatrix} \partial \mathbf{x}.$$

Both the electrons and the ions diffuse with two times the ion diffusion coefficient. This is the classical result for ambipolar diffusion for the case  $T_e = T_h$ .

### 5.5 Regularization

As mentioned in [45], the vectors  $\mathbf{y}$  and  $\mathbf{z}$  are in the nullspace of the ambipolar diffusion matrix  $\hat{\mathbf{D}}$ , which means that the matrix is singular. In the beginning of Section 5.2, we have already diagnosed that this is due to the lack of dissipative terms for the ‘charge neutrality species’  $\sigma^c$  and the ‘mass constraint species’  $\sigma^m$ . As hinted on the last page of [45], a possible solution for this singularity is to add diffusive terms. Here we will work out such an approach in more detail. Regularization of the ambipolar diffusion matrix can be established in the following way:

$$\mathbf{v} = -\hat{\mathbf{D}}\tilde{\mathbf{M}}\partial\mathbf{y} - \beta\mathbf{u} \otimes \mathbf{u}\partial\mathbf{y} - \gamma\mathbf{r} \otimes \mathbf{r}\partial\mathbf{y} + \mathbf{D}\mathbf{z} \otimes \mathbf{u}\mathbf{y}\vec{E}_{ext}/p, \quad (5.20)$$

where  $\beta$  and  $\gamma$  are free parameters and  $\mathbf{r}$  is the vector  $\mathbf{r} = (q_1/m_1, \dots, q_N/m_N)^T$ . To establish that the regularization gives the required diffusive terms for equation (5.9), the parameters  $\beta$  and  $\gamma$  must be chosen positive. In practice, these parameters are chosen to be  $\beta = \max(\mathcal{D}_{ij})$  and  $\gamma = 10^5 \langle \mathbf{r}, \mathbf{D}\mathbf{r} \rangle / \langle \mathbf{r}, \mathbf{r} \rangle^2$ . The factor of  $10^5$  is of the order of magnitude of the heavy particle to electron mass ratio.

We will now derive new expressions for the mass flux and the current constraint based on these regularized expressions for the diffusion velocities. First we take the inner product of (5.20) with  $\mathbf{y}$  to obtain the mass flux. The first term on the right hand side is zero, since  $\mathbf{y}$  is in the nullspace of  $\hat{\mathbf{D}}$ . The third term is also zero, because of quasi-neutrality. Finally, the fourth term is zero since  $\mathbf{y}$  is in the nullspace of  $\mathbf{D}$ . As a result, the mass flux constraint now reads:

$$\sum_i n_i m_i \vec{v}_i = -\mathcal{D}^m \nabla \sigma^m, \quad (5.21)$$

with  $\mathcal{D}^m = \rho\beta\sigma^m$ . Similarly, we can evaluate the inner product of (5.20) with  $\mathbf{z}$ . The first term on the right hand side is again zero, since  $\mathbf{z}$  is in the nullspace of  $\hat{\mathbf{D}}$  as well. The second term is zero because of quasi-neutrality. This results in the following expression for the current:

$$\sum_i n_i q_i \vec{v}_i = -\mathcal{D}^c \nabla \sigma^c + \sigma \vec{E}_{ext}, \quad (5.22)$$

with  $\mathcal{D}^c = \gamma \langle \mathbf{z}, \mathbf{r} \rangle$ . With the above expressions for the mass flux and current constraint, non-degenerate equations for  $\sigma^c$  and  $\sigma^m$  can be found. Summation of the

species continuity equations (5.1) and substitution of (5.21) results in:

$$\nabla \cdot (\rho \vec{v} \sigma^m) - \nabla \cdot (\mathcal{D}^m \nabla \sigma^m) = 0. \quad (5.23)$$

Likewise, multiplication of (5.1) with  $q_i/m_i$ , summation over all species and substitution of (5.22) gives:

$$\nabla \cdot (\rho \vec{v} \sigma^c) - \nabla \cdot (\mathcal{D}^c \nabla \sigma^c) = 0, \quad (5.24)$$

where we have used  $\nabla \cdot (\sigma \vec{E}_{ext}) = 0$ . Note that the equations for  $\sigma^c$  and  $\sigma^m$  are elliptic. Comparing the equation for  $\sigma^c$  with (5.9), we can see that by regularization, we have obtained the desired diffusive terms for  $\sigma^c$ . According to the maximum principle for elliptic equations [42, 43], the maximum will be taken on the boundary. When the quasi-neutrality condition is therefore satisfied at the boundary, it will be satisfied in the entire domain.

## 5.6 Discrete mass and charge conservation

In the previous section we mentioned that *analytically*  $\sigma^m = 1$  and  $\sigma^c = 0$  will be satisfied in the entire domain due to the elliptic nature of (5.23) and (5.24). In this section we will show by deriving discrete equations for  $\sigma^m$  and  $\sigma^c$  that, when the coupled exponential scheme from Chapter 3 is used for discretization, this is true *numerically* as well for systems with  $\vec{E}_{ext} = 0$ . The derivation of these discrete equations for  $\sigma^m$  and  $\sigma^c$  will proceed largely along the same lines as the derivation in Chapter 4. We start with the discrete equation for the mass fraction vector  $\mathbf{y}$ :

$$\mathbf{A}_C \mathbf{y}_C = \mathbf{A}_E \mathbf{y}_E + \mathbf{A}_W \mathbf{y}_W + \mathbf{s}_C \Delta x. \quad (5.25)$$

Left multiplication with  $\mathbf{u}^T = (1, \dots, 1)$  and  $\mathbf{r}^T = (q_1/m_1, \dots, q_N/m_N)$ , respectively, gives:

$$\begin{aligned} \mathbf{u}^T \mathbf{A}_C \mathbf{y}_C &= \mathbf{u}^T \mathbf{A}_E \mathbf{y}_E + \mathbf{u}^T \mathbf{A}_W \mathbf{y}_W, \\ \mathbf{r}^T \mathbf{A}_C \mathbf{y}_C &= \mathbf{r}^T \mathbf{A}_E \mathbf{y}_E + \mathbf{r}^T \mathbf{A}_W \mathbf{y}_W, \end{aligned} \quad (5.26)$$

since  $\mathbf{u}^T \mathbf{s}_C = 0$  and  $\mathbf{r}^T \mathbf{s}_C = 0$ . If  $\mathbf{u}^T$  and  $\mathbf{r}^T$  are left eigenvectors of the discretization matrices  $\mathbf{A}_E$ ,  $\mathbf{A}_W$  and  $\mathbf{A}_C$ , this can be written as:

$$\begin{aligned} a_C^m \mathbf{u}^T \mathbf{y}_C &= a_E^m \mathbf{u}^T \mathbf{y}_E + a_W^m \mathbf{u}^T \mathbf{y}_W, \\ a_C^c \mathbf{r}^T \mathbf{y}_C &= a_E^c \mathbf{r}^T \mathbf{y}_E + a_W^c \mathbf{r}^T \mathbf{y}_W, \end{aligned} \quad (5.27)$$

where  $a_E^m$ ,  $a_W^m$ ,  $a_C^m$ ,  $a_E^c$ ,  $a_W^c$  and  $a_C^c$  are the corresponding eigenvalues. The above equation is equivalent to:

$$\begin{aligned} a_C^m \sigma_C^m &= a_E^m \sigma_E^m + a_W^m \sigma_W^m, \\ a_C^c \sigma_C^c &= a_E^c \sigma_E^c + a_W^c \sigma_W^c, \end{aligned} \quad (5.28)$$

with  $\sigma_E^m, \sigma_W^m, \sigma_C^m, \sigma_E^c, \sigma_W^c$  and  $\sigma_C^c$  denoting the mass constraint and charge neutrality species at the east, west and central point, respectively. We will now prove that  $\mathbf{u}^T$  and  $\mathbf{r}^T$  are indeed left eigenvectors of all the discretization matrices. First, we will focus on the matrix vector product of  $\mathbf{u}^T$  and  $\mathbf{r}^T$  with the flux diffusion matrix:

$$\begin{aligned}\mathbf{u}^T \mathbf{\Gamma} &= \mathbf{u}^T \mathbf{R} \left( \hat{\mathbf{D}} \tilde{\mathbf{M}} + \beta \mathbf{u} \otimes \mathbf{u} + \gamma \mathbf{r} \otimes \mathbf{r} \right), \\ \mathbf{r}^T \mathbf{\Gamma} &= \mathbf{r}^T \mathbf{R} \left( \hat{\mathbf{D}} \tilde{\mathbf{M}} + \beta \mathbf{u} \otimes \mathbf{u} + \gamma \mathbf{r} \otimes \mathbf{r} \right).\end{aligned}\quad (5.29)$$

By rewriting the vectors  $\mathbf{u}^T$  and  $\mathbf{r}^T$  in terms of  $\mathbf{y}^T$  and  $\mathbf{z}^T$ , and using the fact that the vectors  $\mathbf{y}$  and  $\mathbf{z}$  are in the nullspace of  $\hat{\mathbf{D}}$ , the following is obtained:

$$\begin{aligned}\mathbf{u}^T \mathbf{\Gamma} &= \rho \mathbf{y}^T \mathbf{R}^{-1} \mathbf{R} \left( \hat{\mathbf{D}} \tilde{\mathbf{M}} + \beta \mathbf{u} \otimes \mathbf{u} + \gamma \mathbf{r} \otimes \mathbf{r} \right) = \mathcal{D}^m \mathbf{u}^T, \\ \mathbf{r}^T \mathbf{\Gamma} &= \mathbf{z}^T \mathbf{R}^{-1} \mathbf{R} \left( \hat{\mathbf{D}} \tilde{\mathbf{M}} + \beta \mathbf{u} \otimes \mathbf{u} + \gamma \mathbf{r} \otimes \mathbf{r} \right) = \mathcal{D}^c \mathbf{r}^T,\end{aligned}\quad (5.30)$$

where  $\mathcal{D}^m = \rho \beta \sigma$  and  $\mathcal{D}^c = \gamma \langle \mathbf{z}, \mathbf{r} \rangle$ . We can thus conclude that  $\mathbf{u}^T$  and  $\mathbf{r}^T$  are left eigenvectors of the flux diffusion matrix. Now, we will consider the product with the Péclet matrix  $\mathbf{P} = \rho v \delta x \mathbf{\Gamma}^{-1}$ :

$$\begin{aligned}\mathbf{u}^T \mathbf{P} &= \mathbf{u}^T \rho v \delta x \mathbf{\Gamma}^{-1} = \rho v \delta x / \mathcal{D}^m \mathbf{u}^T = P^m \mathbf{u}^T, \\ \mathbf{r}^T \mathbf{P} &= \mathbf{r}^T \rho v \delta x \mathbf{\Gamma}^{-1} = \rho v \delta x / \mathcal{D}^c \mathbf{r}^T = P^c \mathbf{r}^T,\end{aligned}\quad (5.31)$$

where  $P^m = \rho v \delta x / \mathcal{D}^m$  and  $P^c = \rho v \delta x / \mathcal{D}^c$ . To prove that  $\mathbf{u}^T$  and  $\mathbf{r}^T$  are left eigenvectors of  $B(\mathbf{P})$ , we have to diagonalize to the left eigenvectors of the Péclet matrix:

$$\mathbf{P} = \mathbf{W}^{-1} \mathbf{\Lambda} \mathbf{W} = \mathbf{W}^{-1} \begin{pmatrix} \lambda_1 & & \\ & \ddots & \\ & & \lambda_N \end{pmatrix} \mathbf{W}, \quad (5.32)$$

$$B(\mathbf{P}) = \mathbf{W}^{-1} B(\mathbf{\Lambda}) \mathbf{W} = \mathbf{W}^{-1} \begin{pmatrix} B(\lambda_1) & & \\ & \ddots & \\ & & B(\lambda_N) \end{pmatrix} \mathbf{W}, \quad (5.33)$$

where  $\mathbf{W}$  contains the left eigenvectors as its rows. Multiplying with  $\mathbf{W}$  gives:

$$\mathbf{W} B(\mathbf{P}) = B(\mathbf{\Lambda}) \mathbf{W} = \begin{pmatrix} B(\lambda_1) & & \\ & \ddots & \\ & & B(\lambda_N) \end{pmatrix} \mathbf{W}, \quad (5.34)$$

so we can conclude that applying the Bernoulli function to the Péclet matrix does not change the left eigenvectors, but only the corresponding eigenvalues. With this result the product of  $\mathbf{u}^T$  and  $\mathbf{r}^T$  with the discretization matrices becomes:

$$\begin{aligned}\mathbf{u}^T \mathbf{A}_E &= 1/\delta x_e \mathcal{D}_e^m B(P_e^m) \mathbf{u}^T = a_E^m \mathbf{u}^T, \\ \mathbf{r}^T \mathbf{A}_E &= 1/\delta x_e \mathcal{D}_e^c B(P_e^c) \mathbf{r}^T = a_E^c \mathbf{r}^T.\end{aligned}\quad (5.35)$$

Similar expressions for the west and central discretization matrices can be derived, with which we arrive at (5.28). Note that the discrete equations for  $\sigma^m$  and  $\sigma^c$  have the form as if the scalar exponential scheme was applied to equation (5.23) and (5.24), respectively.

An interesting consequence of the discrete equations for  $\sigma^m$  and  $\sigma^c$  is that the central grid points are weighted averages of the east and west neighbors. Since  $\sigma_C^m$  is a weighted average, we can deduce from the discrete maximum principle that  $\sigma^m = 1$  will be satisfied in the entire domain. Suppose that  $\sigma_C^m$  is a local maximum:  $\sigma_C^m \geq \sigma_E^m, \sigma_C^m \geq \sigma_W^m$ . However, since  $\sigma_C^m$  is a weighted average the following needs to be true:  $\sigma_C^m = \sigma_E^m = \sigma_W^m$ . We can now take  $\sigma_E^m$  or  $\sigma_W^m$  and continue the procedure until we hit the boundary, where  $\sigma^m = 1$ . Therefore, all the points in the domain satisfy  $\sigma^m = 1$ , without discretization error. Similarly,  $\sigma^c = 0$  is satisfied without discretization error.

Note that the exact solution for the constraints (5.3) and (5.5) can only be obtained when the discretization scheme does not change the eigenvectors  $\mathbf{u}^T$  and  $\mathbf{r}^T$  of the flux diffusion matrix. For the scalar exponential scheme, this means that the exact solution for the constraints can only be obtained in the case without flow. In all other cases, mass and charge conservation is not guaranteed and the coupled discretization method should be used.

## 5.7 Test case: drift in a H, H<sup>+</sup>, electron mixture

As a test case for the mass and charge constraints, a modified version of the test model of Chapter 4 is used. The geometry is the same as in Chapter 4, but other species are used. At the left inlet the H<sup>+</sup> mass fraction was set to 0.999, at the bottom and top inlet the H<sup>+</sup> mass fraction was set to 1e-14. At all other boundaries homogeneous Neumann conditions were used. The H and electron fraction at the boundary were determined from the mass and charge neutrality constraint, respectively.

First, the model was run without electrical current. Subsequently, an electrical current was induced by applying a voltage of -100 V at the left inlet and grounding the right boundary. Calculations were performed with the coupled exponential scheme from Chapter 3 on a grid of 80 by 80 gridpoints.

In Figure 5.1, the results of the runs with and without applied potential difference can be seen. Comparing the results with and without voltage, it can be seen that applying the voltage has no effect on the accuracy of the mass constraint. The accuracy of the charge constraint, however, decreases by applying the voltage. This can be understood since there is no guarantee that charge conservation can be fulfilled up to machine accuracy when an external electric field is present.

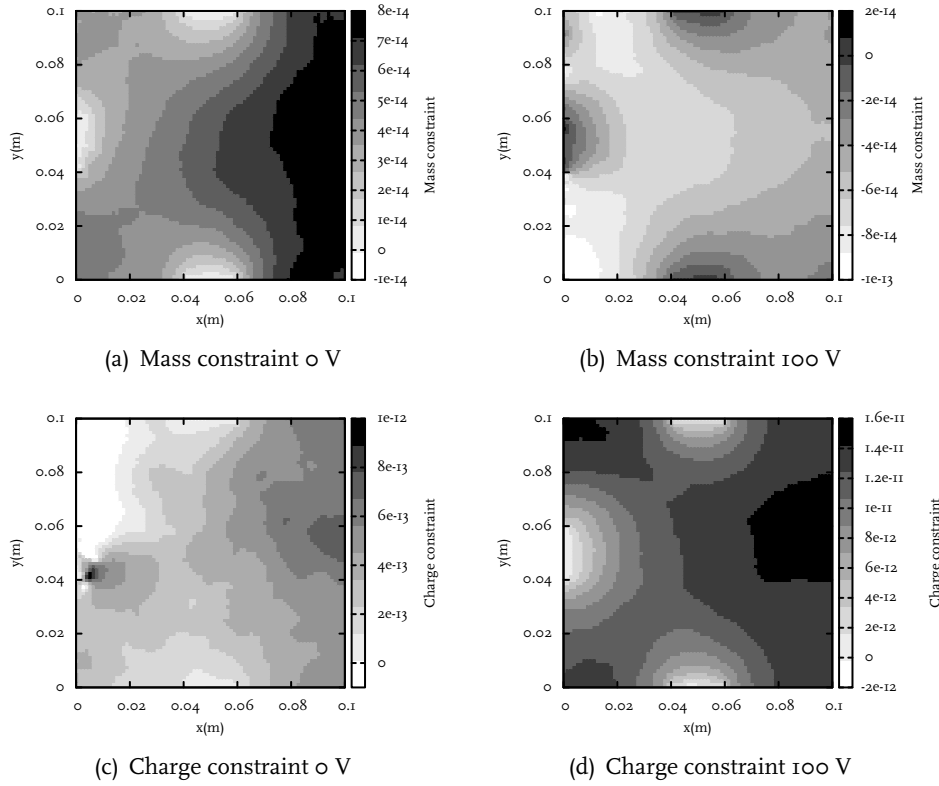


**Figure 5.1:** Mass ( $1 - \sum_i y_i$ ) and charge ( $\sum_i q_i y_i / m_i$ ) constraints with and without applied voltage difference.

## 5.8 Discussion

In this chapter, the multi-component diffusion formulation from Chapter 4 was extended to quasi-neutral mixtures with charge species. Instead of the usual ambipolar constraint, where the current is assumed to be zero, we allowed for a divergence free current. Mass and charge constraints were not applied explicitly, but followed as a result of the continuity equations, the boundary conditions, the diffusion algorithm and the discretization scheme. The test results confirmed that mass and charge constraints were indeed satisfied.

## Chapter 6

# Diffusion in magnetized plasmas

This chapter is based on:

*A finite volume model for multi-component diffusion in magnetically confined plasmas*  
Peerenboom, K.S.C., Dijk, J. van, Goedheer, W.J., Degrez, G, Mullen, J.J.A.M. van der, Journal of Physics D: Applied Physics, 44(19), 194006-1/8, 2011

**Abstract.** In this chapter the multi-component diffusion algorithm from Chapter 4 and 5 is extended to the case of magnetized plasmas. In magnetized plasmas the transport becomes anisotropic. The transport along the magnetic field lines does not change and the formalism of Chapter 4 and 5 can be used. The transport fluxes across and around the field lines become coupled and must be treated differently. In this chapter we discuss the strategy for treating the coupling between these directions.



### 6.1 Stefan-Maxwell equations in a magnetic field

In the presence of a magnetic field  $\vec{B}$ , the Stefan-Maxwell equations as presented in Chapter 4 and 5 have additional terms due to the Lorentz force and can be written as [46]:

$$\sum_l F_{kl} \vec{v}_l - \frac{n_k q_k}{p} \vec{v}_k \times \vec{B} + \frac{y_k}{p} \vec{j} \times \vec{B} = -\vec{d}_k, \quad (6.1)$$

with  $\mathbf{F} = (F_{kl})$  the friction matrix as introduced in Chapter 4,  $\vec{d}_k$  the diffusion driving force,  $n_k$  the number density,  $q_k$  the charge,  $p$  the pressure,  $y_k$  the mass fraction and  $\vec{j}$  the current density. The second term on the left hand side gives the Lorentz force acting on the diffusion velocity, while the third term appears since the diffusion velocities are defined with respect to the mass averaged bulk velocity. The diffusion driving force also has an extra term due to the Lorentz force acting on the mass averaged velocity. In the absence of pressure diffusion and thermophoresis, but in the presence of an electric field  $\vec{E}$ , the diffusion driving force is given by:

$$\vec{d}_k = \nabla x_k - \frac{n_k q_k}{p} \vec{E} - \frac{n_k q_k}{p} \vec{v} \times \vec{B}, \quad (6.2)$$

with  $x_k$  the mole fraction of species  $k$  and  $\vec{v}$  the mass averaged velocity of the plasma.

#### 6.1.1 Along, across and around the field lines

In this thesis, we assume that the plasma is cylindrically symmetric and that the magnetic field points in the axial direction. As explained in Chapter 2, we can introduce the cylindrical basis ( $\vec{e}_r$ ,  $\vec{e}_\phi$ ,  $\vec{e}_z$ ) and write any vector  $\vec{x}$  as  $\vec{x} = x^\perp \vec{e}_r + x^\odot \vec{e}_\phi + x^\parallel \vec{e}_z$ , where  $\parallel$ ,  $\perp$  and  $\odot$  indicate the directions along, across and around the field lines as given in Figure 6.1. In the direction along the field lines ( $\parallel$ ), the Stefan-Maxwell

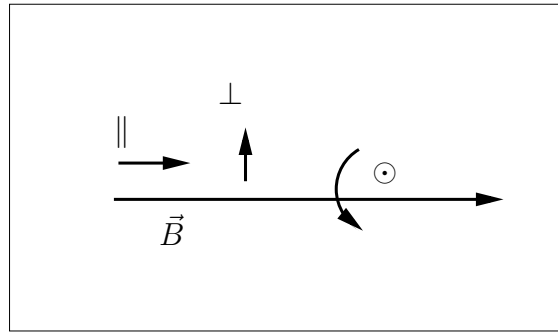


**Figure 6.1:** The directions along ( $\parallel$ ), across ( $\perp$ ) and around ( $\odot$ ) the magnetic field lines.

equations are not influenced by the magnetic field and can be written as:

$$\sum_l F_{kl} v_l^\parallel = d_k^\parallel. \quad (6.3)$$

The flow directions across ( $\perp$ ) and around ( $\odot$ ) the field lines are coupled:

$$\sum_l F_{kl} v_l^\perp - \frac{n_k q_k}{p} v_k^\odot B + \frac{y_k j^\odot B}{p} = -d_k^\perp, \quad (6.4)$$

$$\sum_l F_{kl} v_l^\odot + \frac{n_k q_k}{p} v_k^\perp B - \frac{y_k j^\perp B}{p} = -d_k^\odot. \quad (6.5)$$

The Stefan-Maxwell equations along the field lines can be solved independently from the other directions. The directions across and around the field lines need to be solved together, which can be done by putting together the  $\perp$  and  $\odot$  direction in a  $2N \times 2N$  system, with  $N$  the number of species. However, from a computational viewpoint, it is favorable to use complex arithmetic [48].

To facilitate coupled solving of the directions across and around the field lines, the Stefan-Maxwell equations are made complex by adding  $i$  ( $i^2 = -1$ ) times equation (6.5) to equation (6.4):

$$\begin{aligned} \sum_l F_{kl} (v_l^\perp + i v_l^\odot) - \frac{n_k q_k B}{p} (v_k^\odot - i v_k^\perp) + \frac{y_k B}{p} (j^\odot - i j^\perp) \\ = - (d_k^\perp + i d_k^\odot). \end{aligned} \quad (6.6)$$

Substitution of  $j^\perp = \sum_k n_k q_k v_k^\perp$  and  $j^\odot = \sum_k n_k q_k v_k^\odot$  gives:

$$\begin{aligned} \sum_l F_{kl} (v_l^\perp + i v_l^\odot) - \frac{n_k q_k B}{p} (v_k^\odot - i v_k^\perp) + \frac{y_k B}{p} \sum_l n_l q_l (v_l^\odot - i v_l^\perp) \\ = - (d_k^\perp + i d_k^\odot). \end{aligned} \quad (6.7)$$

When we introduce the complex diffusion velocity  $\tilde{v}_k = v_k^\perp + i v_k^\odot$ , this can be written as:

$$\sum_l F_{kl} \tilde{v}_l + i \frac{n_k q_k}{p} \tilde{v}_k B - i \frac{y_k}{p} \sum_l n_l q_l \tilde{v}_l B = - (d_k^\perp + i d_k^\odot). \quad (6.8)$$

Alternatively, matrix notation gives:

$$(\mathbf{F} + i (\mathbf{I} - \mathbf{y} \otimes \mathbf{u}) \mathbf{B}) \tilde{\mathbf{v}} = - (\mathbf{d}^\perp + i \mathbf{d}^\odot), \quad (6.9)$$

where  $\mathbf{B}$  is the matrix taking into account the Lorentz force:

$$\mathbf{B} = \text{diag} \left( \frac{n_i q_i B}{p} \right), \quad (6.10)$$

and  $\mathbf{u}$  and  $\mathbf{y}$  are the vectors  $\mathbf{u} = (1, \dots, 1)^\text{T}$ ,  $\mathbf{y} = (y_1, \dots, y_N)^\text{T}$ . As pointed out by Giovangigli [49], this system does not have convenient mathematical properties.

For example, the nullspace of  $\mathbf{F} + i(\mathbf{I} - \mathbf{y} \otimes \mathbf{u})\mathbf{B}$  is not known explicitly. This is inconvenient when we want to regularize the matrix. To improve the mathematical structure without changing the solution, the projector  $\mathbf{I} - \mathbf{u} \otimes \mathbf{y}$  is used:

$$(\mathbf{F} + i\mathbf{F}')\tilde{\mathbf{v}} = -(\mathbf{d}^\perp + i\mathbf{d}^\odot), \quad (6.11)$$

where the matrix  $\mathbf{F}'$  is given by [46, 50]:

$$\mathbf{F}' = (\mathbf{I} - \mathbf{y} \otimes \mathbf{u})\mathbf{B}(\mathbf{I} - \mathbf{u} \otimes \mathbf{y}). \quad (6.12)$$

The matrix  $\mathbf{F} + i\mathbf{F}'$  is symmetric, singular and has nullspace  $\mathbf{u}$ . Comparable to Chapters 4 and 5, there is a dual formulation for the magnetized case as well:

$$\tilde{\mathbf{v}} = -(\mathbf{D}^\perp + i\mathbf{D}^\odot)(\mathbf{d}^\perp + i\mathbf{d}^\odot). \quad (6.13)$$

As in previous chapters, the singularity in  $\mathbf{F} + i\mathbf{F}'$  can be removed by applying the mass flux constraint  $\sum_k y_k \tilde{v}_k = 0$  to the set of Stefan-Maxwell equations [38]. The diffusion matrices  $\mathbf{D}^\perp$  and  $\mathbf{D}^\odot$  can then be calculated from  $\mathbf{F} + i\mathbf{F}'$  using the following relation [46]:

$$(\mathbf{F} + i\mathbf{F}' + \alpha\mathbf{y} \otimes \mathbf{y})^{-1} = (\mathbf{D}^\perp + i\mathbf{D}^\odot + 1/\alpha\mathbf{u} \otimes \mathbf{u}), \quad (6.14)$$

where  $\alpha$  is a positive parameter. An appropriate choice for the free parameter  $\alpha$  is  $\alpha = 1/\max(\mathcal{D}_{ij})$  [15], since it guarantees that the elements of the matrices  $\mathbf{F}$  and  $\alpha\mathbf{y} \otimes \mathbf{y}$  have the same order of magnitude. Note that instead of direct inversion of the Stefan-Maxwell system, it is possible to use iterative methods as discussed for example in [46]. These iterative methods are computationally cheaper than direct inversion. We will not discuss this method here, since in our case the largest computational expense lies in solving the discretized species mass balances (Section 3.2), and not in the inversion of the Stefan-Maxwell system at each grid point.

The real part of expression (6.13) gives the diffusion velocity perpendicular to the magnetic field:

$$\mathbf{v}^\perp = -\mathbf{D}^\perp\mathbf{d}^\perp + \mathbf{D}^\odot\mathbf{d}^\odot. \quad (6.15)$$

The imaginary part gives the diffusion velocity around the field lines:

$$\mathbf{v}^\odot = -\mathbf{D}^\perp\mathbf{d}^\odot - \mathbf{D}^\odot\mathbf{d}^\perp. \quad (6.16)$$

The parallel diffusion velocity is not changed by the magnetic field and is given by:

$$\mathbf{v}^\parallel = -\mathbf{D}^\parallel\mathbf{d}^\parallel. \quad (6.17)$$

The driving forces still contain the ambipolar field. In the next section, we will explain how the ambipolar field can be eliminated from the equation.

### 6.1.2 The quasi-neutrality constraint

In the previous chapter, ambipolar diffusion for non-magnetized plasmas was discussed. To eliminate the ambipolar field from the diffusion driving forces, Ohm's law was used:

$$\vec{j} = \sigma \vec{E}_{ext}, \quad (6.18)$$

with  $\sigma$  the conductivity and  $\vec{E}_{ext}$  the external electric field. However, in magnetized plasmas an additional term is present in Ohm's law: the Hall current. When this Hall current is taken into account, Ohm's law is given by:

$$\vec{j} = \bar{\sigma} \left( \vec{E}_{ext} + \vec{v} \times \vec{B} \right), \quad (6.19)$$

with  $\bar{\sigma}$  the anisotropic conductivity tensor,  $\vec{v}$  the bulk velocity and  $\vec{B}$  the magnetic field. We will now derive the expressions for the diffusion velocities using Ohm's law including the Hall current to eliminate the ambipolar electric field.

For calculation of the ambipolar field in the presence of a magnetic field, distinction must be made between the directions along, across and around the magnetic field lines. Normally, without a magnetic field, the ambipolar field is calculated as the electric field that is necessary to prevent charge separation. When a magnetic field is present, this calculation applies along and across the magnetic field. Around the field lines, it is impossible for the electrons and ions to diffuse together. This can be explained with Figure 6.2. In the cylindrically symmetric plasma there is a radial gradient of charged particles. The magnetic field points out of the plane. Because of the opposite charge of the electrons and ions, the circling motion of the electrons is in the opposite direction of the motion of the ions. This means that their contribution to the current has the same sign, which is the mechanism behind the diamagnetic current<sup>1</sup>. Since current can flow around the field lines without causing charge separation, only for the direction along and across the field lines, the current constraint is applied:

$$\begin{aligned} j^{\parallel} &= \langle \mathbf{z}, \mathbf{v}^{\parallel} \rangle = \sigma^{\parallel} E_{ext}^{\parallel}, \\ j^{\perp} &= \langle \mathbf{z}, \mathbf{v}^{\perp} \rangle = \sigma^{\perp} E_{ext}^{\perp} + \sigma^{\perp} v^{\odot} B + \sigma^{\odot} v^{\perp} B. \end{aligned} \quad (6.20)$$

Eliminating the ambipolar electric field in the driving forces with the above current constraints gives the following expressions for the diffusion velocities:

$$\begin{aligned} \mathbf{v}^{\parallel} &= -\mathbf{D}^{\parallel} \left( \mathbf{I} - \frac{\mathbf{z} \otimes \mathbf{D}^{\parallel} \mathbf{z}}{\langle \mathbf{z}, \mathbf{D}^{\parallel} \mathbf{z} \rangle} \right) \partial_{\parallel} \mathbf{x} + \mathbf{D}^{\parallel} \mathbf{z} E_{ext}^{\parallel} / p, \\ \mathbf{v}^{\perp} &= -\mathbf{D}^{\perp} \left( \mathbf{I} - \frac{\mathbf{z} \otimes \mathbf{D}^{\perp} \mathbf{z}}{\langle \mathbf{z}, \mathbf{D}^{\perp} \mathbf{z} \rangle} \right) \partial_{\perp} \mathbf{x} + \mathbf{D}^{\perp} \mathbf{z} E_{ext}^{\perp} / p + \mathbf{D}^{\perp} \mathbf{z} v^{\odot} B / p + \mathbf{D}^{\odot} \mathbf{z} v^{\perp} B / p, \\ \mathbf{v}^{\odot} &= -\mathbf{D}^{\odot} \left( \mathbf{I} - \frac{\mathbf{z} \otimes \mathbf{D}^{\perp} \mathbf{z}}{\langle \mathbf{z}, \mathbf{D}^{\perp} \mathbf{z} \rangle} \right) \partial_{\perp} \mathbf{x} + \mathbf{D}^{\odot} \mathbf{z} E_{ext}^{\perp} / p + \mathbf{D}^{\odot} \mathbf{z} v^{\odot} B / p - \mathbf{D}^{\perp} \mathbf{z} v^{\perp} B / p. \end{aligned} \quad (6.21)$$

<sup>1</sup>This diamagnetic current will also induce a magnetic field. This effect will be neglected here.

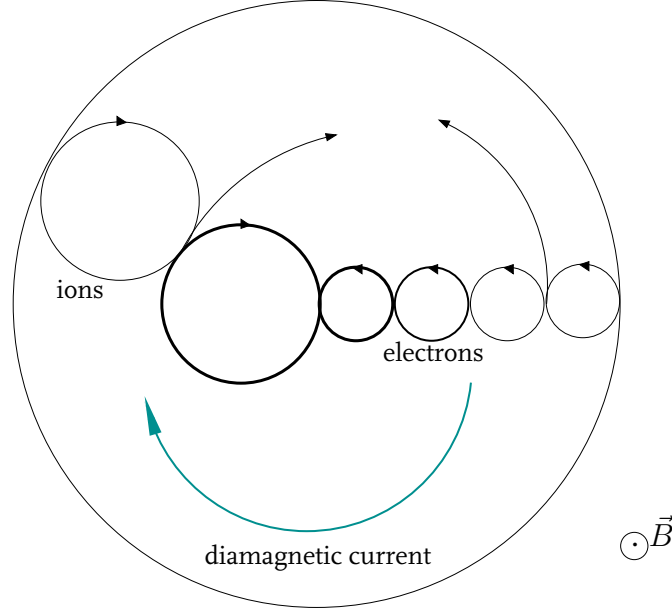


**Figure 6.2:** Diamagnetic current as a result of a radial density gradient. As long as there is a magnetic field, this diamagnetic current can not be zero.

Note that the matrices relating the diffusion velocities to the driving forces are singular and the nullspace is spanned by the vectors  $\mathbf{y}$  and  $\mathbf{z}$ . Regularization can be performed in the same way as in the Chapter 5, where the unmagnetized, ambipolar case was discussed.

## 6.2 Analytical example

Consider the case that the plasma is fully ionized. In this case there are only two species, electrons and ions, and we know that the solution must be given by  $x_+ = x_- = 1/2$ . If the ion mass fraction and charge density are given by  $y_+ = y$  and  $z_+ = z$  respectively, we know from the mass and charge constraint that the electron mass fraction and charge density are given by  $y_- = 1 - y$  and  $z_- = -z$ . What does the diffusion velocity look like in this case?

The diffusion coefficient matrices across and around the field lines are given by:

$$\mathbf{D}^\perp + i\mathbf{D}^\odot = \left( \mathbf{F} + i\mathbf{F}' + \alpha \mathbf{y} \otimes \mathbf{y} \right)^{-1} - \frac{1}{\alpha} \mathbf{u} \otimes \mathbf{u}.$$

Inserting the matrix coefficients gives:

$$\mathbf{D}^\perp + i\mathbf{D}^\odot = \begin{pmatrix} f + i\beta + \alpha y^2 & -f - i\beta + \alpha y(1 - y) \\ -f - i\beta + \alpha y(1 - y) & f + i\beta + \alpha(1 - y)^2 \end{pmatrix}^{-1} - \frac{1}{\alpha} \begin{pmatrix} 1 & 1 \\ 1 & 1 \end{pmatrix},$$

with  $\beta = (1 - y)^2 zB/p - y^2 zB/p$ . Inversion leads to:

$$\begin{aligned} \mathbf{D}^\perp + i\mathbf{D}^\odot &= \begin{pmatrix} \frac{1}{\alpha} + \frac{(1-y)^2}{f+i\beta} & \frac{1}{\alpha} - \frac{y(1-y)}{f+i\beta} \\ \frac{1}{\alpha} - \frac{y(1-y)}{f+i\beta} & \frac{1}{\alpha} + \frac{y^2}{f+i\beta} \end{pmatrix} - \frac{1}{\alpha} \begin{pmatrix} 1 & 1 \\ 1 & 1 \end{pmatrix} \\ &= \frac{1}{f+i\beta} \begin{pmatrix} (1-y)^2 & -y(1-y) \\ -y(1-y) & y^2 \end{pmatrix}. \end{aligned}$$

The real part gives the diffusion across the field lines:

$$\mathbf{D}^\perp = \frac{1}{1 + \beta^2/f^2} \frac{1}{f} \begin{pmatrix} (1-y)^2 & -y(1-y) \\ -y(1-y) & y^2 \end{pmatrix},$$

and the imaginary part the diffusion around the field lines:

$$\mathbf{D}^\odot = -\frac{1}{1 + f^2/\beta^2} \frac{1}{\beta} \begin{pmatrix} (1-y)^2 & -y(1-y) \\ -y(1-y) & y^2 \end{pmatrix}.$$

If we compare the result for  $\mathbf{D}^\perp$  with the analytical example of Chapter 5, we can see that the transport perpendicular to the field lines is reduced by a factor  $1 + \beta^2/f^2$ . Since  $\beta/f$  is the Hall parameter this is the classical result. For  $\beta = 0$ , the unmagnetized result from Chapter 5 is recovered and diamagnetic transport is absent.



## Chapter 7

# Supersonic expansion of argon in Magnum-PSI

This chapter is built on:

*Integral simulation of the creation and expansion of a transonic argon plasma*, Peerenboom, K.S.C., Goedheer, W.J., Dijk, J. van, Mullen, J.J.A.M. van der, Plasma Sources Science and Technology, 19(2), 025009-1/9, 2010

**Abstract.** A transonic argon plasma is studied in an integral simulation where both the plasma creation and expansion are incorporated in the same model. This integral approach allows for simulation of expanding plasmas where the Mach number is not known a priori. Results of this integral simulation are validated with an empirical relation for the shock position. Additionally, the effect of the nozzle geometry on the expansion is studied.



## 7.1 Introduction

Expanding plasma flows can be found in different applications. Besides Magnum-PSI, other examples are low pressure plasma spraying (LPPS) and plasma chemical vapor deposition (PCVD). Because of this wide occurrence, expanding plasmas are studied both experimentally and numerically. Numerical modeling of this type of plasma incorporates a number of challenges. First of all, the transonic flow field including one or more shocks must be described correctly. Secondly, due to the large hydrodynamic speeds, the plasma is most likely not in local thermodynamic equilibrium (LTE). As a consequence, the different constituents of the plasma will have different temperatures and the chemical composition can not be calculated using the laws of Boltzmann, Saha and Guldberg-Waage.

Different approaches have been used for the modeling of expanding plasmas. Modeling the plasma as a neutral gas, consisting of only one species, with gas dynamics equations is the simplest way to get basic insight in the flow field of a plasma jet. When comparing gas dynamics simulations of the shockwave structure in a supersonic plasma jet with experiments, gas dynamics simulations [5] show a repetitive pattern of shockwaves that damps out slowly. However, experiments [51] show a much smoother velocity field, with a rapid decay of the shockwave structures. This discrepancy can be explained by the fact that heat and momentum transport rates are much higher in a plasma than in a neutral gas due to the presence of charged particles. Furthermore, background pressures in expanding plasmas can be as low as a few Pa, see for example [52]. At such low pressures, gas dynamics equations can not always give an accurate description of the flow field. The gas dynamics approach is valid only when the Knudsen number  $Kn$ , which gives the ratio of the average mean free path of the gas atoms or molecules to the characteristic length scale of the flow is much smaller than unity. When the mean free path is comparable to or larger than the characteristic length ( $Kn \geq 1$ ), Direct Simulation Monte Carlo (DSMC) becomes a more suitable method for calculation of the flow field. DSMC calculations on expanding jets have been performed in for example [51, 53].

A more complete approach for expanding plasma flows is to combine the flow calculation with a composition calculation, taking into account more than one species. The composition can then be used to calculate realistic values for the transport coefficients like viscosity and heat conduction. However, combining shock wave simulations with a composition calculation in a plasma is far from easy. Most often, the composition calculation type is therefore chosen to be local thermodynamic equilibrium, see e.g. [54, 55]. This is an over-simplification, since due to the large flow velocities, supersonic plasmas are likely to be out of equilibrium. Furthermore, when the plasma is out of equilibrium, species can gain (or loose) energy by chemical processes at one place in the plasma and transport this energy to another part of the plasma. This can cause extra broadening of shock waves, which can not be taken into account by equilibrium calculations.

Only few non-equilibrium calculations, e.g. [56, 57], were carried out on super-

sonic plasma jets. These non-equilibrium simulations focused, however, on the expansion region. The plasma production was not incorporated in the models. At the inflow boundary, temperature and mass fraction profiles were assumed or taken from another model.

In this chapter we use an integral approach, where both plasma production in an arc and the consecutive expansion in a chamber are incorporated in the same model. Integral here refers to global in the sense that the domain is not split on the interface of the plasma source and the vacuum chamber. With this approach it is possible to study the effect of the arc on the expansion, and vice versa, without *a priori* knowledge of the Mach number and the profiles of the temperature and the chemical constituents at the inlet of the vacuum chamber. The results of this approach are validated with an empirical relation for the shock position. Additionally, the effect of the nozzle geometry on the expansion is studied.

This chapter starts by discussing the shockwave structure of expanding jets. Then, the solution procedure for flow calculation in Plasimo will be discussed in Section 7.3. Section 7.4 presents our model and numerical results are given in Section 7.5. This chapter ends with conclusions in Section 7.6

## 7.2 Underexpanded jet

The flow of plasma expanding from a nozzle into a vacuum chamber can be fully expanded, overexpanded or underexpanded [58, 59]. If the pressure at the outlet of the nozzle is lower than the chamber pressure, the flow is overexpanded. If the pressure at the outlet of the nozzle is higher than the pressure of the vacuum chamber, the flow is underexpanded. Both underexpanded and overexpanded flows show one or more shock waves. These shockwaves equalize the jet pressure with the background pressure. As the flow in Magnum-PSI is underexpanded we will only focus on under-expanded jets.

In an underexpanded jet, the background pressure is lower than the jet pressure, causing the jet to expand beyond the nozzle. In Figure 7.1 a photograph of the expansion in Magnum PSI can be seen. A shockwave pattern is visible. We can see the expansion as a dark region after the nozzle exit. The shock diamond shows up as a lighter region after the expansion.

In Figure 7.2 the shock structure of an underexpanded jet is schematically depicted. When leaving the nozzle (2), the pressure of the flow exceeds the background pressure. Therefore, the flow expands outward in the presence of expansion waves (5) to reduce the pressure. The expansion waves reflect from the jet boundary (6), forming compression waves (7). These compression waves can merge, creating an oblique shockwave (3). By passing the normal shock wave or Mach disk (4), which is oriented perpendicular to the flow direction, the pressure in the jet is increased. However, the flow may be compressed so much that its pressure exceeds the background pressure again, after which the cycle of expansion and compression can start over again. The difference between jet and background pressure becomes smaller

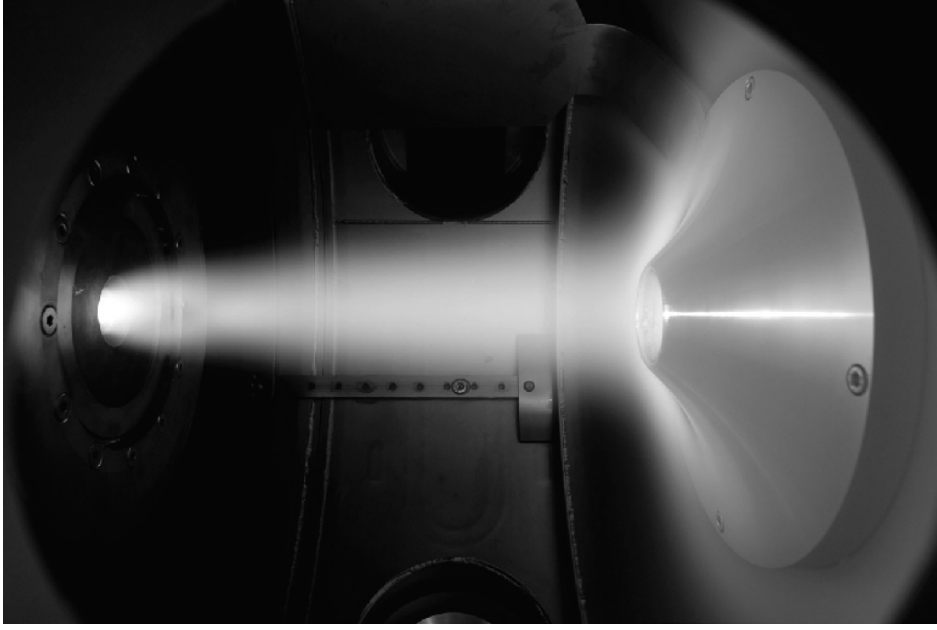


**Figure 7.1:** Argon plasma jet in Magnum-PSI. The background pressure is 30 Pa. At the left, a shockwave can be seen. The feature on the right is the skimmer, which limits the gas flow to the next chamber. The expansion can be seen as a dark region after the nozzle exit. The shock diamond shows up as a lighter region after the expansion.

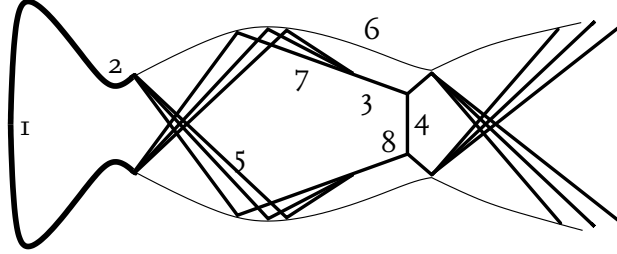


**Figure 7.2:** Shock wave structures in an underexpanded jet. (1: High pressure reservoir, 2: Nozzle exit, 3: Oblique shock waves, 4: Mach disk, 5: Expansion fan, 6: Free jet boundary, 7: Compression fan, 8: Shock triple point)

with each expansion-compression cycle. This damping is due to viscous dissipation, which occurs when the expansion fan reflects from the jet boundary.

According to Ashkenas [60], the position of the first shock is given by:

$$x_{shock} = 0.67d\sqrt{\frac{p_{st}}{p_{ch}}}, \quad (7.1)$$

where  $x_{shock}$  is the position of the shock measured from the exit of the arc,  $d$  is the diameter of the arc,  $p_{ch}$  is the chamber pressure and  $p_{st}$  is the stagnation pressure. Note that (7.1) is an empirical relation for isentropic flows. In plasmas, shock posi-

tions can shift with respect to isentropic gas flow due to viscosity, heat exchange and ionization [61]. Therefore, we can expect deviations from (7.1).

### 7.3 The SIMPLE algorithm

#### 7.3.1 Incompressible flows

To compute an incompressible flow field, the solution of both the momentum and continuity equation (2.9) and (2.17) has to be found. The difficulty in solving these two equations simultaneously is the fact that in the momentum equation the pressure gradient acts as a source term. This pressure is not known, because it is one of the parameters that must be computed. The solution to this problem is given by the continuity equation. Implicitly, the correct pressure is provided by the continuity equation: if the correct pressure is substituted in the momentum equation, the resulting velocity field should satisfy the continuity equation. Yet, the pressure does not occur in the continuity equation. The indirect information in the continuity equation must thus be converted into a direct algorithm for the calculation of the pressure to calculate the flow field.

The algorithm that is used for this in Plasimo is the SIMPLE algorithm, which stands for Semi Implicit Method for Pressure Linked Equations [22, 23]. There are a number of solution strategies which are closely related to the SIMPLE algorithm, amongst others SIMPLER, SIMPLEC and PISO [23]. Since these are all variations based on the same idea, and the SIMPLE algorithm is the algorithm actually used in Plasimo, the explanation in this chapter is restricted to the SIMPLE algorithm.

The explanation of the SIMPLE algorithm in this chapter will proceed along the same lines as in [22]. The algorithm starts with guessing a pressure  $p^*$ . This pressure can be put in the discretized momentum equations, after which the velocity field can be calculated. In general, the velocity field  $v^*$  calculated from this initial guess  $p^*$  will not satisfy the continuity equation. The next step in the SIMPLE algorithm is to find a correction  $p'$  to the guessed pressure  $p^*$ , such that the resulting velocity field will satisfy the continuity equation.

Assume that the correct pressure is given by:

$$p = p^* + p', \quad (7.2)$$

where  $p'$  is the pressure correction. Due to the pressure correction the velocities will also change:

$$u = u^* + u', \quad v = v^* + v', \quad w = w^* + w'. \quad (7.3)$$

The question is how to calculate the pressure correction  $p'$  and how to use this pressure correction to calculate the velocity corrections. The relation between the pressure and the velocity correction will follow from the discretized momentum equation, the pressure correction is calculated from the discretized continuity equation.

Plasimo uses the finite volume method for discretization. The SIMPLE algorithm is often used in combination with a staggered grid [22, 23], but Plasimo uses a colo-

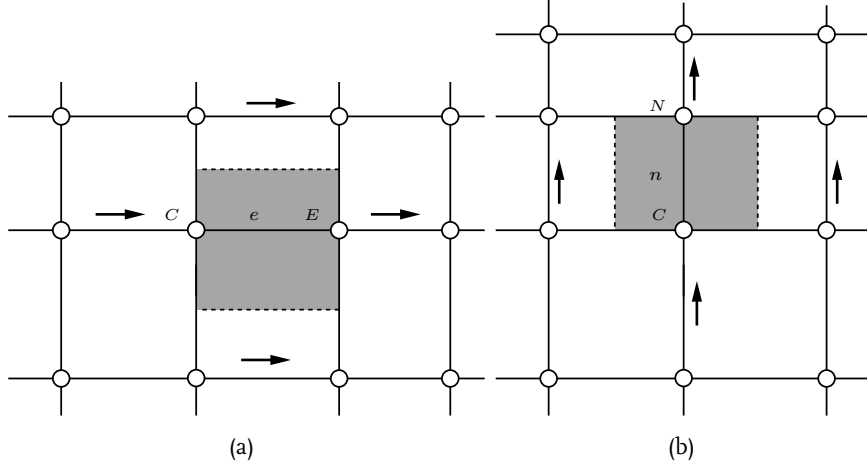


**Figure 7.3:** Staggered control volumes for the discretization of the momentum equation for deriving the discretized equations for  $p'$  and  $u'$ . Note that for calculation of  $v^*$  from  $p^*$  the momentum equation is discretized on a colocated grid. The control volume for discretization in the east-west direction is given by (a), (b) indicates the control volume for discretization in the north-south direction.

cated grid. The reason is that this is more convenient when orthocurvilinear coordinates are used as curvature terms do not need to be evaluated then. In a colocated grid, velocities are defined on the nodal points. However, for derivation of the pressure correction equation in Plasimo, the staggered grid of Patankar [22] is used. As a result, in the discretized pressure correction equation, terms containing the velocity  $v^*$  defined on the control volume faces occur. Since this velocity  $v^*$  is in Plasimo calculated on a colocated grid, a special interpolation scheme is needed. This interpolation scheme is discussed in [62] and [63]. In contrast to the calculation of  $v^*$  from  $p^*$  on a colocated grid, the response of  $u'$  on  $p'$  is determined using staggered control volumes. In Figure 7.3 these staggered control volumes can be seen.

In the following, it is assumed that the flow problem is two-dimensional, Cartesian and stationary. As motivated in Chapter 3, extension to higher dimensions and general ortho-curvilinear coordinates is relatively simple, therefore it will not be considered here. In a steady, quasi-neutral plasma, the momentum equations for the flow as given in Chapter 2 reduce to:

$$\nabla \cdot (\rho \vec{v} \vec{v}) = -\nabla p - \nabla \cdot \bar{\bar{\pi}} + \vec{j} \times \vec{B}, \quad (7.4)$$

with  $\rho$  the mass density,  $\vec{v}$  the velocity,  $p$  the pressure,  $\bar{\bar{\pi}}$  the viscous stress tensor,  $\vec{j}$  the current density and  $\vec{B}$  the magnetic field. Integrating equation (7.4) over the control volume gives the following result for the east-west direction:

$$a_e u_e = \sum a_{nb} u_{nb} + b_{ew} + (p_C - p_E) A_e, \quad (7.5)$$

where  $a_e = (\rho u)_e \Delta y$ ,  $A_e = \Delta y$ , the subscript  $nb$  denotes the neighbors as indicated with arrows in Figure 7.3 and  $b_{ew}$  contains the forces in the east-west direction that

are not related to the pressure gradient. In this discretization the mass density is assumed to be constant. When dealing with a compressible flow the effect of the mass density must be included. How this is done will be discussed in the next section. The velocity can be computed from the momentum equations if the pressure field is given or estimated. When  $p = p^*$  is used as the guess for the pressure, the resulting velocity  $u^*$  will be given by:

$$a_e u_e^* = \sum a_{nb} u_{nb}^* + b_{ew} + (p_C^* - p_E^*) A_e. \quad (7.6)$$

Unless  $p^*$  was the correct pressure, the resulting velocity field  $u^*$  will not satisfy the continuity equation. By subtracting (7.6) from (7.5), the following is obtained:

$$a_e u_e' = \sum a_{nb} u_{nb}' + (p_C' - p_E') A_e. \quad (7.7)$$

As is pointed out in [22], it is possible to leave out the term  $\sum a_{nb} u_{nb}'$ , since the converged solution will have  $u' = 0$ . By dropping this term the algorithm becomes semi-implicit, hence the name SIMPLE. The response of the velocity correction to the pressure correction becomes:

$$u_e' = \frac{A_e}{a_e} (p_C' - p_E') = d_e (p_C' - p_E'). \quad (7.8)$$

This equation shows how the guessed velocity is to be corrected in response to the pressure correction. The other velocity components are obtained likewise. Now the pressure correction has to be found, such that the resulting velocity field will satisfy the continuity equation. This is done by discretizing the mass continuity equation. Integration over the control volume in Figure 7.4, leads to the following expression:

$$[(\rho u)_e - (\rho u)_w] \Delta y + [(\rho v)_n - (\rho v)_s] \Delta x = 0. \quad (7.9)$$

Substitution of the relations between the velocity and pressure correction:

$$\begin{aligned} u_e &= u_e^* + d_e (p_C' - p_E'), \\ u_w &= u_w^* + d_w (p_W' - p_C'), \\ v_n &= v_n^* + d_n (p_C' - p_N'), \\ v_s &= v_s^* + d_s (p_S' - p_C'), \end{aligned}$$

gives the discrete equation for  $p'$ :

$$a_C p_C' = a_E p_E' + a_W p_W' + a_N p_N' + a_S p_S' + b, \quad (7.10)$$

where  $a_C = a_E + a_W + a_N + a_S$ , with  $a_E = \rho_e d_e \Delta y$  (other directions are similar) and  $b = [(\rho u^*)_w - (\rho u^*)_e] \Delta y + [(\rho v^*)_s - (\rho v^*)_n] \Delta x$ .

For the calculation of the discretization coefficients the mass density thus has to be known on the control volume boundaries. To calculate the mass density on these boundaries, an interpolation scheme is needed. From equation (7.10), it can be seen

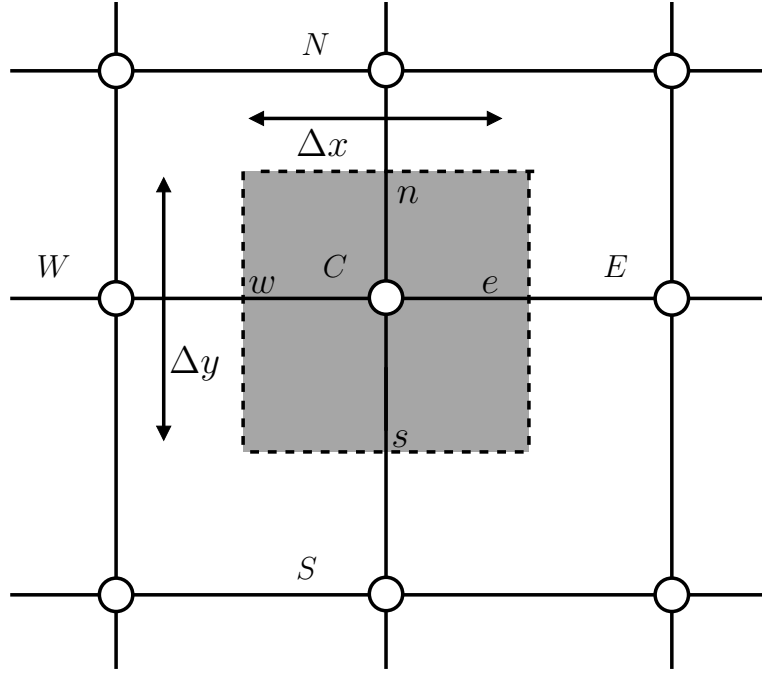


Figure 7.4: Control volume for discretization of the continuity equation.

that  $b$ , which is the mismatch from the continuity equation, acts as a source term. If the starred velocities  $v^*$  fulfill continuity, the  $b$  term in the right hand side of (7.10) will be zero and no pressure correction is needed: the solution of the flow problem has converged. The SIMPLE solution algorithm for incompressible flows can now be summarized as follows:

- Guess the pressure field  $p^*$ .
- Solve the momentum equations to obtain  $u^*, v^*$ .
- Solve the pressure correction equation (7.10).
- Calculate  $p$  by adding the pressure correction:  $p = p^* + \alpha p'$ .
- Calculate the velocities with the velocity correction formulas (7.8).
- Solve the other equations that depend on the flow (temperature, mixture, transport coefficients).
- Use the corrected pressure  $p$  as the new guess  $p^*$  and repeat the procedure until convergence.

As can be seen, only part of the pressure correction  $p'$  is added to  $p^*$ . This under-relaxation  $\alpha$  is applied to avoid divergence as is pointed out in [22]. In the calculation of  $u^*$  and  $v^*$  from the discretized momentum balance some under-relaxation can

also be applied. The solution is considered converged if the residual of both the velocity and the pressure correction equation are below the specified tolerance. The residual of the pressure correction equation is defined as the scaled deviation from mass continuity. The residual of the velocity is defined as the root mean square of the residual of the velocity components. The residual of the components are defined similarly to equation (3.46) but scaled with the mean value of the magnitude of the velocity instead of the velocity at each grid point. The following section will discuss the modifications in the solution procedure when the flow is compressible.

### 7.3.2 Compressible flows

The procedure described in Section 7.3 is used when the flow is incompressible: a change in pressure does not effect the mass density. In compressible flows a change in pressure will effect the mass density. Karki corrections [64] take into account the influence of pressure on the mass density. Besides the velocity, the mass density is now also corrected after the pressure correction is calculated. Note that the calculation of the pressure correction also changes due to the contribution of the mass density.

For calculation of the pressure correction equation in a compressible flow, the mass flux is approximated by [22]:

$$\rho u = (\rho^* + \rho') (u^* + u') = \rho^* u^* + \rho' u^* + \rho^* u', \quad (7.11)$$

where the second order term  $\rho' u'$  has been neglected [22]. Furthermore, the following relation between the pressure and the mass density correction is assumed:

$$\rho' = K p'. \quad (7.12)$$

In principle, the Karki coefficient  $K$  can be chosen freely, since the particular form of the Karki correction does not influence the final solution, but it influences the convergence path towards the solution. A bad choice for the Karki correction can therefore lead to divergence. It is therefore best to base  $K$  on an approximate equation of state. In Plasimo  $K = \rho/p$  is used, which corresponds with  $K = \left. \frac{\partial \rho}{\partial p} \right|_T$  according to the ideal gas law. The discretization of the continuity equation is now given by:

$$\begin{aligned} & [(\rho^* u^*)_e - (\rho^* u^*)_w] \Delta y + [(\rho^* v^*)_n - (\rho^* v^*)_s] \Delta x + \\ & [(\rho^* u')_e - (\rho^* u')_w] \Delta y + [(\rho^* v')_n - (\rho^* v')_s] \Delta x + \\ & [(\rho' u^*)_e - (\rho' u^*)_w] \Delta y + [(\rho' v^*)_n - (\rho' v^*)_s] \Delta x = 0 \end{aligned} \quad (7.13)$$

Substituting relations (7.12) and (7.8) gives:

$$\begin{aligned} & [(\rho^* u^*)_e - (\rho^* u^*)_w] \Delta y + [(\rho^* v^*)_n - (\rho^* v^*)_s] \Delta x + \\ & [(\rho^* d_e(p'_C - p'_E))_e - (\rho^* d_w(p'_W - p'_C))_w] \Delta y + \\ & [(\rho^* d_n(p'_C - p'_N))_n - (\rho^* d_s(p'_S - p'_C))_s] \Delta x + \\ & [(K_e(p'_C - p'_E)u^*)_e - (K_w(p'_W - p'_C)u^*)_w] \Delta y + \\ & [(K_n(p'_C - p'_N)v^*)_n - (K_s(p'_S - p'_C)v^*)_s] \Delta x = 0. \end{aligned} \quad (7.14)$$



This can be rearranged to the same form as equation (7.10), where the discretization coefficients are given by

$$a_C = a_E + a_W + a_N + a_S, \quad (7.15)$$

with

$$a_E = (\rho_e^* d_e + K_e u^*) \Delta y. \quad (7.16)$$

The coefficients  $a_W$ ,  $a_N$ ,  $a_S$  are calculated in a similar way. As can be seen, Karki corrections influence the mass density. But Karki corrections also change the equation from which the pressure correction is calculated. In principle, in a compressible flow/plasma model the density can also be calculated from an equation of state. However, when the flow is strongly compressible Karki corrections may be necessary [22].

**Underrelaxation** As explained in the previous section, the momentum equation from which  $v^*$  is determined can be under-relaxed for stability reasons. The pressure correction may be under-relaxed as well, by adding only a part of the pressure correction  $p'$  to the pressure. In Plasimo, one can choose to under-relax the Karki correction with an under-relaxation factor  $\alpha$ :

$$\rho' = \alpha K p' \quad u' = dp'. \quad (7.17)$$

This under-relaxation has no consequences for mass continuity, but makes the mass density correction less important than the velocity correction.

## 7.4 Numerical model of the source and the expansion

To describe the multicomponent plasma, the fluid equations as given in Section 2.3 are solved. In the simulation it is assumed that the argon plasma is composed only of argon atoms, ions and electrons. Production and destruction of molecular ions, doubly charged ions and different excited levels of the argon neutrals are not taken into account. The production and destruction of argon ions by direct ionization and three particle recombination,  $Ar + e \rightleftharpoons Ar^+ + e + e$ , and stepwise ionization and recombination via the first excited state  $Ar^*$ ,  $Ar + e \rightleftharpoons Ar^* + e \rightleftharpoons Ar^+ + e + e$ , is taken into account. The effect of stepwise ionization is taken into account via an effective rate coefficient, where excitation of  $Ar^*$  is taken as the rate determining step. The species  $Ar^*$  itself is not included in the model. The forward rate coefficient  $k_f$  for both reactions is approximated by a modified Arrhenius expression:

$$k_f = c \left( \frac{T_e}{K} \right)^q \exp \left( \frac{-E}{k_B T_e} \right), \quad (7.18)$$

where  $c$  is the rate constant,  $T_e$  the electron temperature and  $E$  the reaction energy. For the direct ionization reaction,  $c$  was obtained by fitting the cross-section data from [65], which resulted in  $c = 2.8 \times 10^{-16} \text{ m}^3/\text{s}$ ,  $q = 0.5$  and  $E = 15.8 \text{ eV}$ . The stepwise

ionization reaction is described in [66]:  $c = 6.8 \times 10^{-17} \text{ m}^3/\text{s}$ ,  $q = 0.5$  and  $E$  is 12.1 eV. The backward reaction rates of both the direct and stepwise process are obtained via detailed balancing.

To study the influence of the nozzle on the argon jet, simulations are performed for different cylindrical geometries on a 218 by 318 grid. The different geometries are schematically depicted in Figure 7.5. The small cylinder on the left represents the arc

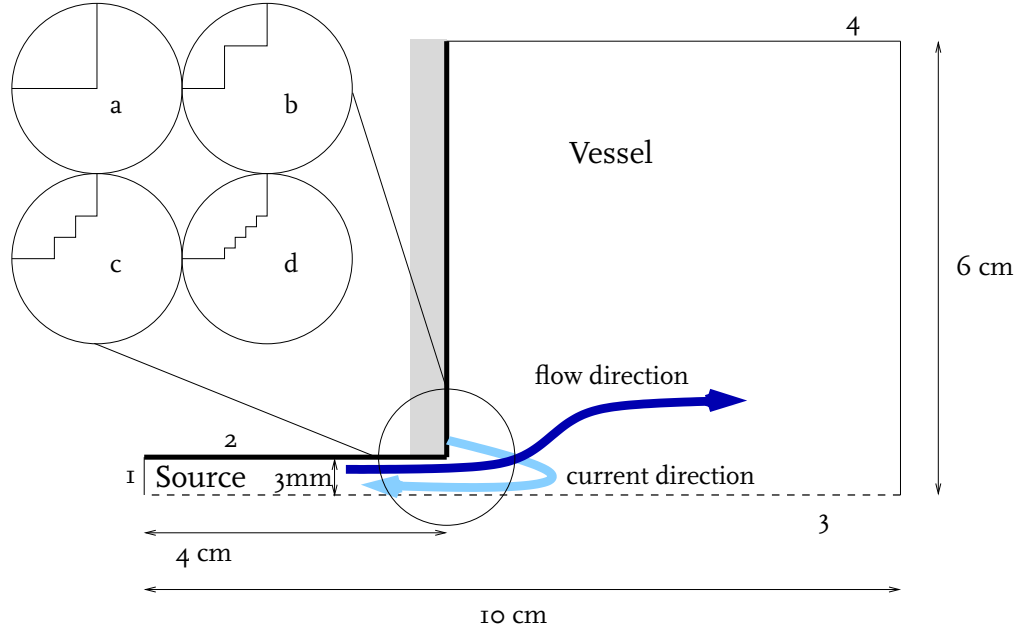


**Figure 7.5:** The model geometry for different nozzle layouts. The gray shaded area indicates where the vessel is grounded. (1: Inlet, 2: solid wall, 3: symmetry axis, 4: outlet, a: no nozzle, b: one step nozzle, c: two step nozzle, d: four step nozzle).

which is 4 cm long and 6 mm in diameter. Grid stretching [21] is applied to increase the coordinate line densities at the inlet, the outlet and the wall of the arc to resolve sharp gradients and shockwaves. Note that the stretching at the wall of the arc will result in grid refinement in the expansion zone as well.

At the walls no-slip boundary conditions are used for both velocity components. At the inlet of the arc and the outlet of the vessel the pressure is specified, and homogeneous Neumann conditions are applied for both velocity components. At the symmetry axis, homogeneous Neumann conditions are applied for the pressure and the axial velocity, while the radial velocity is set to zero.

For the heavy particles, the temperature is fixed to 500 K at the inlet of the arc and the walls. On the symmetry axis and the outlet, homogeneous Neumann conditions are applied. For the electron temperature homogeneous Neumann conditions are used at all boundaries, since the electrons do not exchange heat efficiently with the wall due to their small mass.

At the inlet of the arc, the electric current  $I$  is specified. This translates to a

Neumann condition for the potential as follows:

$$I = - \int \sigma \frac{\partial}{\partial z} \phi dA \quad \Rightarrow \quad \frac{\partial}{\partial z} \phi = - \frac{I}{\int \sigma dA}, \quad (7.19)$$

where it is assumed that the axial electric field is uniform over the inlet of the arc. The anode is grounded. All other boundaries have homogeneous Neumann conditions for the potential.

## 7.5 Numerical results

In this section, plasma creation and expansion is studied first in a geometry without nozzle, thus simulating a free expansion. The inlet pressure is 11000 Pa, the outlet pressure 150 Pa, the current 100 A. Then the effect of varying chamber pressure on the shock position is studied. Finally, the effect of the nozzle geometry on the expansion is presented.

### 7.5.1 The free expansion

In Figure 7.6, the results of the simulation with an inlet pressure of 11000 Pa, a chamber pressure of 150 Pa and a current of 100 A in a geometry without nozzle are given. Inside the arc, the flow accelerates to a Mach number of 1. At the transition from arc to vessel the plasma expands and accelerates to supersonic velocities. After the shock the flow becomes subsonic again. The Mach disk can clearly be distinguished. Note that the condition of  $M=1$  at the arc exit is not *imposed* on the model, it *follows* from the model.

In the heavy particle temperature the effect of the expansion can be seen as a sharp drop in the temperature. After the shock the temperature rises strongly again because of compression and viscous dissipation. Note that overall, the calculated temperatures are higher than expected. The reason is that the plasma is fully ionized at  $z \approx 1.2$  cm. Since the effect of doubly charged ions is not taken into account in the model, energy can not be used for ionization anymore and the temperature rises.

### 7.5.2 Shock position

When changing the background pressure, we expect that for lower background pressures, the shock location is positioned further away from the arc exit. From Figure 7.7 we can see that this is indeed the case in the simulation. The stagnation pressure found in the simulation is approximately 2890 Pa. Calculation of the shockwave position with equation (7.1) gives  $x_{shock} \approx 18$  mm for 150 Pa and  $x_{shock} \approx 12$  mm for 300 Pa. From Figure 7.7 it can be seen that this is in good agreement with the position of the shock from the simulations.

Also for the temperature, the effect of the pressure on the shock can be seen. We can also see that at 150 Pa, where the shock is stronger, the cooling of the expansion and the heating by the shock are larger. Furthermore, the difference between the

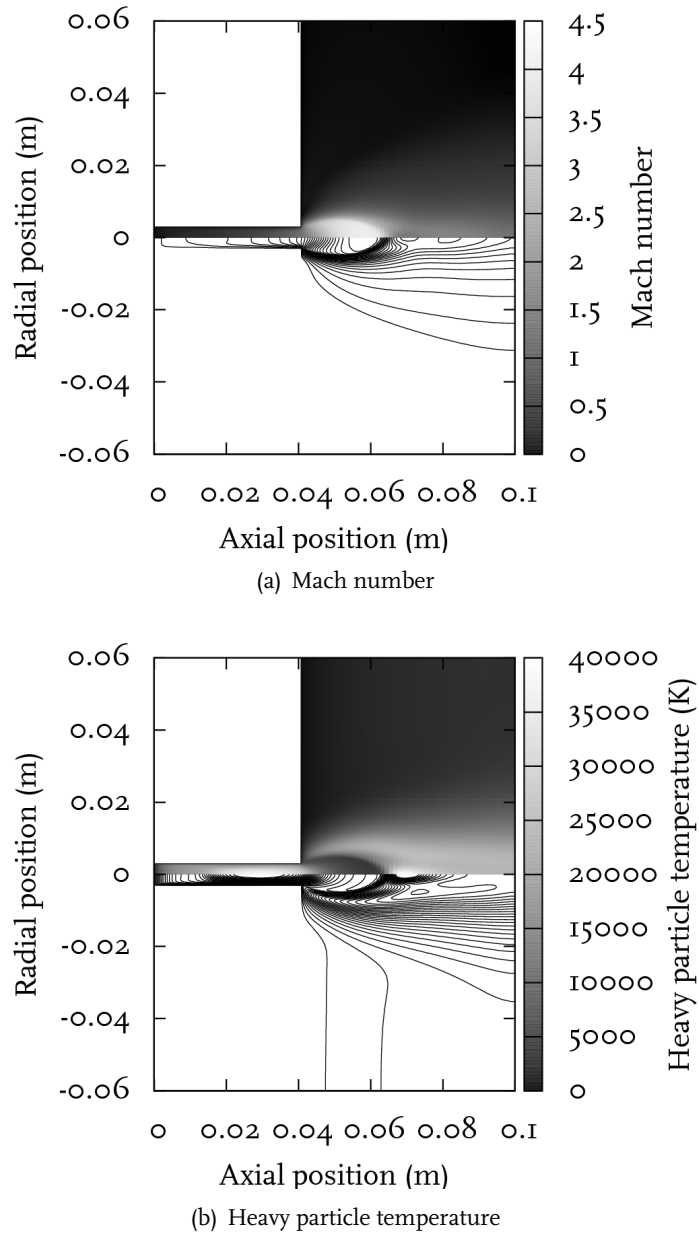
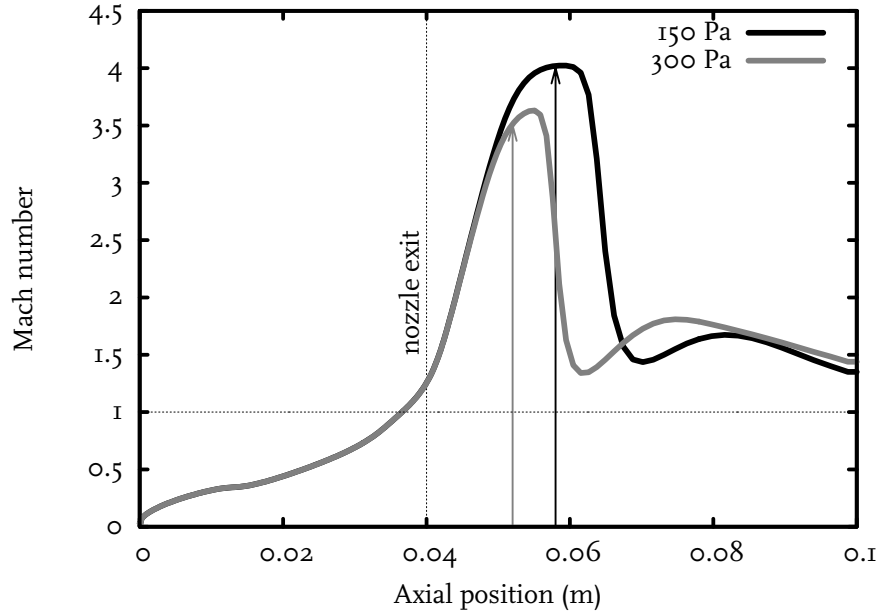
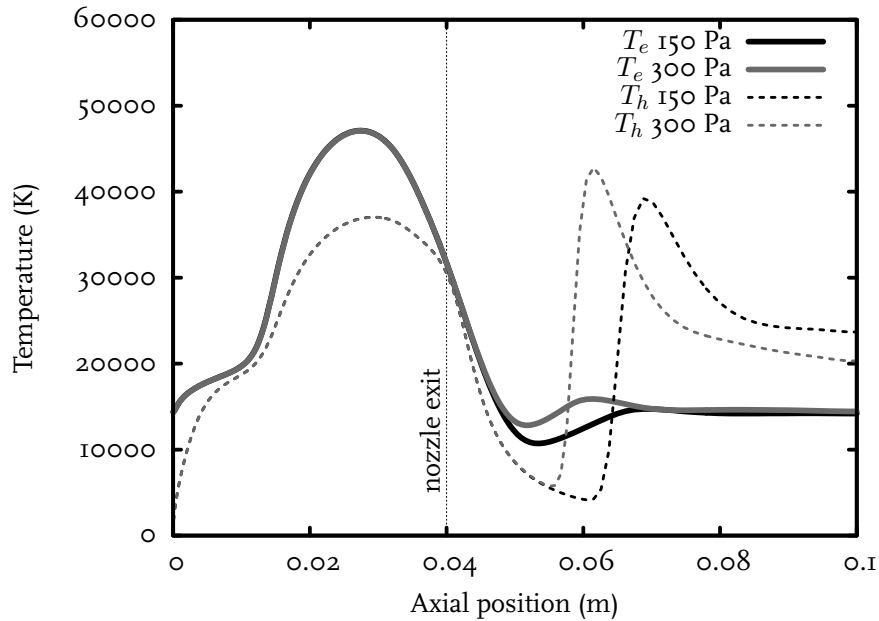


**Figure 7.6:** The free expansion without nozzle. The top part of the plots shows the results with a gray map, the bottom part shows the mirrored (negative radial positions) results as a contour plot.

electron and heavy particle temperature is clearly visible: the plasma is in non-LTE. Upstream of  $M=1$  there are no differences between the two simulations, as should be the case because of choking of the flow. Decreasing the downstream pressure will not result in a higher mass flux through the source.



(a)



(b)

**Figure 7.7:** The Mach number and the electron and heavy particle temperature at the symmetry axis for two different background pressures. The shock position moves downstream with decreasing background pressure. The shock positions according to equation (7.1) are indicated by arrows.

### 7.5.3 Influence of nozzle geometry

In Figure 7.8, the Mach number in the different nozzle geometries can be seen. It is clear that the nozzle has a very large effect on the flow field. Whereas in the free expansion we can clearly see the features of the underexpanded jet, the results are totally different when a nozzle is present. The shock wave forming in the nozzle is

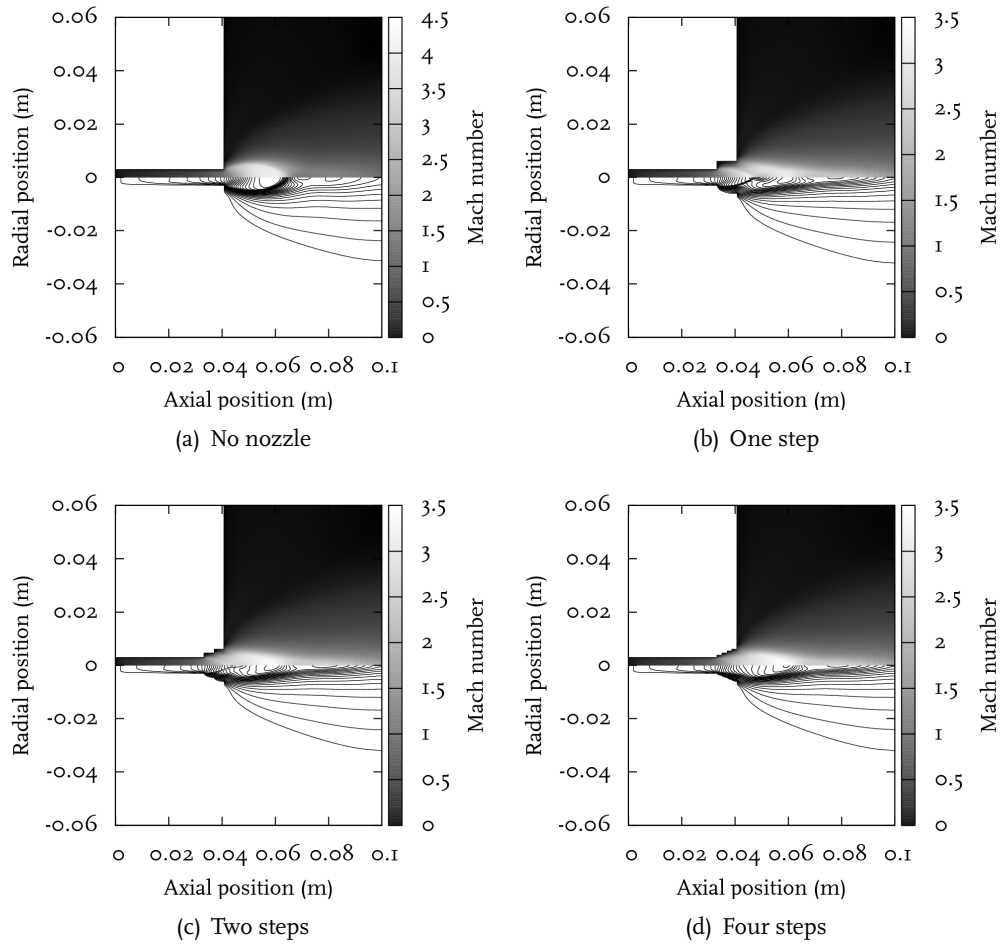


**Figure 7.8:** The Mach number for different nozzle geometries. The shock wave is reflected from the nozzle wall, resulting in a more confined flow field.

reflected from the nozzle wall, resulting in a more confined flow field. Similar results were found in [5] using gas dynamics simulations. For the two and four step nozzle, the flow field is also more confined, but sharp reflections on the nozzle wall are not visible anymore. Note that the nozzles with two and four steps give more or less the same results. This indicates that the solution converges rapidly towards the case where the nozzle consists of infinitely many steps.

This effect can also be seen in the heavy particle temperature and electron density in Figures 7.9 and 7.10. Both the temperature and electron density become more confined to the center of the plasma jet when a nozzle is present. Again, we see rapid convergence to a fixed solution when doubling the number of steps in the nozzle.

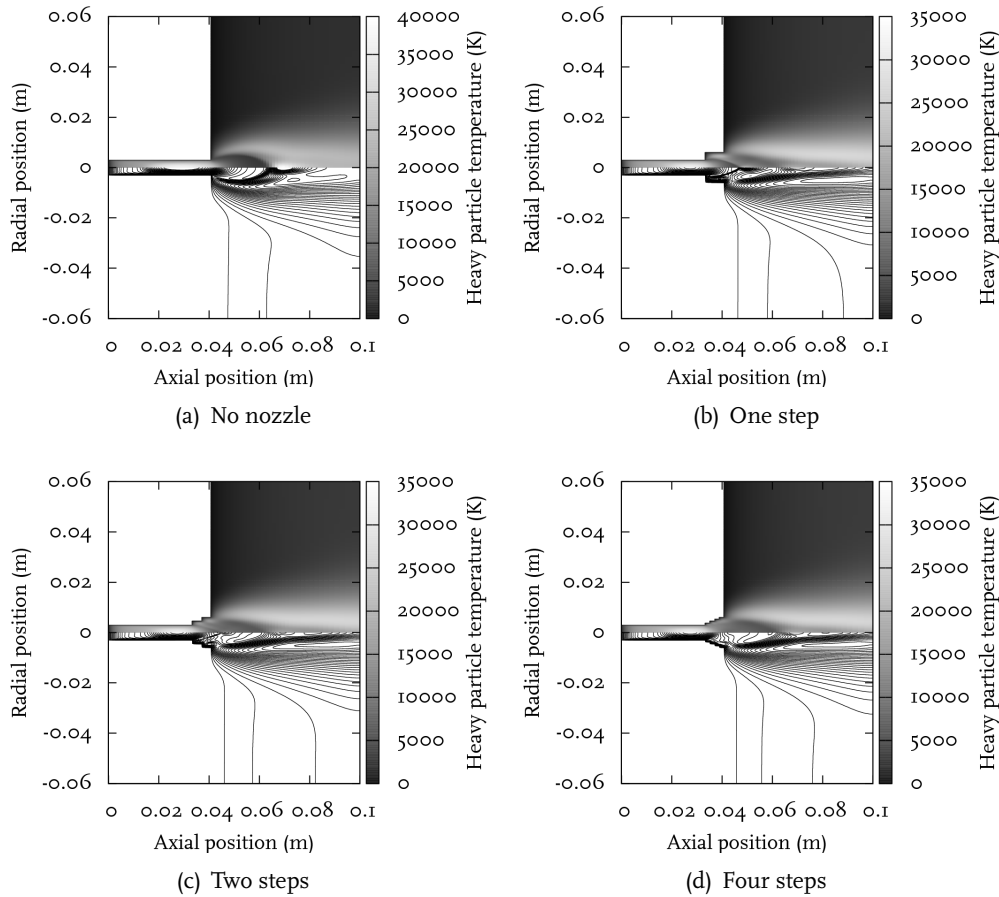
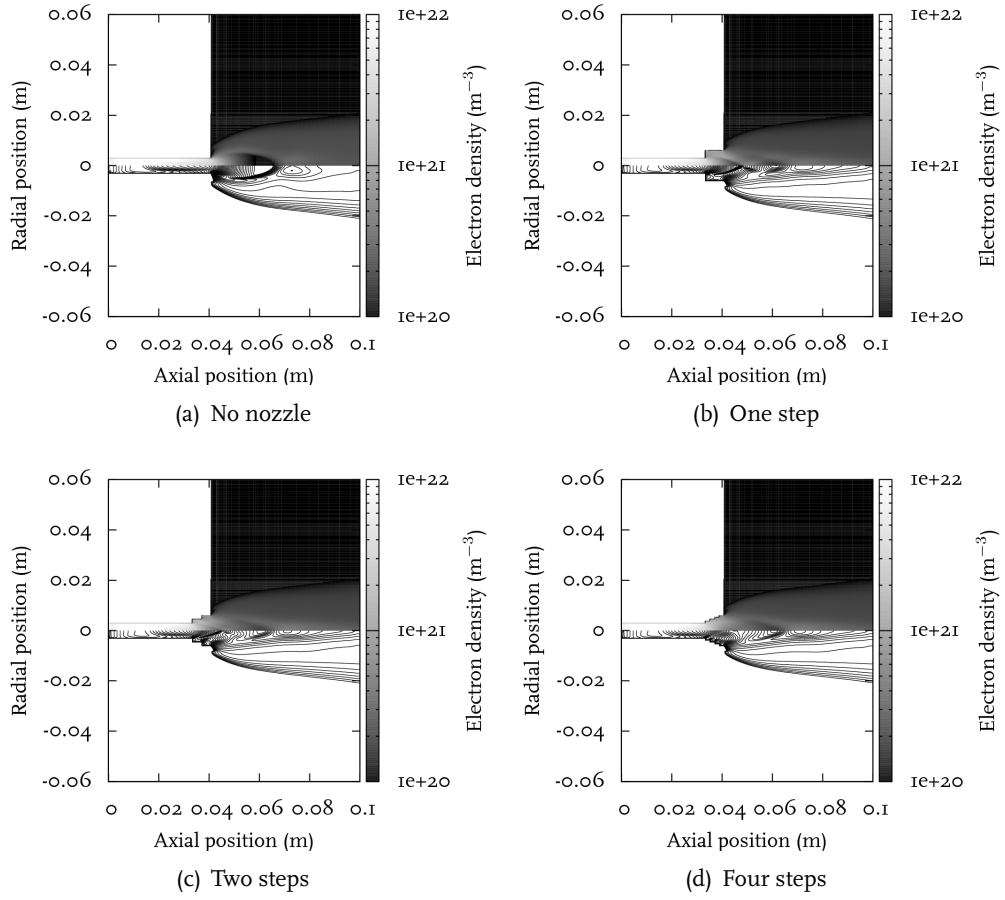


Figure 7.9: The heavy particle temperature for different nozzle geometries.

## 7.6 Conclusions

In this chapter, the feasibility of an integral simulation of both plasma creation in the arc and the consecutive expansion was shown. It was shown that Plasimo can handle the transition from a subsonic to a supersonic flow field. Expected physical behavior like the  $M=1$  condition at the exit of the arc and choking of the flow follow automatically from the model. The model can therefore be used when it is not known *a priori* whether the flow is subsonic or transonic. Another advantage of the integral approach is that the domain of the model does not need to be split on the interface between the arc and the chamber. This is of particular interest because shock waves



**Figure 7.10:** The electron density for different nozzle geometries.

can be present in this interface region. Splitting can therefore easily lead to inconsistencies. It also facilitates studying the effect of the nozzle geometry and anode location.

In the expansion the shockwave position was compared with the model of Ashkenas. Predicted and simulated positions were in good agreement. Small deviations can be due to the fact that the plasma in the simulation is heated by Ohmic dissipation during its expansion.

Finally, the influence of nozzle geometry was studied. It was shown that nozzle reflections lead to a more confined beam. For an increasing number of nozzle steps, the solution converged to a 'fixed' solution.





## Chapter 8

# Effects of magnetization on the expanding argon jet

### 8.1 Introduction

An important operational parameter in Magnum-PSI is the magnetic field. The question is how this field will influence the efficiency of the plasma production and the transport of the plasma beam to the target. Several numerical simulations have been performed to obtain insight in these questions. The effect of the magnetic field on the plasma production in the source was, for example, studied with a non-LTE model by Ahmad [67] for an argon / hydrogen plasma. In [67], magnetic confinement is described by reducing the diffusion by a factor  $1 + H^2$ , with  $H$  the Hall parameter. However, the influence of magnetic confinement on heat conduction or electrical conductivity is not taken into account. Furthermore, the magnetic field is ignored in the flow and electromagnetic calculation. The effect of the magnetic field on the flow and electromagnetic field is taken into account by Cinalli [5] by MHD calculations. However, with an MHD approach plasma production can not be studied and no distinction between the electron and heavy particle temperature can be made since the plasma is treated as a single fluid.

In this chapter we want to present a more complete approach, where the diffusion, electromagnetic and flow calculation are self-consistently coupled via the current density in a non-LTE model. To this end, we extend the non-magnetized argon model from Chapter 7 with the magnetic field in Section 8.2. We will demonstrate how the diffusion velocities, electromagnetic field and flow field become coupled when the plasma gets magnetized. We will then examine the influence of the axial magnetic field on the flow pattern and electromagnetic power incoupling. Numerical results are given in Section 8.3. Finally, Section 8.4 presents the conclusions.

### 8.2 Numerical model for the magnetized expansion

In order to take into account the effect of magnetization, the model discussed in Chapter 7 is revised. This section will outline these revisions. Unless otherwise

stated, the model is the same as in Chapter 7. The major difference is in the multi-component diffusion calculation, where we now use the multicomponent diffusion theory as described in Chapter 6. In the species mass balances, only the ambipolar diffusion matrix from Chapter 6 is taken into account. The drift terms are neglected for numerical stability. As a result, the mean flow velocity is the bulk velocity  $\vec{v}$  for all species. However, in the electromagnetic and flow calculation all terms are taken into account. In argon, this is a reasonable assumption since convection is dominant over diffusion.

### 8.2.1 Anisotropic transport coefficients

Due to application of the magnetic field, the transport coefficients become anisotropic. Diffusion, conductivity and heat conduction will be reduced in the direction perpendicular to the magnetic field lines. The resulting confined plasma jet will be quite different from the plasma jet presented in Chapter 7. Especially the anisotropy in the electrical conductivity will cause large differences in power input compared to the unmagnetized case.

In contrast to Chapter 7, where the mixture rules of Mitchner and Kruger [14] were used for the heavy particle thermal conductivity and the Frost mixture rules [17] for the electron thermal conductivity, thermal conductivities are calculated in a different way in this chapter. Simple expressions based on random walk estimates are used, as described in [18]. For the typical step size, the mean free path is used parallel to the magnetic field, while perpendicular to the magnetic field the Larmor radius is used. Note that only classical transport is taken into account, anomalous transport due to microturbulence is ignored.

### 8.2.2 Flow field

In simulations of magnetized plasmas, the flow calculation is coupled to the multi-component diffusion calculation. The multi-component diffusion calculation provides the Lorentz force  $\vec{j} \times \vec{B}$  acting on the flow. The flow calculation in turn provides the bulk velocity, which is one of the driving forces in the diffusion calculation. By taking the inner product of equation (6.21) with  $\mathbf{z}$ , it can be seen that the radial and azimuthal current are given by:

$$\begin{aligned} j^\perp &= \sigma^\perp E^\perp + \left( \sigma^\perp v^\odot + \sigma^\odot v^\perp \right) B, \\ j^\odot &= -\langle \mathbf{z}, \mathbf{D}^\odot \left( \mathbf{I} - \frac{\mathbf{z} \otimes \mathbf{D}^\perp \mathbf{z}}{\langle \mathbf{z}, \mathbf{D}^\perp \mathbf{z} \rangle} \right) \partial_\perp \mathbf{x} \rangle + \sigma^\odot E^\perp + \left( \sigma^\odot v^\odot - \sigma^\perp v^\perp \right) B. \end{aligned} \quad (8.1)$$

Taking the cross product with the magnetic field gives the Lorentz force in the radial and azimuthal direction:

$$\begin{aligned} F^\perp &= j^\odot B, \\ F^\odot &= -j^\perp B. \end{aligned} \quad (8.2)$$

Due to the azimuthal Lorentz force the plasma jet will start to rotate. This rotation will be most pronounced in the regions where there is a radial component of the electric field, i.e.,  $E^\perp \neq 0$ . The radial Lorentz force points inwards since  $j^\odot < 0$  and limits the expansion of the plasma beam. As a result the jet will be more confined.

The Lorentz force  $\vec{j} \times \vec{B}$  is added as a force to the Navier Stokes equations. Due to the azimuthal Lorentz force, an azimuthal component will appear in the velocity field. Note that this is not in contradiction with our 2D model with axial symmetry, since the azimuthal velocity does not depend on the azimuthal coordinate. At the inlet, the symmetry axis and solid walls, the azimuthal velocity is set to 0. At all other boundaries, homogeneous Neumann conditions are used.

To get an idea of the importance of the Lorentz force, we can calculate the Hartmann and Stuart number. The Hartmann number  $Ha$  gives the ratio of the Lorentz force to the viscous force and can be written as:

$$Ha = BL\sqrt{\frac{\sigma}{\mu}}, \quad (8.3)$$

where  $B$  is the magnitude of the magnetic field,  $L$  the typical length scale,  $\sigma$  the conductivity and  $\mu$  the dynamic viscosity. In the expansion of Magnum-PSI typical values are  $\sigma = 10^4$  S/m,  $\mu = 10^{-6}$  Pa s,  $B = 1$  T,  $L = 10^{-2}$  m. The Hartmann number then is  $Ha = 10^3$ , which means that the Lorentz force is far more important than viscous forces. The ratio between the Lorentz force term and inertia is given by the interaction parameter or Stuart number:

$$N = \frac{\sigma B^2 L}{\rho U}, \quad (8.4)$$

where  $U$  is a characteristic velocity and  $\rho$  the mass density. Inserting the same values as before and  $\rho = 10^{-5}$  kg/m<sup>3</sup>,  $U = 10^3$  m/s, gives  $N = 10^3$ . We can thus expect that in the expansion, the flow field is dominated by the Lorentz force. The Reynolds number  $Re$ , giving the ratio of inertial forces to viscous forces, is related to the Hartmann and the Stuart number via:

$$Re = \frac{Ha^2}{N}. \quad (8.5)$$

The present values for  $Ha$  and  $N$  give  $Re = 10^3$ . Turbulence is ignored in the flow calculation since the plasma jet is expected to remain laminar at this Reynolds number. A possible onset of turbulence at the transition from the arc to the chamber is not taken into account.

### 8.2.3 Electromagnetic field

The multi-component diffusion calculation is also coupled to the electromagnetic calculation via the Hall current. In the previous chapter, the electrostatic potential  $\phi$  was calculated from:

$$\nabla \cdot (\sigma \nabla \phi) = 0. \quad (8.6)$$

Since the total current now also includes the Hall current  $\vec{j}_{Hall}$ , and the conductivity becomes anisotropic this equation becomes:

$$\nabla \cdot (\bar{\sigma} \nabla \phi) = -\nabla \cdot \vec{j}_{Hall}, \quad (8.7)$$

with  $\bar{\sigma}$  the anisotropic conductivity tensor. As a result of the inclusion of the Hall current the Ohmic dissipation density  $\vec{j} \cdot \vec{E}$  changes as well.

The work per unit of volume by the external electromagnetic fields  $\vec{E}$  and  $\vec{B}$  on charged particles (Ohmic dissipation) is given by:

$$Q_{ohm} = \sum_i \vec{F}_i \cdot \vec{u}_i, \quad (8.8)$$

with  $\vec{F}_i$  the electromagnetic force on species  $i$  and  $\vec{u}_i$  the total velocity of species  $i$ . Specifying the force  $\vec{F}_i$  and splitting the velocity in a bulk velocity  $\vec{v}$  and diffusion velocity  $\vec{v}_i$ , we get:

$$Q_{ohm} = \sum_i n_i q_i \left( \vec{E} + (\vec{v} + \vec{v}_i) \times \vec{B} \right) \cdot (\vec{v} + \vec{v}_i). \quad (8.9)$$

Splitting in the components along  $\parallel$ , across  $\perp$  and around  $\odot$  the field lines gives:

$$\begin{aligned} Q_{ohm} &= \sum_i n_i q_i \left( E^{\parallel} (v^{\parallel} + v_i^{\parallel}) + (E^{\perp} + v^{\odot} + v_i^{\odot}) (v^{\perp} + v_i^{\perp}) \right. \\ &\quad \left. - (v^{\perp} + v_i^{\perp}) (v^{\odot} + v_i^{\odot}) \right) \\ &= j^{\parallel} E^{\parallel} + j^{\perp} E^{\perp}. \end{aligned} \quad (8.10)$$

The magnetic field does no work since the Lorentz force is perpendicular to the velocity. The term  $Q_{ohm}$  is the Ohmic dissipation and represents the conversion from electromagnetic energy into kinetic energy. This kinetic energy consists of both thermal and mechanical energy.

Let us now specify the current densities:

$$j^{\parallel} = \sigma_{\parallel} E^{\parallel}, \quad (8.11)$$

$$j^{\perp} = \sigma_{\perp} E^{\perp} + \sigma_{\perp} v^{\odot} B + \sigma_{\odot} v^{\perp} B. \quad (8.12)$$

If the above expressions are substituted in equation (8.10), the following expression for the Ohmic dissipation is obtained:

$$Q_{ohm} = \sigma_{\parallel} E^{\parallel 2} + \sigma_{\perp} E^{\perp 2} + \sigma_{\perp} v^{\odot} B E^{\perp} + \sigma_{\odot} v^{\perp} B E^{\perp}. \quad (8.13)$$

Besides the usual contribution  $\sigma_{\parallel} E^{\parallel 2} + \sigma_{\perp} E^{\perp 2}$  for non-magnetized plasmas, there are two additional terms due to the bulk motion in the magnetic field. Since  $v^{\odot}$  and  $v^{\perp}$  are positive, while  $E^{\perp}$  points in the negative radial direction, the terms  $\sigma_{\perp} v^{\odot} B E^{\perp} + \sigma_{\odot} v^{\perp} B E^{\perp}$  give a negative contribution to the Ohmic dissipation. When  $\vec{j} \cdot \vec{E} > 0$ , electromagnetic energy is converted into kinetic energy. When  $\vec{j} \cdot \vec{E} < 0$ , kinetic energy is converted into electromagnetic energy.

### 8.3 Results

In this section, the results for an expanding argon jet for different magnetic field strengths are presented. As in Chapter 7, the inlet pressure is 11000 Pa, the background pressure 150 Pa, resulting in a gas flow rate of approximately 1.9 slm. The applied current is 100 A. Simulations are performed on the grid with a one-step nozzle as presented in Chapter 7. The discharge channel has a diameter of 6 mm and is 3.5 cm long.

#### 8.3.1 Flow field

As discussed in the previous section, we expect from the Hartmann and Stuart number that the magnetic field will have a large impact on the flow field. In Figure 8.1,

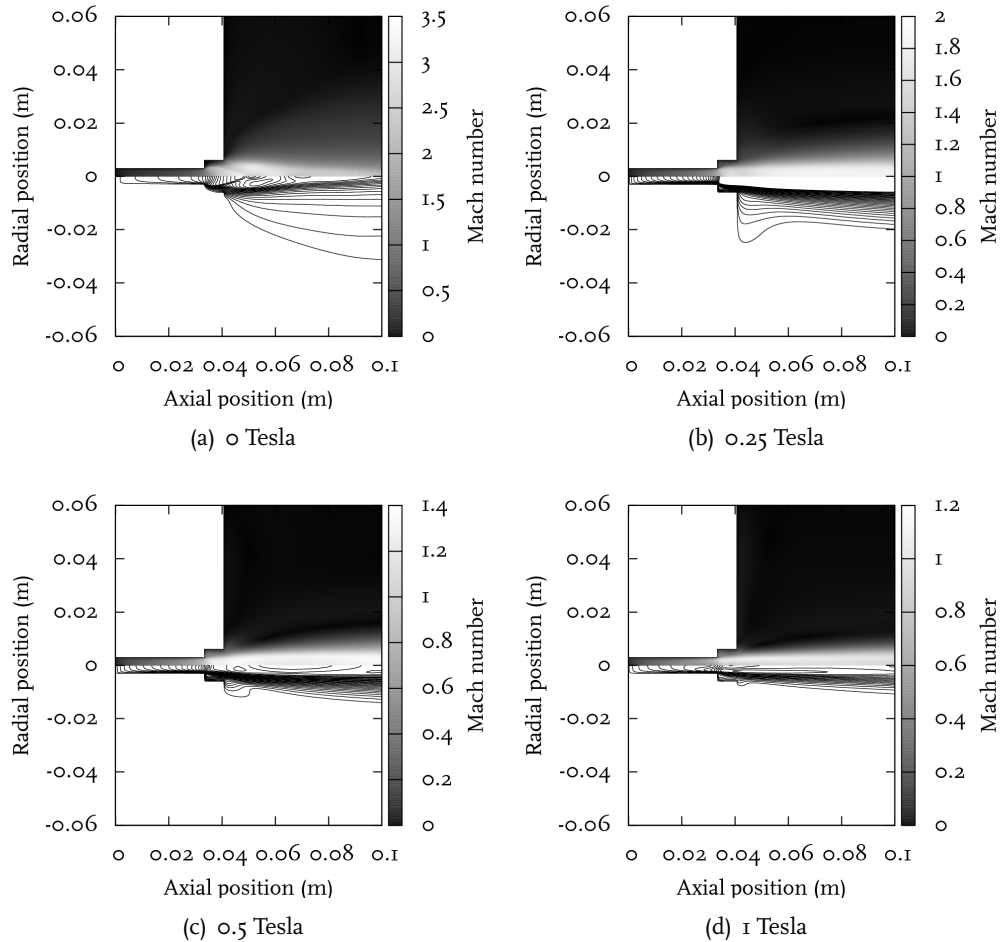


**Figure 8.1:** Mach number for different magnetic field strengths. With increasing magnetic field the plasma jet becomes narrower and more confined.

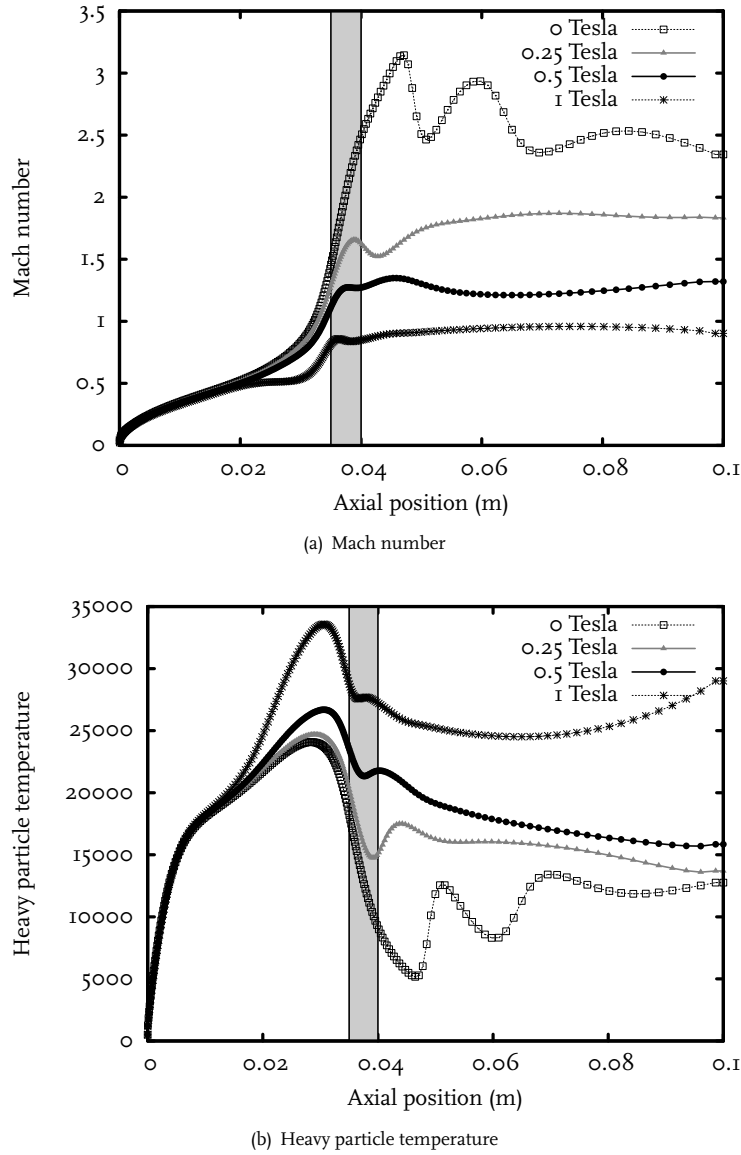


**Figure 8.2:** Mach number and heavy particle temperature on the symmetry axis for different magnetic field strengths. Since the radial Lorentz force prevents the plasma from expanding, the shockwave structure disappears. In addition, the drop in the temperature after the arc exit becomes less pronounced. In both plots the gray rectangle indicates the nozzle position.

where the Mach number is plotted, we can see that this is indeed the case. The plasma jet becomes narrower and more confined. To look in more detail at the effect of the magnetic field on the flow, the Mach number and heavy particle temperature are also plotted on the axis in Figure 8.2. We can distinguish several effects of the magnetic field. With increasing magnetic field the shock position moves upstream towards the

arc exit. In addition, the shockwave becomes weaker. Also, the Mach number decreases with increasing magnetic field strength. This is a result of the radial Lorentz force on the flow, which decreases the expansion of the flow. Furthermore, the radial Lorentz force will cause an increased pressure in the plasma beam. Since therefore the plasma expands effectively in a higher pressure environment, the shock position will move upstream. In addition, the temperature dip in the expansion becomes less pronounced. Due to the azimuthal Lorentz force the plasma jet will start to rotate. This can be seen in Figure 8.3, which gives a radial plot of the azimuthal velocity at  $z=6$  cm. Depending on the magnetic field, the azimuthal velocity has both positive and negative values.

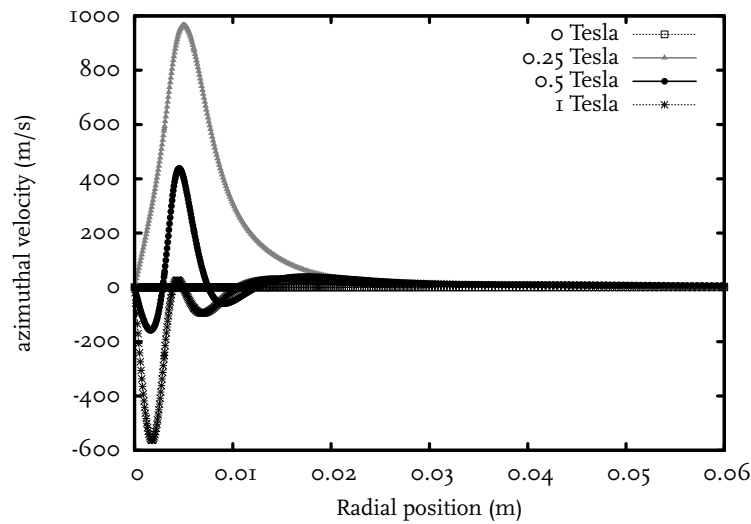


Figure 8.3: Azimuthal velocity for different magnetic field strengths at  $z=6$  cm.

### 8.3.2 Potential distribution

In Figure 8.4 isocontours for the potential for different magnetic field strengths can be seen. It can be seen that due to the anisotropy in the electrical conductivity, electrical current extends further into the vessel. This will drastically change the plasma since energy is now also put into the plasma in the vessel. Figure 8.5 shows a second characteristic of the potential in magnetized plasmas. In this figure, the potential is plotted as a function of the radial position at  $z=6$  cm. At the edge of the plasma beam there is a small wing where the potential is positive. This is due to the Hall current which is a source term for the potential equation.

### 8.3.3 Source output

In Figure 8.6, the ion and heat fluxes as function of the magnetic field can be seen. It is visible that until halfway the source, the magnetic field has no influence on the



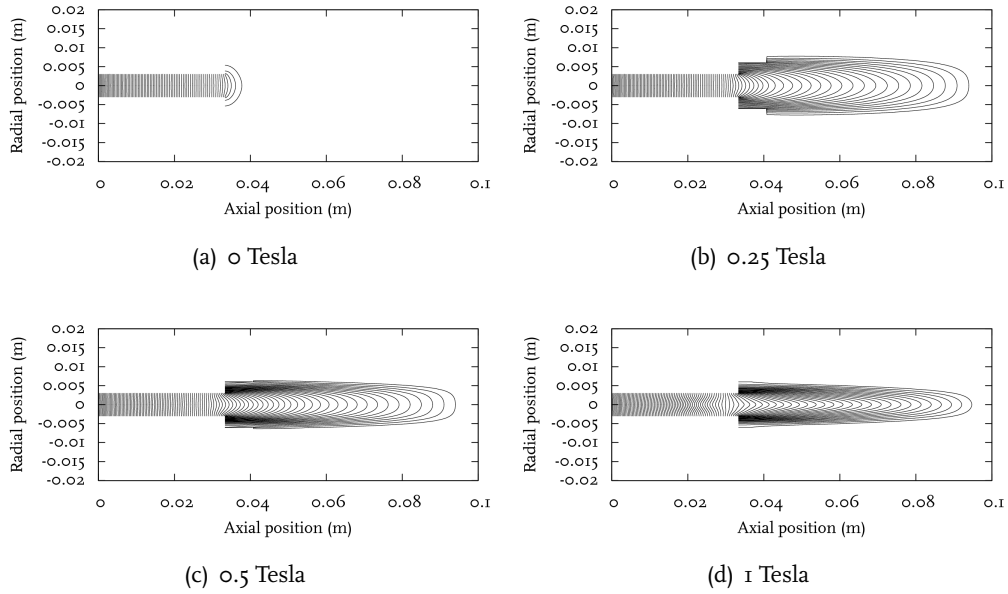


**Figure 8.4:** Isocontours for the potential. Due to the anisotropy in the electrical conductivity, electrical current extends further into the vessel.

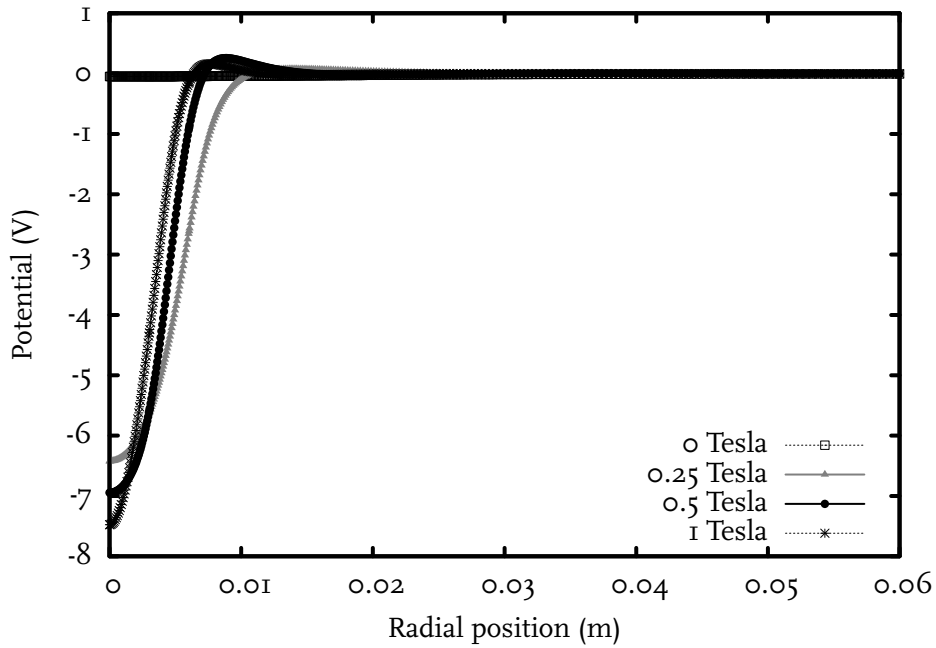
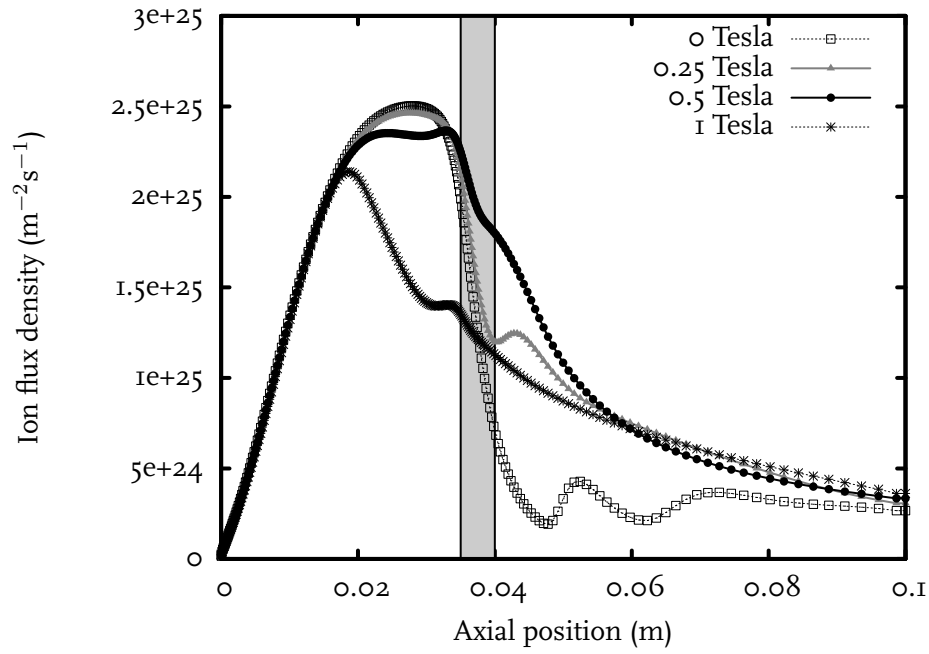
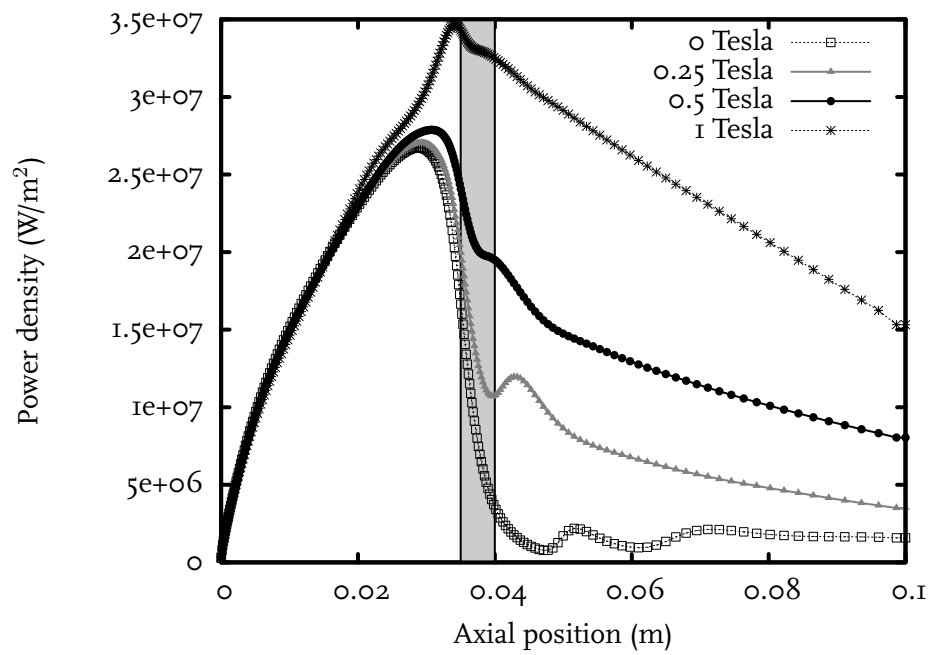


**Figure 8.5:** Potential as a function of radius at  $z = 6$  cm. Due to the Hall current, the potential is not a monotonic function.



(a) Ion flux



(b) Heat flux

**Figure 8.6:** Ion and heat flux densities on the symmetry axis. The gray rectangle indicates the nozzle position.

ion flux. After that, differences start to appear due to differences in the pressure and the flow field. However, overall, the magnetic field does not have a large influence on the ion flux. In contrast to the ion flux, the heat flux is strongly influenced by the magnetic field. This is mainly due to the higher temperatures reached in the magnetized case. Moreover, the conditions reached in this argon simulation are of the same order of magnitude as expected in the ITER divertor ( $10^{24}$  ions  $\text{m}^{-2}\text{s}^{-1}$ , 10 MW/ $\text{m}^2$ ).

## 8.4 Conclusions

In this chapter the effect of the magnetic field on an expanding argon plasma was studied. Inside the arc, where the plasma is created, no significant changes were observed compared to the unmagnetized plasma. However, in the expansion the plasma jet is strongly influenced by the magnetic field. Due to the Lorentz force on the flow field, the plasma jet becomes more confined and starts to rotate. Also the electromagnetic incoupling of power changed drastically. With a magnetic field, power input is not only present inside the arc, but also in the vacuum chamber. Furthermore, with a magnetic field, ion and heat fluxes were in the same order of magnitude as the fluxes expected in the ITER divertor.

We can conclude that our model is capable of capturing the characteristic features of the magnetized plasma jet. With respect to chemistry our model is still relatively simple: an argon plasma with one ion species. In the next chapter we will switch to hydrogen, resulting in a more complex chemistry with an increased number of species and reactions. In addition, the results from the hydrogen model will be compared to Pilot-PSI experiments.

## Chapter 9

# The expanding hydrogen plasma - comparison with experiments

### 9.1 Introduction

The previous two chapters focused on the simulation of argon plasmas to keep the chemistry as simple as possible. With the argon model the capability to simulate magnetized expanding plasmas was shown. However, since the main interest for Magnum-PSI is in hydrogen, we will now switch to hydrogen. Due to its molecular nature, simulation of hydrogen involves a much more complex chemistry compared to argon.

In contrast to argon, where the effective radius for the active plasma zone is equal to the channel radius, the hydrogen arc is thermally constricted. The thermal constriction is visible as a central peak at the symmetry axis of the discharge and a plateau near the cascaded arc wall. We will refer to this profile as the ‘sombrero’ profile. The particular shape of this profile is caused by a peak in the thermal conductivity for the dissociation transition ( $H_2 \leftrightarrow 2H$ ). This transition gives the plateau at about 3000 K near the wall.

Experimentally, the thermal constriction of the hydrogen cascaded arc can be deduced from the negative slope of the  $I - V$  characteristic, as measured in [52]. The current is concentrated at the center of the channel where the temperature is high (the central peak of the sombrero profile). As the current increases, this current channel becomes wider causing the conductance to increase. As a result, the slope of the  $I - V$  characteristic is flat or even negative.

Numerically, the constricted profile can easily be obtained in LTE simulations; see e.g. [68]. In non-LTE simulations, however, it has never been clearly observed. In [67] for example, a constricted profile was completely absent, while a minimal constriction was seen for the electron temperature in [68]. For the heavy particles, constriction was absent. Furthermore, no clear plateau at 3000 K was seen.

This chapter presents a hydrogen model capable of simulating the thermal contraction. Simulation results are compared to experiments on Pilot-PSI as described in [52]. In Section 9.2, the setup and operating conditions for both the experiment

and the numerical model are briefly discussed. After that, Section 9.3 focuses on the chemical composition, since the species and reaction set are crucial to obtain thermal constriction. The comparison of the simulation results to the experiments is presented in Section 9.4. This chapter ends with conclusions in Section 9.5.

## 9.2 Setup and operating conditions

A schematic figure of the cascaded arc plasma source can be seen in Figure 9.1. The arc consists of five cascade plates that are electrically insulated from each other. A hole in the center acts as the discharge channel. Both in the model and the experiments 4 and 5 mm wide channels are used. The last plate, which is grounded, acts both as

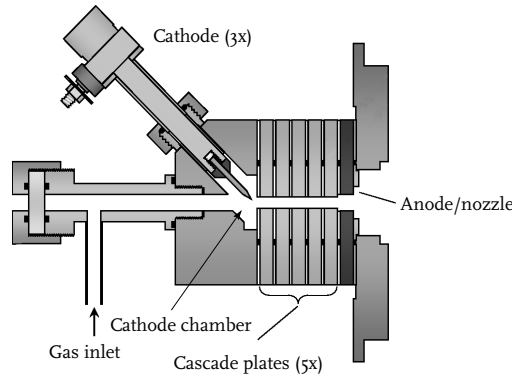


**Figure 9.1:** The cascaded arc plasma source. Gas flows from the gas inlet through the cathode chamber into the channel, where it is ionized. In the channel the plasma is accelerated and, passing the nozzle, the plasma expands into the vacuum chamber. Figure adapted from [52].

the anode and the nozzle. The inner diameter of the anode plate is 6 mm for the 4 mm wide discharge channel and 7.5 mm for the 5 mm wide discharge channel. The total length of the discharge channel excluding the anode plate is 33 mm. To model the discharge channel, the anode plate and the expansion, a non-rectangular grid of 44 by 80 cells was used.

In the cathode chamber, three cathodes emit the electron current thermionically. Hydrogen gas is fed to the discharge channel through the same chamber. The pressure in the cathode chamber is typically  $10^3$ - $10^4$  Pa depending on the gas flow, discharge current and channel diameter. An important difference between the model and the experiment is that in the experiment the hydrogen gas flow rate is used as one of the control parameters, while in the model the pressure is set as a boundary condition for numerical stability. The pressure in the vacuum vessel during experiments is 1-15 Pa, depending on the inlet gas flow rate. In the model, the vessel pressure is set to 50 Pa, since lower pressures lead to negative pressures at the transition from the arc to the chamber.

Numerical simulations are compared to pressure measurements, I-V measurements and Thomson scattering. Pressure measurements in [52] were performed as

function of the inlet gas flow rate between 0.2 and 10 slm for different channel diameters. The discharge current was 100 A and the magnetic field 0.4 Tesla. Opposed to the experiments, the model was run for different inlet pressures, giving the gas flow rate as a result.

To eliminate extra power input in the nozzle region, voltage measurements were carried out for a magnetic field of 0 Tesla. In [52], the I-V characteristic was measured for a fixed gas flow rate. Since in our model the pressure is used as a boundary condition and the voltage is more strongly influenced by the flow rate than by the current, reproducing the exact plots from [52] will be very cumbersome. Instead, we will look at the effect of the current on the flow rate for a fixed pressure and compare these results to [52].

To obtain the electron density and temperature in the expansion, Thomson scattering (TS) was performed by Vijvers [52]. Measurements were done at about 4 cm from the source exit. A magnetic field of 0.2 Tesla was applied to allow for the TS measurements; without magnetic field the plasma does not extend into the vessel. Again, the measurements and simulations could not be directly compared since measurements were carried out for a fixed flow rate.

### 9.3 Composition

The hydrogen mixture simulated consists of the species  $H_2$ ,  $H_2^{\nu=4}$ ,  $H$ ,  $H^+$  and  $e$ . These species are so-called transportable species, for which mass balances are solved. However, to determine effective reaction rates between these transportable species, more species need to be taken into account to correctly describe the reaction paths. These species are called local chemistry or intermediate species. The reaction to and from these levels are very fast and therefore they can be assumed to have negligible densities [69]. However, they can not be neglected in the reaction path. As intermediate species we take into account  $H_2^+$  and  $H^*$ . Both the transportable and intermediate species and the reaction paths are depicted in Figure 9.2. Vibrationally excited molecules are important for charge exchange. To take this into account,  $H_2^{\nu=4}$  is used as a representative species for these excited molecules. Charge transfer is most likely to occur with the vibrational level  $\nu = 4$  since the energy difference between  $H^+$  and  $H_2^+$  ions is almost equal to the energy of the level  $\nu = 4$ .

An overview of all the reactions used is given in Table 9.1. The reaction set and rate coefficients are largely based on the data presented in Ahmad [67]. In our model a smaller number of species and reactions is used. It was found that with the rate coefficient in [67] for heavy particle assisted dissociation:



no thermal constriction could be obtained. This is due to the fact that the effect of rovibrationally excited hydrogen molecules on the dissociation rate is ignored. This effect can easily increase the dissociation rate by a factor  $10^4$  as is shown by Capitelli in [70]. Therefore we chose to increase the rate coefficient as used in [67] with a factor

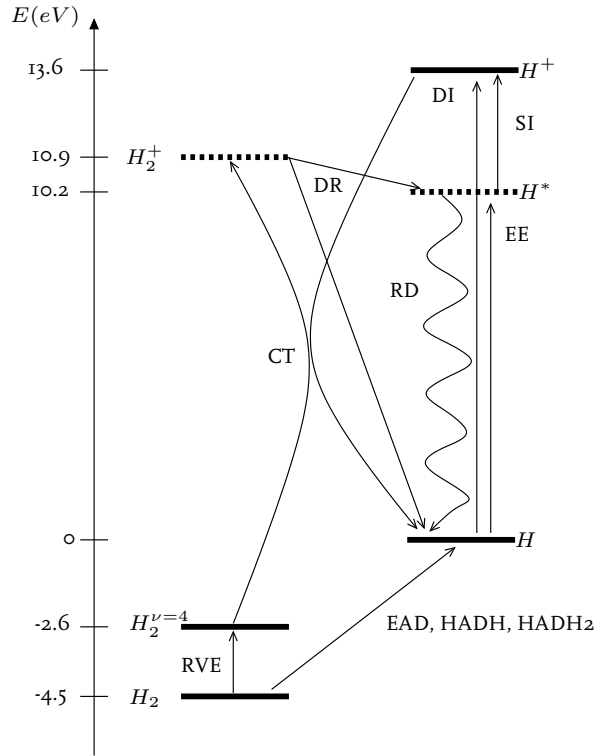
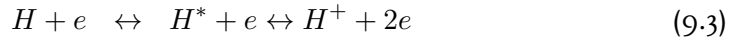


**Figure 9.2:** Processes and levels taken into account in the composition calculation. Levels indicated by a solid line are taken into account explicitly as transportable species. The densities of the dashed levels are assumed to be negligible. However, they are important as intermediate species for determining effective rate coefficients between the solid levels.

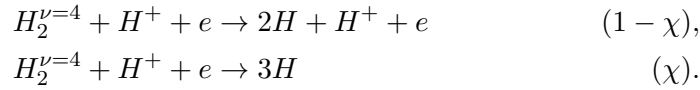
Name	Reaction	
EAD	Electron Assisted Dissociation	$H_2 + e \leftrightarrow 2H + e$
HADH	Heavy Particle Assisted Dissociation	$H_2 + H \leftrightarrow 3H$
HADH <sub>2</sub>	Heavy Particle Assisted Dissociation	$H_2 + H_2 \leftrightarrow 2H + H_2$
DI	Direct Ionization	$H + e \leftrightarrow H^+ + 2e$
EE	Electron Excitation	$H + e \leftrightarrow H^* + e$
SI	Stepwise Ionization	$H^* + e \leftrightarrow H^+ + 2e$
RVE	RoVibrational Excitation	$H_2 + e \leftrightarrow H_2^{\nu=4} + e$
CT	Charge Transfer	$H_2^{\nu=4} + H^+ \rightarrow H_2^+ + H$
DR	Dissociative Recombination	$H_2^+ + e \rightarrow H + H^*$
RD	Radiative Decay	$H^* \rightarrow H + h\nu$

**Table 9.1:** Reactions used for the hydrogen model. Note that the reaction chain CT-DR-SI/RD is combined in one effective reaction where the rate is only determined by the first step, charge transfer. The same is done for the stepwise ionization reaction EE-SI.

$10^4$ . In this way thermal constriction could be obtained. Note, however, that this is a rather crude approximation, not taking into account the spatial and temperature dependence of the dissociation process by rovibrationally excited molecules. Also for the direct and stepwise ionization reactions:



a rate coefficient different from [67] is used. The reason is that with the rate coefficient of [67] the electron mass fraction was not constricted, leading to a positive current voltage characteristic. Instead, the rate coefficients for direct and stepwise ionization as available in the Plasimo demosuite are used. The reaction chain charge transfer, dissociative recombination, followed by ionization ( $1 - \chi$  branch) or radiative decay ( $\chi$  branch) is described by an effective reaction:



Since we assume the reaction rate of this effective reaction is determined by the slowest step, the rate is calculated as the rate for charge transfer. As a result, the ionization and radiative decay transitions have equal probabilities ( $\chi = 0.5$ ).

## 9.4 Results

In this section we will compare the numerical results to pressure, I-V and Thomson scattering measurements from [52].

### 9.4.1 Comparison to pressure measurements

As was discussed in Section 9.2, in the experiment the hydrogen flow rate is used as a control variable, whereas in the simulation the pressure is specified as a boundary condition. To see if a specified pressure gives the correct hydrogen flow rate in the model, we compare our simulations with pressure measurements on Pilot PSI [52]. In Figure 9.3 the pressure in the cathode chamber as function of the hydrogen flow rate for two different geometries can be seen. It can be seen that the experiments and simulations are in good agreement with each other. Both in the experiments and the simulations the pressure increases with increasing gas flow rate and decreases with increasing channel diameter. The simulations systematically give a slightly lower pressure at the same flow rate. The fact that the pressure is measured in the cathode chamber, see Figure 9.1, while the pressure boundary condition is set at the edge of the first cascade plate can justify a small pressure difference.

### 9.4.2 Comparison to I-V measurements

In Figure 9.4, the cathode potential as function of the hydrogen flow rate can be seen. From the experimental data it can be seen that the flow rate has a much stronger



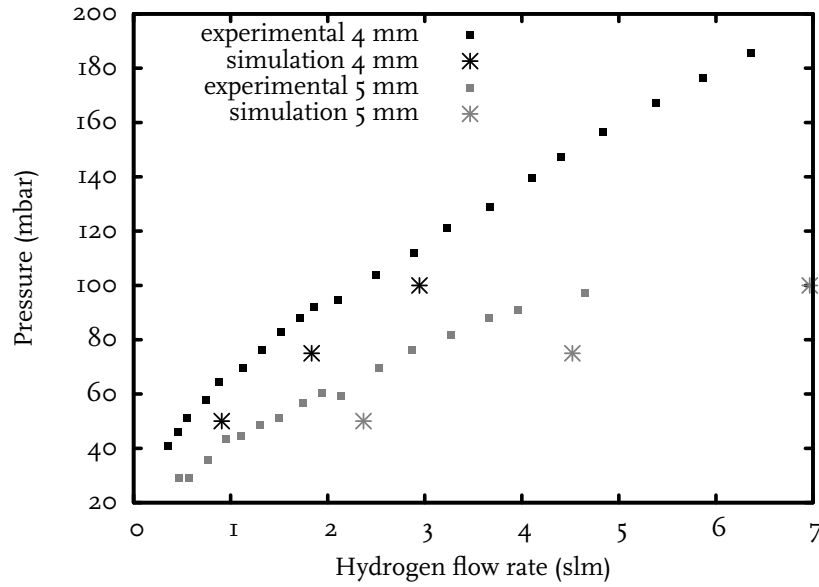


**Figure 9.3:** Pressure as function of the hydrogen flow rate for channel diameters of 4 and 5 mm. The discharge current was 100 A and the magnetic field 0.4 Tesla. Both in the experiments and the simulations the pressure increases with increasing gas flow rate and decreases with increasing channel diameter. The simulations systematically give a slightly lower pressure at the same flow rate. Experimental data from [52].

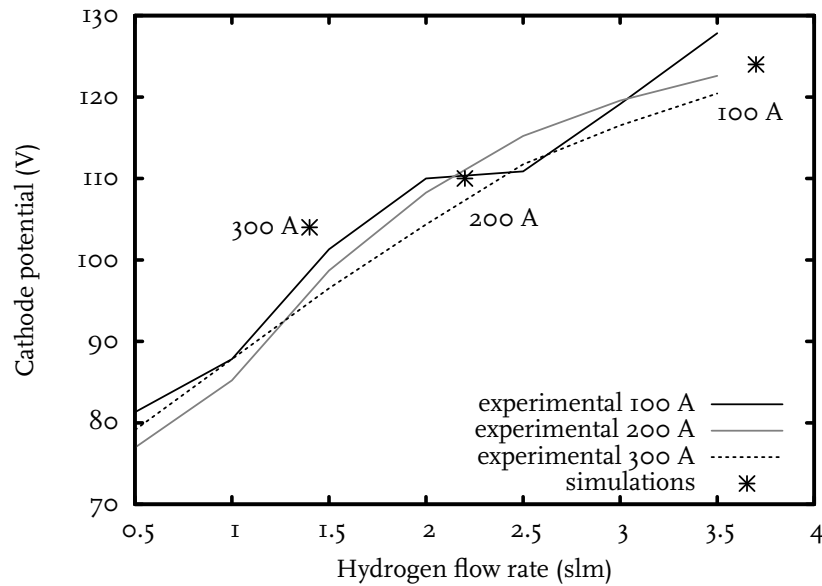


**Figure 9.4:** Cathode potential as function of hydrogen flow rate for a discharge with a channel diameter of 5 mm and a magnetic field of 0 Tesla. Experimental data from [52].

influence on the voltage than the current. The simulation data show a similar trend. As explained in the introduction, the current voltage characteristic is flat or negative because of widening of the constricted temperature profile with increasing current. This effect can be seen in Figures 9.5 and 9.6. To ensure that the model is capable of resolving the sombrero, the simulations were repeated on a much finer grid of 170 by 314 cells, which does not significantly alter the sombrero profile.

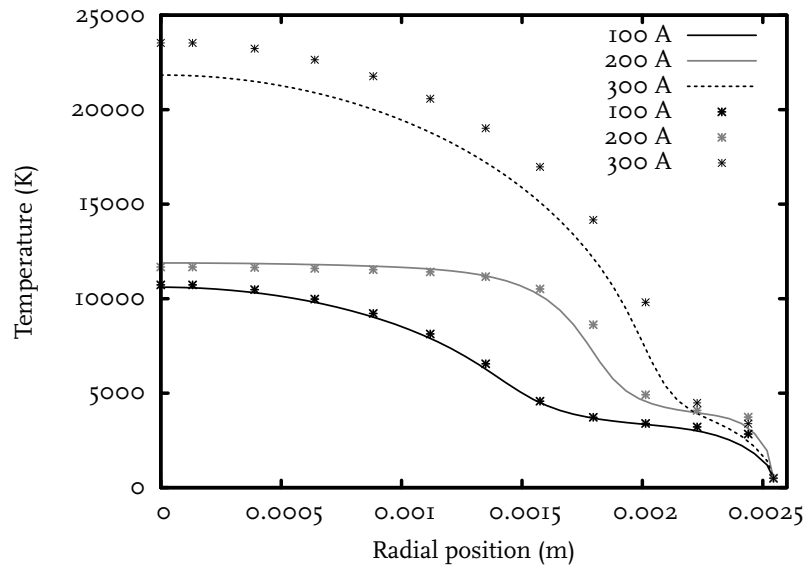


**Figure 9.5:** Heavy particle temperature at  $z=0.15$  cm. The channel diameter was 5 mm and the magnetic field 0 Tesla. Calculations on the coarse grid of 44 by 80 cells are indicated with points. Calculations on the grid with four times as many points in both radial and axial direction are indicated with lines.

Also the plateau at 3000 K due to the dissociation transition  $H_2 \rightarrow 2H$  can clearly be seen. To our knowledge, this is the first time the sombrero profile is generated with a complete non-LTE model. The crucial difference between this work and [67] and [68], where the sombrero is absent, is the rate for the heavy particle assisted dissociation reaction. In [67] and [68] the effect of rovibrationally excited molecules is not taken into account, resulting in rates that are approximately a factor  $10^4$  ([67]) and  $10^3$  ([68]) lower than the rate used here. An explanation for the fact that such high rates were not used before could be that the resulting strong chemical and energy source terms are difficult to treat numerically. In this thesis, special measures were taken in source term linearization (Section 3.3 of this thesis) to avoid problems with such large source terms.

#### 9.4.3 Comparison to Thomson measurements

In Figure 9.7 the Thomson Scattering and simulation results can be seen. Both the electron density and temperature in the simulations are significantly lower than the

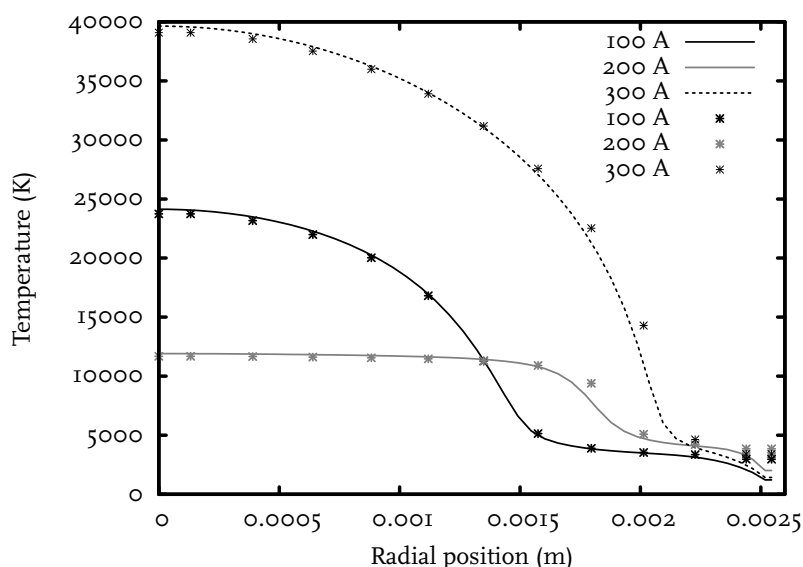


**Figure 9.6:** Electron temperature at  $z=0.15$  cm. The channel diameter was 5 mm and the magnetic field 0 Tesla. Calculations on the coarse grid of 44 by 80 cells are indicated with points. Calculations on the grid with four times as many points in both radial and axial direction are indicated with lines.

measured values. A possible explanation could be that in the simulation a background pressure of 50 Pa was used, while in the experiments, the background pressure was 1-15 Pa. As a result, the effect of the magnetic field on the plasma can be too small. Another difference between the model and the experiments is that in the experiment the gas flow rate is used as the control variable, while in the model the pressure is set as a boundary condition at the inlet. However, these explanations are not confirmed by additional simulations at different flow rates, background pressures and magnetic field strengths. A more probable cause of the discrepancies lies in the crude description of the molecular chemistry. As mentioned in section 9.3 the effect of rovibrationally excited molecules on the dissociation rate is taken into account by increasing the rate with a factor  $10^4$ . This results in the desired behavior in the source region, but is probably not valid in the expansion region. The temperature dependence and the spatial distribution of rovibrationally excited molecules is not taken into account.

## 9.5 Conclusions

In this chapter, simulations of the expanding hydrogen plasma were compared to measurements on Pilot-PSI by Vijvers et al. [52]. In the source region, where simulation results were compared to pressure and I-V measurements, good agreement was found. Both in the experiments and the simulations the pressure increased with

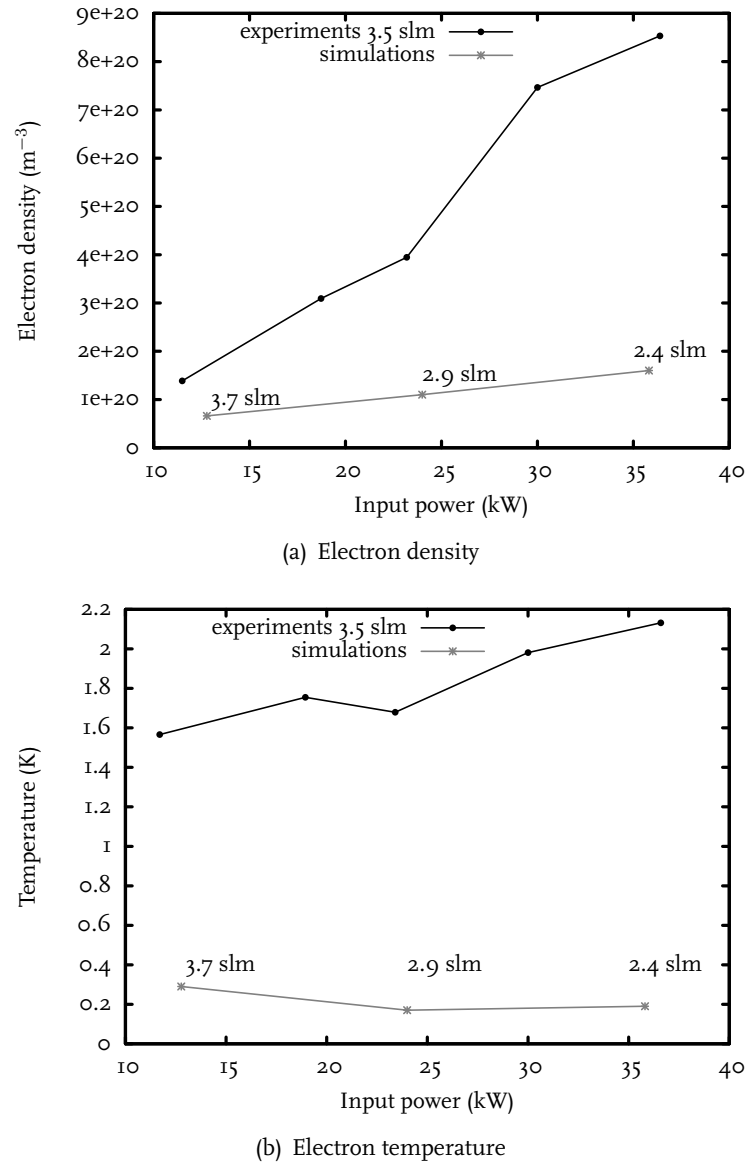


**Figure 9.7:** Electron density and temperature at 4 cm from the source exit for a discharge with  $d=5$  mm and  $B=0.2$  Tesla.

increasing gas flow rate and decreased with increasing channel diameter. The simulations systematically gave a slightly lower pressure at the same flow rate, which could be attributed to the discrepancy between the location of the pressure boundary conditions and the measurement location. Also for the I-V measurements, good agreement was found. The model was able to reproduce the sombrero profile for the first time in a non-LTE simulation. To obtain this result, the dissociation rate was increased by a

factor  $10^4$  to include the effect of rovibrationally excited molecules. To be able to use such high rates special measures were taken in source term linearization (Section 3.3 of this thesis) to avoid numerical problems. As a result of this approach, thermal constriction as present in the hydrogen arc and the resulting flat I-V characteristic were found in the simulations.

In the expansion region, where simulation results were compared to Thomson scattering measurements larger discrepancies between model and experiments were found. Both the electron density and temperature in the simulations were significantly lower than the measured values. Probably, increasing the dissociation rate with a factor  $10^4$ , is not valid in the expansion region, since the spatial distribution of rovibrationally excited molecules and the temperature dependence is not taken into account. It is well possible that the amount of rovibrationally excited molecules sharply decreases in the expansion. Collisions with hot electrons are less frequent in the expansion, while there is relaxation to lower levels by emission of IR radiation. With a more detailed description of the molecular chemistry, for example by describing the rovibrational states with a collisional radiative model, realistic simulations of Magnum-PSI should be possible with the presented model.

## Chapter 10

# General conclusions

A numerical model for simulation of magnetized expanding plasmas was constructed using the plasma modeling platform Plasimo. Balances of mass, momentum and energy were solved using the finite volume method. An important aspect of the numerical model is the multicomponent diffusion calculation. Numerical techniques were developed to successfully apply multicomponent diffusion to magnetized expanding plasmas. Simulations of both magnetized and non-magnetized expansions have been performed to verify the suitability of the numerical techniques.

The multicomponent diffusion model was developed in a systematic way. First, in Chapter 4, a coupled system of continuity equations was obtained from the Stefan-Maxwell equations for mixtures with only neutral species. To discretize this set of continuity equations, the exponential scheme was generalized to systems of convection-diffusion equations in Chapter 3. It was shown that with this new discretization scheme, mass conservation can be fulfilled up to machine accuracy without applying the mass constraint explicitly.

In Chapter 5, multicomponent diffusion was extended to mixtures with charged species. Instead of the usual assumption of zero current, we allowed a divergence free current driven by an external electric field to be present. To maintain charge neutrality, the calculation of the potential was self consistently coupled to the diffusion velocity. It was demonstrated that charge and mass conservation can be fulfilled up to machine accuracy without applying the constraints explicitly.

The multicomponent diffusion model was further extended with the magnetic field in Chapter 6. In magnetized plasmas, the flow directions across and around the magnetic field lines are coupled by the Lorentz force. Coupling is taken into account by using complex arithmetic in the diffusion algorithm. Furthermore, beside the potential, also the flow field is coupled to the diffusion velocities.

The feasibility of Plasimo's flow calculation and ambipolar diffusion was shown in Chapter 7 for an argon plasma. It was shown that Plasimo can handle the transition from a subsonic to a supersonic flow field. Expected physical behavior like the  $M=1$  condition at the arc exit and choking of the flow follow automatically from the model. The model can therefore be used when it is not known a priori whether the flow is subsonic or transonic. Another advantage of the integral approach is that the model

does not need to be split up on the interface of arc/chamber. This facilitated studying the effect of the nozzle geometry. It was shown that nozzle reflections lead to a more confined beam. For an increasing number of nozzle steps, the solution converged to a 'fixed' solution.

The effect of the magnetic field on the expanding argon plasma was studied in Chapter 8. Inside the arc, where the plasma is created, no significant changes were observed compared to the unmagnetized plasma from Chapter 7. However, in the expansion the plasma jet is strongly influenced by the magnetic field. Due to the Lorentz force on the flow field, the plasma jet becomes more confined and starts to rotate. Also the electromagnetic incoupling of power changed drastically. With a magnetic field, power input is not only present inside the arc, but also in the vacuum chamber. As a result, plasma production cannot be studied considering only the source region, since plasma production extends into the expansion region as well. With a magnetic field, ion and heat fluxes were of the same order of magnitude as the fluxes expected near the ITER divertor.

To keep the chemistry as simple as possible, the feasibility of modeling the magnetized expansion was shown in Chapters 7 and 8 for an argon plasma. Finally, a hydrogen model was presented in Chapter 9. Simulation results of the expanding hydrogen plasma were compared to experiments on Pilot-PSI. In the source region, where simulation results were compared to pressure and I-V measurements, good agreement was found. The model was able to reproduce the sombrero profile for the first time in a non-LTE simulation. To obtain this result, the dissociation rate was increased by a factor  $10^4$  to include the effect of rovibrationally excited molecules. Using such high rates was made possible by the new source term linearization as presented in Chapter 3, which ensures physical solutions even in the source dominated limit. In the expansion region, where simulation results were compared to Thomson scattering measurements larger discrepancies between model and experiments were found. This is understandable, since the adhoc factor  $10^4$  does not account for the temperature dependence and spatial distribution of rovibrationally excited molecules. The discrepancies can probably be overcome by using a more complete description of the molecular chemistry, including rovibrational excitation processes.

To conclude, a numerical model for studying the plasma creation in the source and the consecutive magnetized expansion in Magnum-PSI has been developed. This model captures the essential physical mechanisms of the magnetized expanding plasma.

## Appendix A

# Linear algebra overview

### A.1 The generalized inverse

Consider a square matrix  $\mathbf{A}$ . If there is a matrix  $\mathbf{B}$  such that  $\mathbf{BA} = \mathbf{I}$ , this is called the *inverse* of  $\mathbf{A}$ , it is denoted as  $\mathbf{A}^{-1}$ . If an inverse exists, the matrix is called *regular*, otherwise it is called *singular*. Every matrix  $\mathbf{A}$  has a unique *Moore-Penrose*, or *pseudo-inverse* [41, section 1.1]. This is the matrix  $\mathbf{A}^+$  that satisfies all four *Penrose equations*,

$$\begin{aligned} 1 : & \mathbf{AA}^+\mathbf{A} = \mathbf{A}; \\ 2 : & \mathbf{A}^+\mathbf{AA}^+ = \mathbf{A}^+; \\ 3 : & (\mathbf{AA}^+)^* = \mathbf{AA}^+; \\ 4 : & (\mathbf{A}^+\mathbf{A})^* = \mathbf{A}^+\mathbf{A}. \end{aligned} \tag{A.1}$$

It is readily verified that for a regular matrix  $\mathbf{A}^+ = \mathbf{A}^{-1}$  all these relations are satisfied: for a regular matrix the Moore-Penrose inverse is just the normal matrix inverse.

Following Ben-Israel and Greville [41], we will also consider *generalized inverses* that satisfy some, but not all of the four Moore-Penrose conditions. An inverse of  $\mathbf{A}$  that satisfies the conditions  $(i, j, k, \dots)$  is denoted as  $\mathbf{A}^{(i,j,k,\dots)}$ , and the set of all such matrices as  $\mathbf{A}\{i, j, k, \dots\}$ .

As an example  $\mathbf{A}^{(1)}$  denotes an inverse matrix that satisfies (at least) condition one. The set of all such matrices is denoted as  $\mathbf{A}\{1\}$ . An inverse that satisfies at least properties one and three is denoted as  $\mathbf{A}^{(1,3)}$  and is a member of the set  $\mathbf{A}\{1, 3\}$ . For the Moore-Penrose inverse we have  $\mathbf{A}^+ = \mathbf{A}^{(1,2,3,4)}$  and since it is unique it is the only member of the set  $\mathbf{A}\{1, 2, 3, 4\}$ .

Consider the constrained system [46, section 5.1]:

$$\begin{aligned} \mathbf{Ga} &= \mathbf{b}; \\ \mathbf{a} &\in \mathbf{C}, \end{aligned} \tag{A.2}$$

where  $\mathbf{G} \in \mathbb{R}^{n \times n}$  and  $\mathbf{C}$  is a linear subspace of that space. For subspaces  $\mathbf{C}$  and  $\mathbf{S}$  of  $\mathbb{R}^n$  such that  $N(\mathbf{G}) \oplus \mathbf{C} = \mathbb{R}^n$  and  $R(\mathbf{G}) \oplus \mathbf{S} = \mathbb{R}^n$ , there exists a  $\{1, 2\}$  generalized inverse  $\mathbf{Z}$  of  $\mathbf{G}$  with nullspace  $\mathbf{S}$  and range  $\mathbf{C}$ . In addition to  $\mathbf{ZGZ} = \mathbf{Z}$



and  $GZG = G$ , this has the properties

$$GZ = P_{R(G),S}, \quad (\text{A.3})$$

$$ZG = P_{C,N(G)}, \quad (\text{A.4})$$

where  $P_{R(G),S}$  is the projector onto parallel to  $S$ . Likewise,  $P_{C,N(G)}$  is the projector onto  $C$  along  $N(G)$ . In Appendix A.2, projectors will be discussed. The constrained system above is well-posed only if

$$N(G) \oplus C = \mathbb{R}^n. \quad (\text{A.5})$$

Then for any  $S$  such that  $R(G) \oplus S = \mathbb{R}^n$ , we can write  $a = Zb$ , where  $Z$  is the unique  $\{1, 2\}$  inverse of  $A$  with range  $C$  and nullspace  $S$ .

## A.2 Oblique projectors

Consider the oblique projection on  $a$  along  $b^\perp$ . The matrix  $P$  describing this projection is given by:

$$P = \frac{a \otimes b}{\langle b, a \rangle}. \quad (\text{A.6})$$

For an arbitrary  $x$ , the projection on  $a$  along  $b^\perp$  can therefore be written as:

$$Px = a \frac{\langle b, x \rangle}{\langle b, a \rangle}. \quad (\text{A.7})$$

This projection is schematically depicted in Figure A.1.

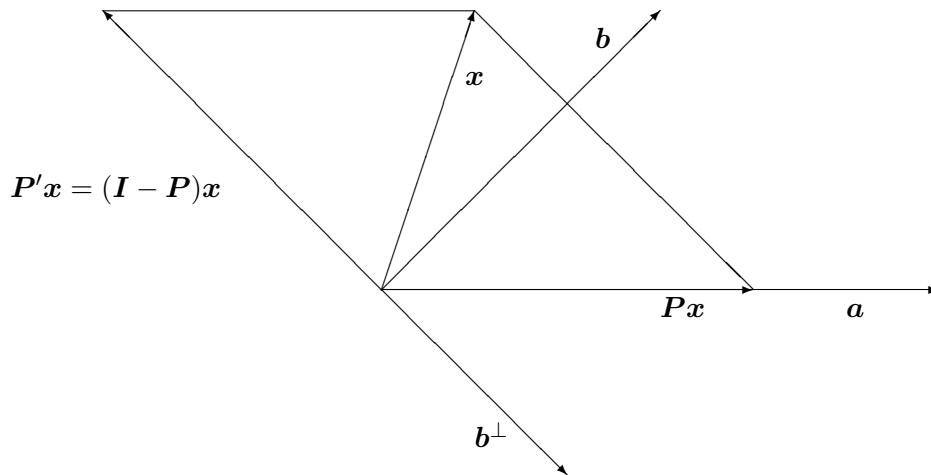


**Figure A.1:** The matrix  $P = a \otimes b / \langle b, a \rangle$  defines a projection on the vector  $a$  along the vector  $b^\perp$ .

From Figure A.1 it can also be seen that the range of  $\mathbf{P}$  is  $\mathbf{a}$  and its nullspace is  $\mathbf{b}^\perp$ . Note that when  $\mathbf{b} = \mathbf{a}$ , the projection is orthogonal, since in this case the range and the nullspace of  $\mathbf{P}$  are orthogonal subspaces. The projection then leaves  $\mathbf{a}$  invariant, and it annihilates all vectors orthogonal to  $\mathbf{a}$ . Projector matrices are *idempotent*; they can be applied multiple times without changing the result after the first application:

$$\mathbf{P}^2 \mathbf{x} = \frac{\mathbf{a} \otimes \mathbf{b}}{\langle \mathbf{b}, \mathbf{a} \rangle} \frac{\mathbf{a} \otimes \mathbf{b}}{\langle \mathbf{b}, \mathbf{a} \rangle} \mathbf{x} = \frac{\mathbf{a} \otimes \mathbf{b}}{\langle \mathbf{b}, \mathbf{a} \rangle} \mathbf{x} = \mathbf{P} \mathbf{x}. \quad (\text{A.8})$$

Now consider the projector  $\mathbf{P}'$ ,

$$\mathbf{P}' = \mathbf{I} - \mathbf{P} = \mathbf{I} - \frac{\mathbf{a} \otimes \mathbf{b}}{\langle \mathbf{b}, \mathbf{a} \rangle}. \quad (\text{A.9})$$

The nullspace of  $\mathbf{P}'$  is  $\mathbf{a}$ , while its range is  $\mathbf{b}^\perp$ . The matrix  $\mathbf{P}'$  is called the complementary projector to  $\mathbf{P}$  and gives the projection on  $\mathbf{b}^\perp$  along  $\mathbf{a}$ . Since  $\mathbf{P}'$  and  $\mathbf{P}$  are complementary, we have:

$$\mathbf{P} \mathbf{P}' = \mathbf{P} - \mathbf{P}^2 = \mathbf{P} - \mathbf{P} = 0. \quad (\text{A.10})$$

The matrix  $\mathbf{P}'$  is idempotent as well:

$$\mathbf{P}'^2 = \mathbf{P}'(\mathbf{I} - \mathbf{P}) = \mathbf{P}'. \quad (\text{A.11})$$



# List of symbols

## Physical quantities

Symbol	Unit	Definition
$\alpha$	$\text{sm}^{-2}$	free parameter for mass regularization
$\alpha$	-	underrelaxation parameter
$\beta$	$\text{m}^2 \text{s}^{-1}$	free parameter for mass regularization
$\vec{B}$	T	magnetic field
$\vec{b}_i$	$\text{N kg}^{-1}$	body force on species $i$
$\vec{c}_i$	$\text{m s}^{-1}$	peculiar velocity of species $i$
$c_{pi}$	$\text{J kg}^{-1} \text{K}^{-1}$	specific heat capacity of species $i$
$\gamma$	$\text{m}^2 \text{s}^{-1} \text{C}^{-2}$	free parameter for charge regularization
$\mathcal{D}_{ij}$	$\text{m}^2 \text{s}^{-1}$	binary diffusion coefficient
$D_{ij}$	$\text{m}^2 \text{s}^{-1}$	multicomponent diffusion coefficient
$D_{ij}^{\parallel}$	$\text{m}^2 \text{s}^{-1}$	multicomponent diffusion coefficient along $\vec{B}$
$D_{ij}^{\perp}$	$\text{m}^2 \text{s}^{-1}$	multicomponent diffusion coefficient across $\vec{B}$
$D_{ij}^{\odot}$	$\text{m}^2 \text{s}^{-1}$	multicomponent diffusion coefficient around $\vec{B}$
$\vec{d}_i$	$\text{m}^{-1}$	diffusion driving force for species $i$
$d_i^{\parallel}$	$\text{m}^{-1}$	component of diffusion driving force along $\vec{B}$
$d_i^{\perp}$	$\text{m}^{-1}$	component of diffusion driving force across $\vec{B}$
$d_i^{\odot}$	$\text{m}^{-1}$	component of diffusion driving force around $\vec{B}$
$\vec{E}$	$\text{V m}^{-1}$	total electric field
$\vec{E}_{amb}$	$\text{V m}^{-1}$	ambipolar electric field
$\vec{E}_{ext}$	$\text{V m}^{-1}$	external electric field
$\epsilon$	$\text{F m}^{-1}$	electrical permittivity
$F_{ij}$	$\text{sm}^{-2}$	friction matrix
$\phi$	V	electrostatic potential
$f_i$	$\text{s}^3 \text{m}^{-6}$	distribution function of species $i$
$\vec{F}_i$	$\text{N m}^{-3}$	volumetric force on species $i$
$\Gamma_{ij}$	$\text{kg m}^{-1} \text{s}^{-1}$	multicomponent flux diffusion matrix
$h_i$	$\text{J kg}^{-1}$	specific enthalpy of species $i$
$h_i^0$	$\text{J kg}^{-1}$	specific enthalpy of formation of species $i$
$\vec{J}_i$	$\text{kg m}^{-2} \text{s}^{-1}$	diffusive mass flux of species $i$

$\vec{j}$	$\text{A m}^{-2}$	electrical current density
$\ell_i$	$\text{m}$	Larmor radius of species $i$
$\lambda_e$	$\text{J K}^{-1} \text{m}^{-1} \text{s}^{-1}$	electron heat conductivity
$\lambda_h$	$\text{J K}^{-1} \text{m}^{-1} \text{s}^{-1}$	heavy particle heat conductivity
$\mathbf{M}$	-	matrix relating the gradients of the mole fractions to the gradients of the mass fractions
$m_i$	$\text{kg}$	mass of a single particle of species $i$
$\mu$	$\text{Pa s}$	dynamic viscosity
$n_i$	$\text{m}^{-3}$	number density of species $i$
$p$	$\text{Pa}$	pressure
$p_i$	$\text{Pa}$	partial pressure of species $i$
$P$	-	Peclet number
$\mathbf{P}$	-	Peclet matrix
$q_i$	$\text{C}$	charge of a single particle of species $i$
$\vec{q}_e$	$\text{Jm}^{-2}\text{s}^{-1}$	electron heat flux
$\vec{q}_h$	$\text{Jm}^{-2}\text{s}^{-1}$	heavy particle heat flux
$Q_{ohm}$	$\text{Jm}^{-3}\text{s}^{-1}$	ohmic dissipation
$Q_{eh}$	$\text{Jm}^{-3}\text{s}^{-1}$	heat transfer between electrons and heavy particles
$r_i$	$\text{C kg}^{-1}$	charge to mass ratio of species $i$
$\mathbf{R}$	$\text{kgm}^{-3}$	matrix relating the mass fluxes to the velocities
$\rho$	$\text{kg m}^{-3}$	mass density
$\rho_i$	$\text{kg m}^{-3}$	mass density of species $i$
$\sigma^m$	-	mass constraint species
$\sigma^c$	$\text{C kg}^{-1}$	charge neutrality species
$\sigma$	$\text{S m}^{-1}$	electrical conductivity
$T_i$	$\text{K}$	temperature of species $i$
$\vec{u}_i$	$\text{m s}^{-1}$	velocity of species $i$
$\vec{v}_i$	$\text{m s}^{-1}$	diffusion velocity of species $i$
$\vec{v}$	$\text{m s}^{-1}$	mass averaged flow velocity
$x_i$	-	mole fraction of species $i$
$y_i$	-	mass fraction of species $i$
$z_i$	$\text{C m}^{-3}$	charge density of species $i$
$\omega_i$	$\text{m}^{-3}\text{s}^{-1}$	production rate of species $i$
$\Omega_i$	$\text{s}^{-1}$	Larmor frequency of species $i$

### Mathematical symbols

$\otimes$	dyadic product
$\oplus$	direct sum
$\langle, \rangle$	inner product
$\parallel$	direction parallel to the magnetic field
$\perp$	direction perpendicular to the magnetic field
$\odot$	direction around the magnetic field

# Bibliography

- [1] <http://www.iter.org>.
- [2] G. Federici, C.H. Skinner, J.N. Brooks, J.P. Coad, C. Grisolia, A.A. Haasz, A. Hassanein, V. Philipps, C.S. Pitcher, J. Roth, W.R. Wampler, and D.G. Whyte. Plasma-material interactions in current tokamaks and their implications for next step fusion reactors. *Nuclear Fusion*, 41(12):1967, 2001.
- [3] H. Maecker. *Zeit. Naturforsch.*, 11a(457), 1956.
- [4] G. Kroesen, D. Schram, and J. de Haas. Description of a flowing cascade arc plasma. *Plasma Chem. and Plasma Proc.*, 10:531–551, 1990.
- [5] M. Cinalli and R. Keppens. Supersonic expansion in the Pilot-PSI plasma jet: neutral gas and MHD models. *J. Phys. D: Appl. Phys.*, 39:4589, 2006.
- [6] E. D. de Rooij, U. von Toussaint, A. W. Kleyn, and W.J. Goedheer. Molecular dynamics simulations of amorphous hydrogenated carbon under high hydrogen fluxes. *Physical Chemistry Chemical Physics*, 11(42):9823–9830, 2009.
- [7] E. D. de Rooij, A. W. Kleyn, and W.J. Goedheer. Sticking of hydrocarbon radicals on different amorphous hydrogenated carbon surfaces: a molecular dynamics study. *Physical Chemistry Chemical Physics*, 12(42):14067–14075, 2010.
- [8] E. Salonen, K. Nordlund, J. Keinonen, and C.H. Wu. Molecular dynamics studies of the sputtering of divertor materials. *Journal of Nuclear Materials*, 313–316:404–407, 2003.
- [9] M. Baeva, W.J. Goedheer, N.J. Lopes Cardozo, and D. Reiter. B2-EIRENE simulation of plasma and neutrals in MAGNUM-PSI. *Journal of Nuclear Materials*, 363-365(0):330–334, 2007.
- [10] R. Wieggers and W.J. Goedheer. Accepted for publication. *Contrib. to plasma physics*.
- [11] <http://plasimo.phys.tue.nl>.
- [12] D. Benoy. *Modelling of thermal argon plasmas*. PhD thesis, Eindhoven University of Technology, The Netherlands, 1993.

- [13] E. Holt and R. Haskell. *Foundations of plasma dynamics*. New York: The Macmillan Company, 1965.
- [14] M. Mitchner and C.H. Kruger. *Partially Ionized Gases*. New York: Wiley & Sons, 1973.
- [15] T. Magin and G. Degrez. Transport algorithms for partially ionized and unmagnetized plasmas. *Journal of Computational Physics*, 198:424–449, 2004.
- [16] A. Ern and V. Giovangigli. *Multicomponent transport algorithms*. Springer-Verlag, Heidelberg, 1994.
- [17] L. Frost. Conductivity of seeded atmospheric pressure plasmas. *J. Appl. Phys.*, 32:2029, 1961.
- [18] P. Helander and D. Sigmar. *Collisional transport in magnetized plasmas*. Cambridge University Press, Cambridge, 2002.
- [19] J. Ferziger and H. Kaper. *Mathematical Theory of Transport Processes in Gases*. North Holland, Amsterdam, 1972.
- [20] S.B. Pope. The calculation of turbulent recirculating flows in general orthogonal coordinates. *J. Comput. Phys*, 26:197–217, 1978.
- [21] C. D. Mobley and R. J. Stewart. On the numerical generation of boundary-fitted orthogonal curvilinear coordinate systems. *J. Comput. Phys*, 34:124–135, 1980.
- [22] S. Patankar. *Numerical heat transfer and fluid flow*. Taylor and Francis, Levittown, 1980.
- [23] H. Versteeg and W. Malalasekera. *An Introduction to Computational Fluid Dynamics*. Longman Scientific and Technical, Harlow, 1995.
- [24] D.L. Scharfetter and H.K. Gummel. Large-signal analysis of a silicon read diode oscillator. *IEEE Transactions on Electron Devices*, 16(1):64–77, 1969.
- [25] J. Ten Thijs Boonkamp, J. van Dijk, L. Liu, and K. Peerenboom. Extension of the complete flux scheme to systems of conservation laws. *Accepted for publication in Journal of Scientific Computing*. <http://dx.doi.org/10.1007/s10915-012-9588-5>.
- [26] J. H. M. Ten Thijs Boonkamp and M. J. Anthonissen. The finite volume-complete flux scheme for advection-diffusion-reaction equations. *J. Sci. Comput.*, 46(1):47–70, January 2011.
- [27] H. T. Cullinan. Analysis of flux equations of multicomponent diffusion. *Industrial & Engineering Chemistry Fundamentals*, 4(2):133–139, 1965.
- [28] P. Rini, D. Vanden Abeele, and G. Degrez. Closed form for the equations of chemically reacting flows under local thermodynamic equilibrium. *Phys. Rev. E*, 72:011204–1–011204–12, 2005.

- [29] A. Hartgers, H. van der Heijden, M. Beks, J. van Dijk, and J. van der Mullen. An elemental diffusion description for LTE plasma models. *J. Phys. D: Appl. Phys.*, 38:3422–3429, 2005.
- [30] M. Beks, A. Hartgers, and J. van der Mullen. Demixing in a metal halide lamp, results from modelling. *J. Phys. D: Appl. Phys.*, 39:4407–4416, 2006.
- [31] Adolf Fick. über diffusion. *Poggendorff's Annal. Physik.*, 94:59–86, 1855.
- [32] Adolf Fick. On liquid diffusion. *Phil. Mag. and Jour. Sci.*, 10:31–39, 1855.
- [33] S. Chapman and T. Cowling. *The Mathematical Theory of Non-uniform Gases*. Cambridge University Press, Cambridge, 1960.
- [34] W. Wangard, D. Dandy, and B. Miller. A numerically stable method for integration of the multicomponent species diffusion equations. *Journal of Computational Physics*, 174:460–472, 2001.
- [35] E. Burman, A. Ern, and V. Giovangigli. Bunsen flame simulation by finite elements on adaptively refined, unstructured triangulations. *Combustion Theory and Modelling*, 8:65–84, 2004.
- [36] D. Pope and G. Gogos. A new multicomponent diffusion formulation for the finite-volume method: application to convective droplet combustion. *Numerical Heat Transfer, Part B*, 48:213–233, 2005.
- [37] S. Mazumder. Critical assessment of the stability and convergence of the equations of multi-component diffusion. *Journal of Computational Physics*, 212:383–392, 2006.
- [38] V. Giovangigli. Mass conservation and singular multicomponent diffusion algorithms. *IMPACT Comput. Sci. Eng.*, 2:73–97, 1990.
- [39] F.A. Williams. Elementary derivation of the multicomponent diffusion equation. *Am. J. Phys.*, 26:467–469, 1958.
- [40] D. Burnett. The distribution of molecular velocities and the mean motion in a non-uniform gas. *Proceedings of the London Mathematical Society*, s2-40(1):382–435, 1936.
- [41] Adi Ben-Israel and Thomas N.E. Greville. *Generalized Inverses — Theory and Applications*. John Wiley and Sons, New York, 1973.
- [42] K. Morton. *Numerical Solution of Convection-Diffusion Problems*. Chapman and Hall, London, 1996.
- [43] M. Protter and H. Weinberger. *Maximum Principles in Differential Equations*. Prentice-Hall, Englewood Cliffs, 1967.



- [44] V. Giovangigli. Convergent iterative methods for multicomponent diffusion. *IMPACT Comput. Sci. Eng.*, 3:244–267, 1991.
- [45] V. Giovangigli and B. Graille. Asymptotic stability of equilibrium states for ambipolar plasmas. *Mathematical Models and Methods in Applied Sciences*, 14(9):1361–1399, 2004.
- [46] V. Giovangigli. Multicomponent transport algorithms for partially ionized mixtures. *Journal of Computational Physics*, 229:4117–4142, 2010.
- [47] K.S.C. Peerenboom, J. van Dijk, J.H.M. ten Thije Boonkkamp, L. Liu, W.J. Goedheer, and J.J.A.M. van der Mullen. Mass conservative finite volume discretization of the continuity equations in multi-component mixtures. *Journal of Computational Physics*, 230(9):3525–3537, 2011.
- [48] L.W. Ehrlich. Complex matrix inversion versus real. *Communications of the ACM*, 13:561–562, 1970.
- [49] V. Giovangigli and B. Graille. Kinetic theory of partially ionized reactive gas mixtures. *Physica A*, 327:313–348, 2003.
- [50] V. Giovangigli, B. Graille, T. Magin, and M. Massot. Multicomponent transport in weakly ionized mixtures. *Plasma Sources Science and Technology*, 19:034002, 2010.
- [51] S. Selezneva, M. Boulos, M. van de Sanden, R. Engeln, and D. Schram. Stationary supersonic plasma expansion: continuum fluid mechanics versus direct simulation Monte Carlo method. *J. Phys. D: Appl. Phys.*, 35:1362, 2002.
- [52] W. Vijvers, C. van Gils, W. Goedheer, H. van der Meiden, D. Schram, V. Veremiyenko, J. Westerhout, N. Lopes Cardozo, and G. van Rooij. Optimization of the output and efficiency of a high power cascaded arc hydrogen plasma source. *Physics of plasmas*, 15:093507, 2008.
- [53] H. van Eck, W. Koppers, G. van Rooij, W. Goedheer, R. Engeln, D. Schram, N. Lopes Cardozo, and A. Kleyn. Modeling and experiments on differential pumping in linear plasma generators operating at high gas flow rates. *Journal of applied physics*, 105:063307, 2009.
- [54] J. Diebel, T. Magin, M. Panesi, P. Rini, D. Vanden Abeele, and Gérard Degrez. *Simulation of Supersonic Flows in Inductively Coupled Plasma Tunnels*. Springer Berlin Heidelberg, 2004.
- [55] P. Han and X. Chen. Modeling of the supersonic argon plasma jet at low gas pressure environment. *Thin Solid Films*, 390:181, 2001.
- [56] Y. Bartoziewicz, P. Proulx, and Y. Mercadier. A self-consistent two-temperature model for the computation of supersonic argon plasma jets. *J. Phys. D: Appl. Phys.*, 35:2139, 2002.

- [57] S. Selezneva, M. Rajabian, D. Gravelle, and M. Boulos. Study of the structure and deviation from equilibrium in direct current supersonic plasma jets. *J. Phys. D: Appl. Phys.*, 34:2862, 2001.
- [58] C. Chapman. *High speed flow*. Cambridge University Press, Cambridge, 2000.
- [59] R. Courant and K. Friedrichs. *Supersonic flow and shock waves*. Interscience Publishers, 1963.
- [60] H. Ashkenas and F. Sherman. *Rarefied gas dynamics*. Academic New York, 1966.
- [61] K.T.A.L. Burm. *Modelling of non-equilibrium plasma flows*. PhD thesis, Eindhoven University of Technology, The Netherlands, 2001.
- [62] S. Majumdar. Role of underrelaxation in momentum interpolation for calculation of flow with nonstaggered grids. *Numerical heat transfer*, 13:125, 1988.
- [63] C. Rhie and W. Chow. Numerical study of the turbulent flow past an airfoil with trailing edge separation. *AIAA journal*, 21:1525, 1983.
- [64] K. Karki and S. Patankar. Pressure based calculation procedure for viscous flows at all speeds in arbitrary configurations. *AIAA Journal*, 27:1167, 1989.
- [65] J. Hasted. *Physics of atomic collisions*. Butterworths London, 1972.
- [66] J. van der Mullen and J. Jonkers. Fundamental comparison between non-equilibrium aspects of ICP and MIP discharges. *Spectrochim. Act. B*, 54:1017, 1999.
- [67] Z. Ahmad and W.J. Goedheer. Numerical simulation of a cascaded arc source with different Ar–H<sub>2</sub> mixtures of nonlocal thermal equilibrium plasmas. *Physics of Plasmas*, 16(8):083503, 2009.
- [68] G. Janssen. *Design of a general plasma simulation model*. PhD thesis, Eindhoven University of Technology, The Netherlands, 2000.
- [69] J. van Dijk, A. Hartgers, J. Jonkers, and J.A.M. van der Mullen. Collisional radiative models with multiple transport-sensitive levels — application to high electron density mercury discharges. *J. Phys. D: Appl. Phys.*, 34:1499–1509, 2001.
- [70] M. Capitelli et al. Some aspects of electron-molecule scattering, molecular dynamics, and vibrational kinetics in nonequilibrium H<sub>2</sub>/D<sub>2</sub> plasmas. *Plasma Physics Reports*, 25(1), 1999.



# Abstract

## Modeling of Magnetized Expanding Plasmas

In fusion reactors, the walls are exposed to very high particle and energy fluxes. To study the problem of wall erosion and hydrogen retention in these conditions, the Magnum-PSI experiment at the FOM Institute of Plasma Physics is set up. The plasma source for Magnum-PSI is a cascaded arc, where a strong magnetic field is applied to obtain the desired conditions.

The focus of this thesis is the development of a numerical model for studying the plasma creation in the source and the consecutive magnetized expansion. To describe the behavior of the different species in the range of conditions in the plasma – from gas to fully ionized, from non-magnetized to strongly magnetized – a multi-component diffusion description is needed. Numerical techniques are developed to successfully apply multicomponent diffusion to magnetized expanding plasmas.

Multi-component diffusion results in a system of coupled continuity equations for all species. In addition this coupled system is subject to mass and charge conservation constraints. To deal with the coupling between the species a new finite volume discretization method is introduced to discretize the system of continuity equations. For numerical stability, mass and charge constraints are not explicitly applied. Instead, all species mass fractions are treated as independent unknowns and mass and charge constraints are a result of the continuity equations, the boundary conditions, the diffusion algorithm and the new discretization scheme. With this method, mass and charge constraints can be satisfied exactly, although they are not explicitly applied.

To verify the suitability of the method, simulations of both magnetized and non-magnetized expansions have been performed. The simulations are able to reproduce important characteristics of magnetic confinement. Results show that in the magnetized case, the plasma production cannot be modeled by considering the source alone, since plasma production extends into the expansion region.



# Dankwoord

Tijdens mijn afstuderen ben ik bij EPG begonnen met het modelleren van het gemagnetizeerde plasma van Magnum PSI. Waar mijn afstudeeronderzoek toen bestond uit het constateren van hindernissen op weg naar een model, mocht ik nu tijdens mijn promotie deze uitdagingen echt aan gaan pakken. Dit was niet mogelijk geweest zonder de hulp van de volgende personen.

Allereerst natuurlijk Joost van der Mullen en Wim Goedheer die deze positie creëerden en het daardoor mogelijk maakten om het onderzoek naar het modelleren van Magnum PSI voort te zetten. Wim ook bedankt voor de begeleiding vanuit FOM Rijnhuizen. Je hield vertrouwen in een goede afloop ook toen alles wat minder liep. Jan van Dijk was mijn dagelijks begeleider op de TU/e en heeft me wegwijs gemaakt in de wereld van Plasimo, C++ en Linsys. Speciale dank naar Gerrit Kroesen, mijn eerste promotor, die in het laatste stadium van mijn promotie bereid was om de begeleiding op zich te nemen.

Ook wil ik graag Vincent Giovangigli bedanken die altijd bereid was om mijn vragen over multi-component diffusie te bespreken. Met Jan Ten Thijs Boonkamp heb ik prettig samengewerkt met het opzetten van het gekoppelde schema, dat onmisbaar bleek bij het toepassen van de diffusie theorie in simulaties. Daarnaast nam je de moeite om mijn proefschrift grondig te lezen en de wiskundige puntjes op de i te zetten. Ook de andere leden van mijn promotiecommissie, Herman Clercx and Gérard Degrez, wil ik bedanken voor het lezen van het proefschrift.

Het was fijn werken binnen de EPG groep en ik wil dan ook alle EPG'ers bedanken voor de prettige werksfeer. In het bijzonder wil ik noemen: het Plasimo team, Rina Boom, mijn stagiair Romain Le Picard en kamergenoten Diana, Manolo, Sara, Ana en Mykhaylo.

Tot slot, Mark, bedankt voor alle geduld de afgelopen 4 jaar, en de zowel praktische als emotionele steun bij het schrijven van dit proefschrift.



# Curriculum Vitae

**December 15<sup>th</sup> 1983**

Born in Eindhoven, the Netherlands.

**1996-2002**

Gymnasium, Lorentz Casimir Lyceum, Eindhoven, the Netherlands.

**2002-2008**

M. Sc. in Applied Physics at Eindhoven University of Technology (cum laude).

- Graduation project in the Elementary Processes in Gas Discharges group at Eindhoven University of Technology, subject: numerical modeling of magnetized plasmas.
- Traineeship at The Centre for Estuarine and Marine Ecology, The Netherlands Institute of Ecology (NIOO-KNAW), Yerseke, the Netherlands, subject: experimental study on the influence of vegetation on sediment dynamics.
- Traineeship in the Elementary Processes in Gas Discharges group at Eindhoven University of Technology, subject: numerical modeling of the electric field in HID lamps.

**2008-2012**

Ph.D. candidate in the Elementary Processes in Gas Discharges group at Eindhoven University of Technology.